NTNU
Norwegian University of
Science and Technology

Investigation and Comparison of Methods Accounting for Asynchronous Seismic Ground Motions for Bridges

Nils Henrik Haughovd
Herman Høy

Department of Structural Engineering
Faculty of Engineering Science and Technology
NTNU- Norwegian University of Science and Technology

ACCESSIBILITY

Open

MASTER THESIS 2017

SUBJECT AREA:	DATE:	NO. OF PAGES:
Earthquake engineering	June 11th 2017	106 + 25 (appendix)

TITLE:

Investigation and Comparison of Methods Accounting for Asynchronous Seismic Ground Motions for Bridges

Undersøkelse og sammenligning av metoder som tar hensyn til asynkron seismisk bevegelse for broer

BY:

Nils Henrik Haughovd

Herman Høy

SUMMARY:

Eurocode 8, part 2, presents various methods to incorporate asynchronous seismic excitation for bridges. Common practice is to use time history analyses due to their high level of accuracy; however, they are computationally expensive. The aim of this study was therefore to investigate whether other, faster, methods could produce comparable results, and to examine their strengths and weaknesses. Two finite element models were developed in ANSYS: 1) the Chacao Bridge, which is a large two-span suspension bridge, and 2) a four-span beam bridge for verification of implementation and results.

The single-point response spectrum method generally proved to be conservative, and results corresponded well with those from the simplified method in the Eurocode. However, the simplified method presented greatly amplified response for the Central Pylon in the Chacao Bridge, and the method's pseudo-static displacements failed to account for varying seismic characteristics.

The multi-point response spectrum method in ANSYS was by far the fastest and most user-friendly method. It provided the most coincident results with those from the time history analysis. However, the results from the two bridge models led to different observations. The response for the four-span beam bridge was overestimated, while the response for the Chacao Bridge was slightly underestimated. The method proved to be sensitive to the structure's configuration and stiffness. Consequently, small, stiff structures and structural components spanning multiple supports may be severely overestimated using this method. On the other hand, accurate results may be obtained for large and soft structures with independently moving components.

Displacements and rotations were successfully extracted from Der Kiureghian and Neuenhofer's response spectrum method. The Eurocode's simplified version provided identical results, and its simplifications were justified. However, forces and moments could not be calculated due to inaccuracies in the transfer function.

RESPONSIBLE TEACHER: Prof. Amir M. Kaynia

SUPERVISOR: Prof. Amir M. Kaynia (NTNU)

CARRIED OUT AT: Department of Structural Engineering, NTNU.

Abstract

Eurocode 8, part 2, presents various methods to incorporate asynchronous seismic excitation for bridges. Common practice is to use time history analyses due to their high level of accuracy; however, they are computationally expensive. The aim of this study was therefore to investigate whether other, faster, methods could produce comparable results, and to examine their strengths and weaknesses. Two finite element models were developed in ANSYS: 1) the Chacao Bridge, which is a large two-span suspension bridge, and 2) a four-span beam bridge for verification of implementation and results.

The single-point response spectrum method generally proved to be conservative, and results corresponded well with those from the simplified method in the Eurocode. However, the simplified method presented greatly amplified response for the Central Pylon in the Chacao Bridge, and the method's pseudo-static displacements failed to account for varying seismic characteristics.

The multi-point response spectrum method in ANSYS was by far the fastest and most user-friendly method. It provided the most coincident results with those from the time history analysis. However, the results from the two bridge models led to different observations. The response for the four-span beam bridge was overestimated, while the response for the Chacao Bridge was slightly underestimated. The method proved to be sensitive to the structure's configuration and stiffness. Consequently, small, stiff structures and structural components spanning multiple supports may be severely overestimated using this method. On the other hand, accurate results may be obtained for large and soft structures with independently moving components.

Displacements and rotations were successfully extracted from Der Kiureghian and Neuenhofer's response spectrum method. The Eurocode's simplified version provided identical results, and its simplifications were justified. However, forces and moments could not be calculated due to inaccuracies in the transfer function.

Sammendrag

Eurokode 8, del 2, inneholder ulike metoder for å ta hensyn til asynkron seismisk bevegelse for bruer. Vanlig praksis er å bruke tidshistorieanalyser på grunn av deres gode nøyaktighet, men slike analyser kan være tidkrevende. Målet med oppgaven er derfor å undersøke om andre, raskere, metoder kan produsere tilsvarende resultater, og samtidig undersøke metodenes styrker og svakheter. To elementmodeller ble laget i ANSYS: 1) Chacao bro, en stor to-spenns hengebro, og 2) en fire-spenns bjelkebro for verifisering av implementasjon og resultater.

Single-point responsspektermetoden viste seg å være konservativ, og resultatene samsvarte godt med resultater fra den forenklede metoden i eurokoden. Den forenklede metoden ga likevel en altfor stor respons i det midtre tårnet på Chacao bro, og metodens pseudo-statiske forskyvninger klarte ikke å ta hensyn til effekter fra asynkron seismisk bevegelse.

Multi-point responsspektermetoden i ANSYS var den klart raskeste og mest brukervennlige metoden. I tillegg var metodens resultater nærmest resultatene fra tidshistorieanalysen. Resultatene fra de to bromodellene førte imidlertid til forskjellige observasjoner. Responsen i bjelkebroen ble overestimert, mens responsen i Chacao bro ble noe underestimert. Metoden viste seg å være sensitiv i forhold til konstruksjonens konfigurasjon og stivhet. Derfor kan små og stive konstruksjoner samt komponenter som strekker seg over flere opplegg bli kraftig overestimert ved bruk av metoden. På den annen side kan svært gode resultater oppnås for store og myke konstruksjoner der komponentene kan bevege seg uavhengig av hverandre.

Ved bruk av Der Kiureghian og Neuenhofers responsspektermetode ble det beregnet både forskyvninger og rotasjoner. Eurokodens forenklede versjon ga identiske resultater og dens forenklinger ble derfor rettferdiggjort. På grunn av unøyaktigheter i konverteringsfunksjonen ble ikke krefter og momenter beregnet.

Preface

This thesis was written as part of the Master's Program for Civil and Environmental Engineering at the Norwegian University of Science and Technology. Among the possible fields of study offered by the Master's Program, we have chosen Structural Engineering with Structural Dynamics as field of specialization.

Even though earthquakes of significance are rare in Norway, our fascination has grown throughout the studies. Lectures given by Professor Amir M. Kaynia and Anders Rønnquist and Asscociate Professor Ole Øiseth have been encouraging and essential for our interest in the field of study. When Aas-Jakobsen AS presented an opportunity to examine a tremendous two-span suspension bridge located in one of the most seismically active areas on earth, we were immediately excited. The thesis deals with asynchronous seismic excitation of bridges, a field of engineering with lack of competence in Norway. The opportunity to acquire knowledge within such an advanced field of study was very motivating for both of us.

We would like to express our gratitude to Aas-Jakobsen AS for providing us with access to the Chacao Bridge project. Special thanks go to Lars Halvor Kaasa for help with setting up the finite element model of the Chacao Bridge. His guidance in finite element modeling is greatly appreciated.

Finally, we would like to thank our supervisor Prof. Amir M. Kaynia. His expertise and guidance in Earthquake Engineering has been essential for this thesis. He has motivated us, answered questions, suggested topics of examination, and been available at weekly meetings. For this, we would like to express our deepest appreciation.

Trondheim, June 11th 2017

Herman Høy   Nils Henrik Haughovd

Contents

List of Figures

List of Tables

List of Acronyms

PGD Peak ground displacement

PGA Peak ground acceleration

PSD Power spectral density

DOF Degree of freedom

MDOF Multi degree of freedom

RSA Response spectrum analysis

SPRS Single-point response spectrum

MPRS Multi-point response spectrum

THA Time history analysis

EC8-1 Eurocode 8: Part 1

EC8-2 Eurocode 8: Part 2

SRSS Square root of the sum of squares

CQC Complete quadratic combination

SSI Soil-structure interaction

BC Boundary condition

Chapter 1

Introduction

1.1 Background

Aas-Jakobsen in Oslo has in a multinational project, designed a bridge that will connect Chile's largest island to the mainland (Aas-Jakobsen, 2014). More specific, the Chacao Bridge will be crossing the Chacao Channel, linking Chiloé to mainland Chile. A study carried out in 2001 identified two seismic sources in the region of interest: a subduction source between the Nazca Plate and the South American Plate, and a crustal source located on the Gulf of Ancud Fault (Aas-Jakobsen et al., 2016d). The Bridge's location is marked in Figure 1.1, and is one of the most seismically active areas on earth.

Figure 1.1: Local and global location of the Chacao Bridge (Aas-Jakobsen et al., 2016d)

Figure 1.2: Illustration of the Chacao Bridge (Aas-Jakobsen, 2014)

The Chacao Bridge is designed as a 2750m long steel girder supported by three massive concrete pylons (Aas-Jakobsen, 2014). See Figure 1.2 for illustration. The great length of the Bridge may introduce additional response caused by time-space variation of the seismic ground motion. Subsequently, in cooperation with Aas-Jakobsen, the authors have been set to investigate various methods for seismic design of bridges. Aas-Jakobsen is particularly interested in the functionality of a multi-point response spectrum analysis, and its possibility to replace the traditional single-point response spectrum analysis.

1.1.1 Scope and Limitations

The main objective of this thesis is to compare and investigate strengths and weaknesses of various methods which account for asynchronous seismic excitation of bridges. The choice of methods is based on recommendations from Eurocode 8, part 2 for bridges (EC8-2). A total of six methods are investigated, and includes methods from both the frequency and the time domain:

- Time history analysis

- A simplified method from EC8-2

- Single-point response spectrum analysis

- Multi-point response spectrum analysis

- The multi-point response spectrum analysis by Armen Der Kiureghian and Neuenhofer

- EC8-2's simplified version of the multi-point response spectrum analysis by Armen Der Kiureghian and Ansgar Neuenhofer

Two finite element models are developed in ANSYS Mechanical APDL (ANSYS inc., 2016): The Chacao Bridge and a four-span beam bridge for verification of implementation and results. Modelling of the Chacao Bridge is carried out on the basis of an already constructed model in RM-Bridge (Incorporated Bentley Systems, 2016) by Aas-Jakobsen in Oslo. However, due to advanced interaction between concrete and steel, the south approach bridge is neglected. The four span beam bridge is modeled as 2-dimensional, and time histories and response spectra are limited to excitation in the longitudinal direction.

All analyses are carried out in ANSYS, with the exception of the MPRS method by Der Kiureghian and Neuenhofer. The method is not available in ANSYS, and is implemented manually using MatLab (MathWorks, 2017). However, due to the complexity of the Chacao Bridge, Der Kiureghian and Neuenhofer's method is restricted to the four span beam bridge.

1.1.2 Structure of the Report

A short description of the content in each chapter is listed below:

Chapter 2 provides the theoretical background of spatial variability, and derives the mathematical expression of each effect based on a coherency model. It also includes a theoretical description of each method.

Chapter 3 gives detailed descriptions of both finite element models. It also compares the models of the Chacao Bridge developed in ANSYS and RM-Bridge.

Chapter 4 provides descriptions of how the methods are implemented on both finite element models, and the development of seismic input motions.

Chapter 5 presents a selection of the results. It also lists the naming convention and orientation of all structural components.

Chapter 6 compares the shape and magnitude of the results presented in Chapter 5. It also discusses the origin of deviations.

Chapter 7 describes the implementation of analyses designed to explore the origin of unexpected effects.

Chapter 8 presents the results from the additional analyses conducted in Chapter 7.

Chapter 9 discusses if the results from the additional analyses can explain the unexpected results from Chapter 5.

Chapter 10 states the reliability, strengths, and weaknesses of each method.

Chapter 2

Theory

2.1   Spatial Variability

> The term "spatial variation of seismic ground motions" denotes the differences
> in the amplitude and phase of seismic motions recorded over extended areas.
>
> <div align="right">Zerva (2016)</div>

Zerva (2016) claims that one of the factors causing spatial variation, is the transmission of waves through different earth strata to the ground surface. This is also the main focus in the present thesis. In this paper, spatial variability is described by a coherency model developed by Der Kiureghian (1996). The model includes effects from four phenomena: the incoherence effect, the wave-passage effect, the attenuation effect and the site-response effect. The attenuation effect takes into account that amplitudes decrease due to attenuation from wave scattering, material damping and geometric spreading. It can be proven that the attenuation effect has little influence on the coherency function; consequently, it has not been included in this thesis. Even though the attenuation effect is neglected in the following derivation, it may have an impact on long-span bridges.

Der Kiureghian (1996) describes spatial variability with use of auto- and cross-power spectral density functions, and uses a coherency function to describe each effect separately. Therefore, before explaining spatial variability in detail, it is necessary to understand the theory behind auto- and cross-power spectral densities.

A stationary process, $a(t)$, can be described as the sum of discrete frequency components. All components have uncorrelated amplitudes A_i, random independent phase angles

ϕ_i and frequencies ω_i

$$a(t)^d = \sum_{i=1}^{n} A_i \cos(\omega_i t + \phi_i) \tag{2.1}$$

where t is time, $\omega_i = \omega_1 + (i+1)\Delta\omega$ and $i = 1,2,...,n$. All amplitudes have mean squares equal to σ_i^2 and zero mean. In the following equations, index k and l denote two subsequent foundation supports with response $a_k(t)$ and $a_l(t)$. The auto-correlation function for $a(t)$ at support k is given by (2.2), which describes the correlation between movements at time instance t and $t + \tau$.

$$E[a_k(t)a_k(t+\tau)]^d = \sum_{i=1}^{n}\sum_{j=1}^{n} E[A_i A_j \cos(\omega_i t + \phi_i)\cos(\omega_j(t+\tau)+\phi_j)] \tag{2.2}$$

By using that ϕ_i is a random variable, $E[A_i^2] = \sigma_i^2$, $E[A_i] = E[A_j] = 0$ and the trigonometric identity $\cos(a)\cos(b) = \frac{1}{2}[\cos(a-b)+\cos(a+b)]$, (2.2) is reduced to:

$$E[a_k(t)a_k(t+\tau)]^d = \frac{1}{2}\sum_{i=1}^{n}\sigma_i^2 \cos[\omega_i(\tau)] \quad \text{for} \quad i = j$$
$$= 0 \qquad\qquad\qquad\quad \text{for} \quad i \neq j \tag{2.3}$$

The auto-power spectral density (PSD) is obtained by taking the Fourier transform of (2.3). It describes the power of the response at all frequencies. For a continuous signal, the auto-PSD can be expressed as (Newland, 2012):

$$G_{a_k a_k}(\omega) = \frac{1}{2\pi}\int_{-\infty}^{\infty} E[a_k(t)a_k(t+\tau)]e^{-i\omega t}dt \tag{2.4}$$

However, Der Kiureghian (1996) uses a discrete representation of the response. Therefore, it is necessary to adapt the discrete-time Fourier transform of $\cos(at)$, which is equal to $\delta(\omega - a) + \delta(\omega + a)$ (Wikipedia, 2017). The auto-PSD of (2.3) becomes:

$$G_{a_k a_k}(\omega)^d = \frac{1}{4}\sum_{i=1}^{n}\sigma_i^2[\delta(\omega_i - \omega) + \delta(\omega_i + \omega)] \tag{2.5}$$

In contrast to auto-correlation, cross-correlation describes the correlation between movements at two different support foundations k and l. The Fourier transform of the auto-correlation provides the cross-PSD, $G_{a_k a_l}$.

Finally, the complex non-dimensional coherency function is obtained by combining the

auto- and cross-PSDs (Der Kiureghian, 1996):

$$\gamma_{kl}(\omega) = \frac{G_{a_k a_l}(\omega)}{\sqrt{G_{a_k a_k}(\omega) G_{a_l a_l}(\omega)}} \quad \text{for} \quad G_{a_k a_k}(\omega) G_{a_l a_l}(\omega) \neq 0$$

$$= 0 \qquad\qquad\qquad \text{for} \quad G_{a_k a_k}(\omega) G_{a_l a_l}(\omega) = 0$$

(2.6)

Equation (2.6) provides a statistical measure of the linear dependence between the response at support foundation k and l. Perfect in-phase motions yield $\gamma_{kl}(\omega) = 1$, while $\gamma_{kl}(\omega) = 0$ denotes completely independent motions.

2.1.1 The Incoherence Effect

Similar to (2.1), the acceleration process at support k can be expressed as a sum of discrete frequency components:

$$a_k(t)^d = \sum_{i=1}^{n} A_i \cos(\omega_i t + \phi_i)$$

(2.7)

Two phenomena contribute to the incoherence effect when earthquake-induced motions travel from support k to support l (Der Kiureghian, 1996). Firstly, the ground medium is heterogeneous and leads to scattering of waves. Secondly, the seismic source will always have a certain extent. Therefore, waves will arrive from different segments of the source, which results in superposition of waves. As illustrated in Figure 2.1, this leads to a change in amplitude and phase at support l. Consequently, the acceleration process at support l, a distance d_{kl} from support k, may be expressed by (2.8). Note that the topography and soil conditions in Figure 2.1-2.3 do not reflect reality.

$$a_l(t)^d = \sum_{i=1}^{n} (p_{kl,i} A_i + q_{kl,i} B_i) \cos(\omega_i t + \phi_i + \varepsilon_{kl,i})$$

(2.8)

Where $\varepsilon_{kl,i}$ is the phase difference with variance $\alpha_{kl,i}^2$, and $(p_{kl,i} A_i + q_{kl,i} B_i)$ is the amplitude at support l (Der Kiureghian, 1996). $p_{kl,i} A_i$ determines the contribution from the amplitude at support k, while $q_{kl,i} B_i$ is the incoherent contribution to the amplitude. The index kl, i indicates that $p_{kl,i}$ and $q_{kl,i}$ are dependent on both the distance d_{kl} and the frequency ω_i. Larger distances and higher frequencies tend to increase the incoherence effect.

In addition, by assuming that the two processes $a_k(t)$ and $a_l(t)$ are statistically equivalent, it can be proven that $p_{kl,i} \equiv \cos(\beta_{kl,i})$ and $q_{kl,i} \equiv \sin(\beta_{kl,i})$. Using this in combination
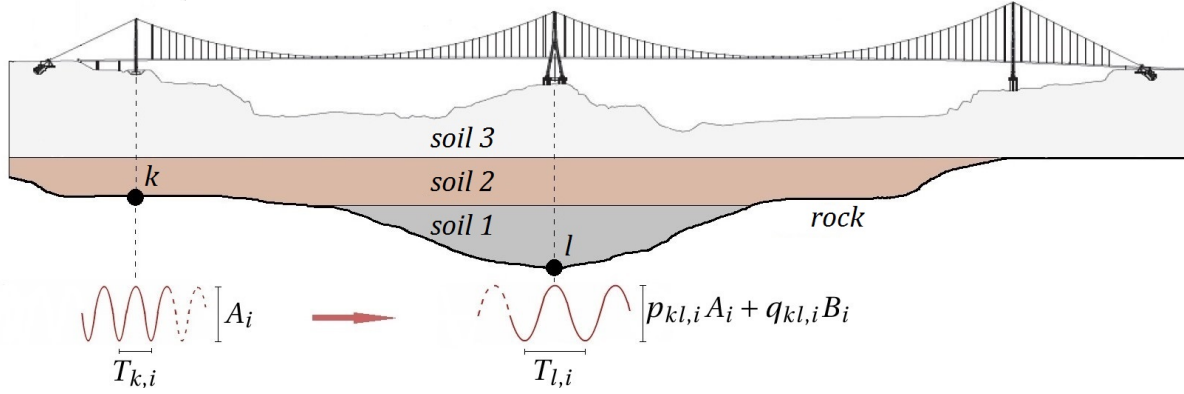
Figure 2.1: Illustrative representation of the incoherence effect

with the procedure developed in Chapter 2.1, the cross-PSD becomes:

$$G^d_{a_k a_l} = \frac{1}{4} \sum_{i=1}^{n} \sigma_i^2 \cos[\beta(d_{kl}, \omega_i)] \exp\left[-\frac{1}{2}\alpha^2(d_{kl}, \omega_i)\right] [\delta(\omega_i - \omega) + \delta(\omega_i + \omega)] \qquad (2.9)$$

By use of (2.5) and converting the discrete equations into continuous forms, (2.9) can be expressed as: $T_{k,i}$ $T_{l,i}$

$$G_{a_k a_l} = \cos[\beta(d_{kl}, \omega_i)] \exp\left[-\frac{1}{2}\alpha^2(d_{kl}, \omega_i)\right] \sqrt{G_{a_k a_k}(\omega) G_{a_l a_l}(\omega)} \qquad (2.10)$$

Finally, the coherency function describing the incoherence effect is obtained by use of (2.6) (Der Kiureghian, 1996):

$$\gamma_{kl}(\omega)^{\text{incoherence}} = \cos[\beta(d_{kl}, \omega_i)] \exp\left[-\frac{1}{2}\alpha^2(d_{kl}, \omega_i)\right] \qquad (2.11)$$

2.1.2   The Wave-Passage Effect

The change in response due to the different arrival time of the waves at different support foundations, is called the wave-passage effect. Time-lag is denoted $\tau_{kl,i}$, and indicates the time difference from waves arriving at support k relative to their arrival at support l (Der Kiureghian, 1996). The acceleration process at support l which includes both the incoherence effect and the wave-passage effect can be expressed as:

$$a_l(t)^d = \sum_{i=1}^{n} (p_{kl,i} A_i + q_{kl,i} B_i) \cos[\omega_i(t - \tau_{kl,i}) + \phi_i + \varepsilon_{kl,i}] \qquad (2.12)$$

The time-lag is based on waves arriving with the same incidence angle, ψ, at both sup-
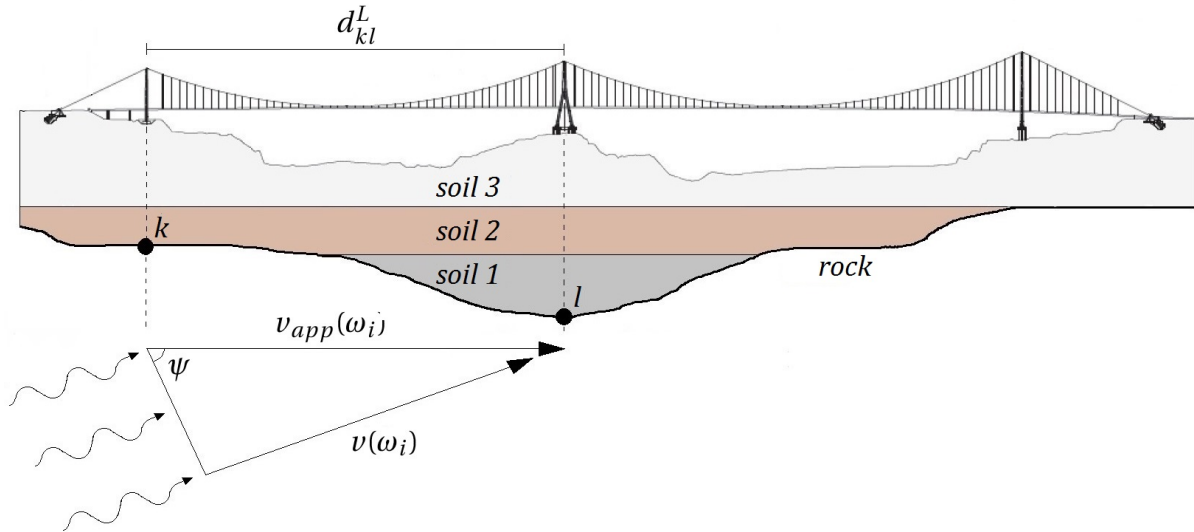
Figure 2.2: Illustrative representation of the wave-passage effect

ports (Der Kiureghian, 1996). Consequently, this limits the equation to only be applicable in situations where it exists one dominant angle of arrival. Since d_{kl}^L corresponds to the projected distance between support k and l, it is common to use an apparent wave velocity. Figure 2.2 illustrates the phenomena, where $v(\omega_i)$ is the wave velocity, ψ is the wave's angle of arrival relative to the ground's normal axis, and $v_{app}(\omega_i)$ is the equivalent velocity propagating parallel to the ground surface.

$$\tau_{kl,i} = \frac{d_{kl}^L \sin(\psi)}{v(\omega_i)} = \frac{d_{kl}^L}{v_{app}(\omega_i)} \tag{2.13}$$

Performing the same procedure as in Chapter 2.1.1, the coherency function describing both the incoherence effect and the wave-passage effect becomes

$$\gamma_{kl}(\omega)^{\text{incoherence}} \gamma_{kl}(\omega)^{\text{wave passage}} =$$
$$\cos[\beta(d_{kl}, \omega_i)] \exp\left[-\frac{1}{2}\alpha^2(d_{kl}, \omega_i)\right] \exp\left[-i\frac{\omega d_{kl}^L}{v_{app}(\omega)}\right] \tag{2.14}$$

where the wave-passage effect is described by:

$$\gamma_{kl}(\omega)^{\text{wave passage}} = \exp\left[-i\frac{\omega d_{kl}^L}{v_{app}(\omega)}\right] \tag{2.15}$$

2.1.3 The Site-Response Effect

The site-response effect accounts for the different soil conditions underneath each support foundation (Der Kiureghian, 1996). It is common to represent soil by a single column, with layers describing varying soil conditions. Independently of the acceleration process at bedrock, different soil conditions will generate a different response at the surface due to the filtering effects in each column. The response amplitude at support k can be described by the frequency response function $H_k(\omega)$ generated by a harmonic motion at bedrock. Transition from the movement at bedrock to the surface can be expressed as

$$G_{a_k a_k}(\omega)^{\text{surface}} = |H_k(\omega)|^2 G_{a_k a_k}(\omega)^{\text{bedrock}} \tag{2.16}$$

where $G_{a_k a_k}(\omega)^{\text{surface}}$ and $G_{a_k a_k}(\omega)^{\text{bedrock}}$ are the auto-PSDs underneath support k at surface and bedrock (Der Kiureghian, 1996). The same procedure applies to support l, and the cross-PSD of the response underneath the two supports are

$$G_{a_k a_l}(\omega)^{\text{surface}} = H_k(\omega) H_l(-\omega) G_{a_k a_l}(\omega)^{\text{bedrock}} \tag{2.17}$$

where $G_{a_k a_l}(\omega)^{\text{bedrock}}$ is the cross-PSD at bedrock. Finally, using (2.6), the coherency function describing the site-response effect becomes

$$\gamma_{kl}(\omega)^{\text{site response}} = \exp\{i[\theta_k(\omega) - \theta_l(\omega)]\} \tag{2.18}$$

where

$$\theta_k(\omega) - \theta_l(\omega) = \tan^{-1} \frac{\text{Im}[H_k(\omega) H_l(-\omega)]}{\text{Re}[H_k(\omega) H_l(-\omega)]} \tag{2.19}$$
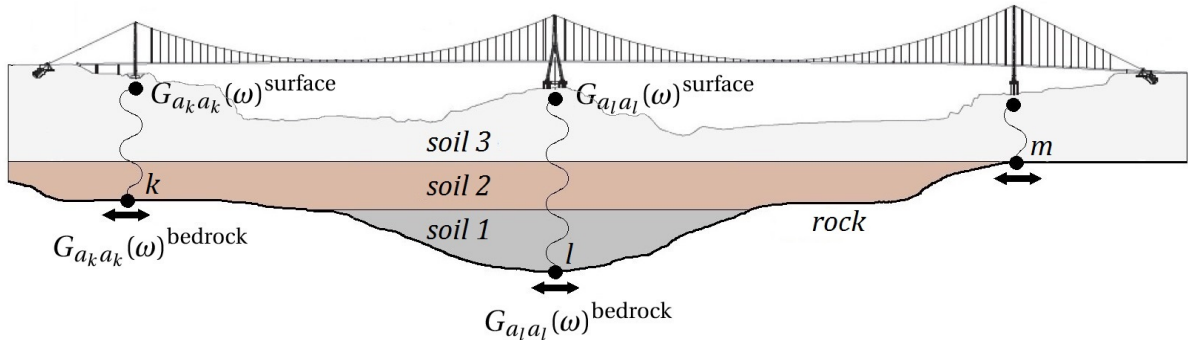
Figure 2.3: Illustrative representation of the site-response effect

2.1.4 Combined Coherency Effect

The coherency function describing spatial variability is equal to the product of the incoherence, wave-passage, and site-response effects:

$$
\begin{aligned}
\gamma_{kl}(\omega) =& \gamma_{kl}(\omega)^{\text{incoherence}} \gamma_{kl}(\omega)^{\text{wave passage}} \gamma_{kl}(\omega)^{\text{site response}} \\
=& \cos[\beta(d_{kl},\omega_i)] \exp\left[-\frac{1}{2}\alpha^2(d_{kl},\omega_i) \right] \\
& \exp\left[-i\frac{\omega d_{kl}^{L}}{v_{app}(\omega)} \right] \exp\left\{ i\left[\theta_k(\omega) - \theta_l(\omega) \right] \right\}
\end{aligned}
\tag{2.20}
$$

2.2 Analyses

Multiple methods exist for estimation of a structure's response to seismic excitation. Due to the Eurocode's reputation as recommended practice, the choice of methods was based on the analyses suggested by EC8-2. Analyses were chosen from both time and frequency domain. Analyses conducted in the time domain have a deterministic approach, while frequency dependant methods are, for the most part, based on statistics. Therefore, the analyses are not expected to produce identical results. The analyses of interest include time history analysis, single-point- and multi-point response spectrum analyses, a simplified method from EC8-2, and Der Kiureghian and Neuenhofer's multi-point response spectrum method.

2.2.1 The Simplified Method

For locations with low seismicity, EC8-2 allows the use of a simplified design criteria (EC8-2, 3.3). The method will, in this thesis, be referred to as *the simplified method*. Spatial variability of the seismic action is accounted for by combining the inertia response and effects from pseudo-static displacements. The inertia response is calculated by use of a single input seismic action for the entire bridge, determined by the poorest soil conditions. Furthermore, pseudo-static forces are calculated by imposing two sets of horizontal displacement patterns, set A and set B. The sets are applied separately and are considered by EC8-2 as the two most critical patterns. Set A assumes that all foundations are displaced in the same direction with varying amplitude, while Set B assumes each support foundation to move in opposite direction relative to its adjacent support. See Figure 2.4 and 2.5 for an illustrative representation of the pseudo-static displacement patterns.

Set A is based on displacements d_{ri}, relative to a reference support $i = 0$. The relative displacements are functions of the design ground displacement, d_g, at support i, the distance, L_i, from support i to the reference support, and L_g, the shortest distance assumed to give completely uncorrelated motions. All displacements are applied simultaneously and defined by:

$$d_{ri} = \varepsilon_r L_i \le d_g \sqrt{2} \qquad (2.21)$$

$$\varepsilon_r = \frac{d_g \sqrt{2}}{L_g} \qquad (2.22)$$

Design ground displacements are defined in EC8-1 (3.2.2.4), and are based on values from an horizontal elastic response spectrum:

$$d_g = 0.025 \cdot a_g \cdot S \cdot T_C \cdot T_D \qquad (2.23)$$

The more complex displacement pattern in Set B assumes each intermediate support i to be displaced Δd_i relative to both its adjacent supports. Δd_i is a function of ε_r, the factor β_r and $L_{av,i}$ the average distance from support i to its adjacent supports $i-1$ and $i+1$. Note that the maximum value of ε_r is used in cases where a change of ground type appears between two supports. In addition, β_r is 0.5 for constant ground types and 1.0 for varying
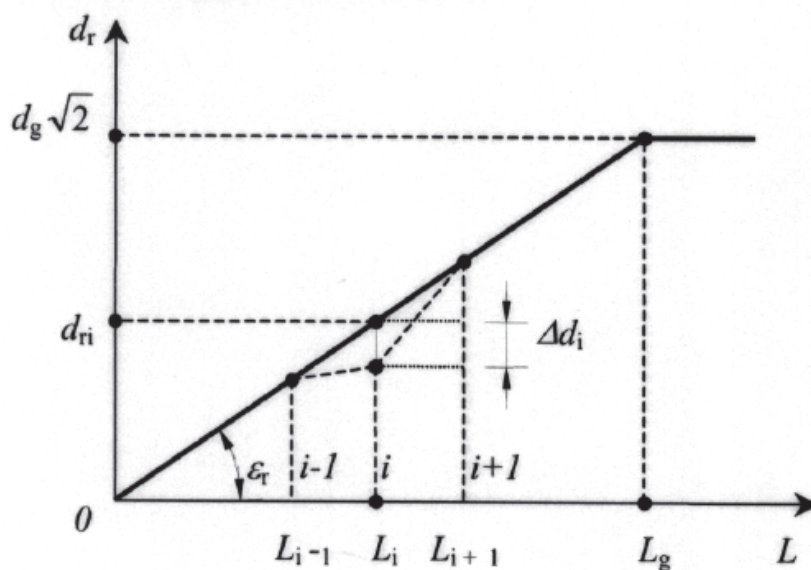
Figure 2.4: Set A in the simplified method (EC8-2, Figure 3.1)

ground types between supports. The total displacement, d_i, at each support is defined by (2.24)-(2.26).

$$\Delta d_i = \beta_r \varepsilon_r L_{\alpha v,i} \tag{2.24}$$

$$d_i = \pm \Delta d_i / 2 \tag{2.25}$$

$$d_{i+1} = \mp \Delta d_{i+1} / 2 \tag{2.26}$$

Total design effect, E_{tot}, is obtained by combining the inertia response and the most severe effect from the pseudo-static displacements. Combination is carried out by use of the square root of the sum of squares (SRSS), expressed in (2.27). However, the maximum effect from set A and B do not need to be combined.

$$E_{tot} = \sqrt{E_{setA}^2 + E_{setB}^2 + E_{inertia}^2} \tag{2.27}$$

In studies carried out by Sextos and Kappos (2005, 2009), the simplified method was compared to the more refined method provided in the informative Annex of EC8-2. The study included 27 bridges subjected to 278 spatially variable earthquake ground motion scenarios. Results from the study indicate that the simplified method is an efficient method for including effects of asynchronous excitation. Furthermore, Sextos and Kappos (2005, 2009) states that the simplified method produces minor effects for short bridges on uniform ground conditions; while effects from asynchronous excitation increase for longer bridges, longer spans
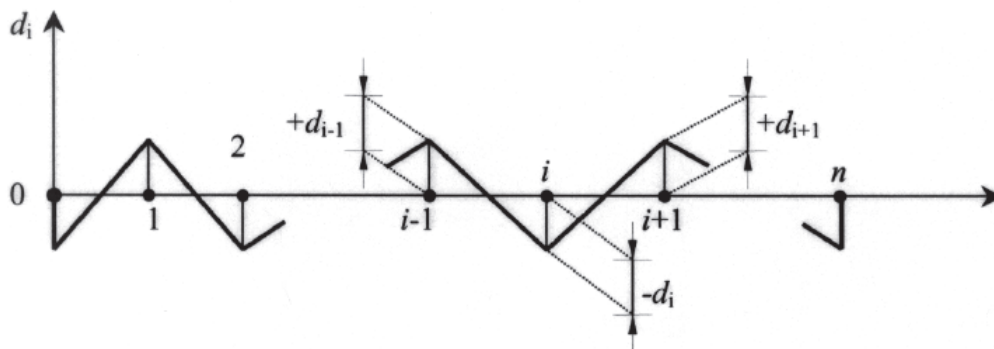
Figure 2.5: Set B in the simplified method (EC8-2, Figure 3.2)

and non-uniform soil conditions.

The study also enlightens disadvantages regarding the simplified method. Firstly, the method was developed to estimate additional member forces due to asynchronous excitation. Consequently, it cannot be used to estimate actual displacements. Secondly, the design effect of asynchronous excitation proves to be minor compared to the refined method. Sextos and Kappos (2005, 2009) consider the SRSS-rule to suppress the effect of asynchronous excitation when combining the three load cases. A suggestion was made to use direct summation.

The third disadvantage is the inability to predict the location of the most unfavourable affected support foundation. This is due to the method's use of pseudo-static displacements. Consequently, it cannot capture the dynamic excitation of higher modes, which is an effect often observed during asynchronous excitation. The effect is more severe for curved bridges as the excitation of higher modes are expected to be of greater significance.

Sextos and Kappos (2005, 2009) suggest two improvements to narrow the gap between the simplified method and the refined analysis. As an alternative to direct summation, they recommend to increase the pseudo-static displacements by a factor of 5.6. Furthermore, as a solution to the methods inability to locate the most unfavourable affected support foundation, they introduce an average increase ratio $\bar{\rho}$. The final design value at each support i, denoted $M_{sd,i}$, is given by (2.28)-(2.30).

$$M_{sd,i} = M_{i,inertia} \cdot \bar{\rho} \tag{2.28}$$

$$\bar{\rho} = \frac{1}{n} \sum_{i=1}^{n} \rho_i \tag{2.29}$$

$$\rho_i = \frac{\sqrt{M_{i,setA}^2 + M_{i,setB}^2 + M_{i,inertia}^2}}{M_{i,inertia}} \tag{2.30}$$

2.2.2 Time History Analysis

Time history analyses (THA) use ground displacement, velocity or acceleration series as load input. A THA is computationally demanding, but in return one may get accurate results if applied correctly. The equation of motion for a structure subjected to earthquake-induced ground acceleration $\ddot{u}_g(t)$ is

$$\mathbf{m}\ddot{\mathbf{u}} + \mathbf{c}\dot{\mathbf{u}} + \mathbf{k}\mathbf{u} = -\mathbf{m}\iota\ddot{u}_g(t) \tag{2.31}$$

where ι is the influence vector (Chopra, 2011). The equation of motion for multi degree of freedom (MDOF) systems can be solved using various methods. One approach is the mode superposition method, which calculates the displacement, **u**, as the superposition of modal contributions. The approach is expressed in (2.32), where ϕ_n is the shape function and q_n is modal coordinate of mode number n. However, the mode superposition method can only be used for simple excitations in the elastic range, and is not be applicable for seismic loading of suspension bridges.

$$\mathbf{u} = \sum_{n=1}^{N} \phi_n q_n(t) \tag{2.32}$$
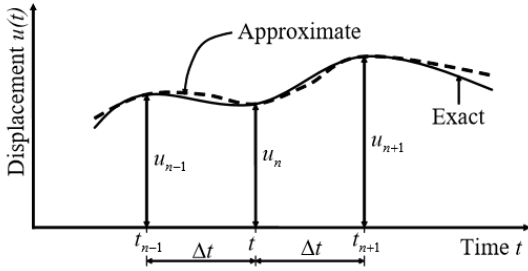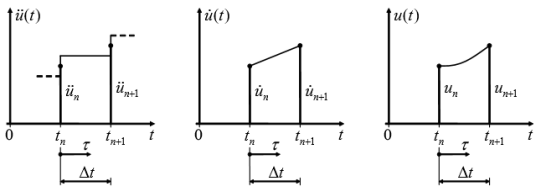
The second approach is use of numerical methods, such as time-stepping methods. Numerical methods can be explicit or implicit, conditionally or unconditionally stable, linear or nonlinear. Explicit methods require many steps, but at low cost per increment. Implicit methods require fewer steps, but at higher cost per increment. In addition, explicit methods are conditionally stable, meaning that convergence depends on the chosen time step. Using increments larger than the critical time step, Δt_{cr}, results in the solution "blowing up" (Mathisen, 2016a).

There are several different time-stepping methods depending upon the chosen way to integrate the accelerations. Two methods are considered in this thesis: the central difference method and Newmark's method. The central difference method is often used for analyses of impact and explosion response, and is an explicit and conditionally stable method (Rönnquist, 2016). It is based on time derivatives of the displacement and described in full in Table 2.1. Newmark's method is implicit, and its stability depends on the chosen way to integrate the acceleration. The linear acceleration method is more accurate than the constant

acceleration method, but in return, the constant acceleration method is unconditionally stable while the linear method is only conditionally stable.

Structural vibration problems do not require small time steps to capture the dynamic effects. Therefore, Mathisen (2016a) recommends using implicit methods, such as the constant acceleration method described in Table 2.1.

Table 2.1: Central difference and Newmark's method (Chopra, 2011; Mathisen, 2016a,b)

Central difference method	Newmark's method (constant acceleration method)

$$\ddot{u}_0 = \frac{p_0 - c\dot{u}_0 - k\dot{u}_0}{m}$$

$$\ddot{u}(\tau) = \tfrac{1}{2}(\ddot{u}_{i+1} + \ddot{u}_i)$$

$$u_{-1} = u_0 - \Delta t\,\dot{u}_0 + \frac{(\Delta t)^2}{2}\ddot{u}_0$$

$$\dot{u}(\tau) = \dot{u}_i + \frac{\tau}{2}(\ddot{u}_{i+1} + \ddot{u}_i)$$

$$\hat{k} = \frac{m}{(\Delta t)^2} + \frac{c}{2\Delta t}$$

$$\dot{u}_{i+1} = \dot{u}_i + \frac{\Delta t}{2}(\ddot{u}_{i+1} + \ddot{u}_i)$$

$$a = \frac{m}{(\Delta t)^2} - \frac{c}{2\Delta t}$$

$$u(\tau) = u_i + \dot{u}_i\tau + \frac{\tau^2}{4}(\ddot{u}_{i+1} + \ddot{u}_i)$$

$$b = k - \frac{2m}{(\Delta t)^2}$$

$$u_{i+1} = u_i + \dot{u}_i\Delta t + \frac{(\Delta t)^2}{4}(\ddot{u}_{i+1} + \ddot{u}_i)$$

$$\hat{p}_i = p_i - au_{i-1} - bu_i$$

$$u_{i+1} = \frac{\hat{p}_i}{\hat{k}}$$

If required:

$$\dot{u}_i = \frac{u_{i+1} - u_{i-1}}{2\Delta t}$$

$$\ddot{u}_i = \frac{u_{i+1} - 2u_i + u_{i-1}}{(\Delta t)^2}$$

2.2.3 Response Spectrum Analysis

With respect to computational time, response spectrum analyses (RSA) are far more effi-cient than THAs. The concept of RSAs was developed by Maurice A. Biot in 1941 (Ye et al., 2012), and is today a recognized method for seismic design of structures. RSA is based on mode superposition, and calculates the maximum response contribution from each natural vibration mode due to excitation based on a response spectrum (Chopra, 2011). The elastic response spectrum is a function of maximum acceleration, velocity or displacement versus the natural period of the structure. The spectrum accounts for the ground motion and the vibrational properties of the structure (Priestley et al., 1996). However, the number of cycles or duration of the time series are not represented.

The equations provided in EC8-1 (3.2.2.2) generates an elastic design response spectrum with shape as depicted in Figure 2.6. It takes into account the structural damping, vibration period and the soil- and seismological characteristics. Furthermore, a spectrum represents a number of possible earthquake events, and can be created in two manners:

- A standardized response spectrum from EC8-1

- A site-specific response spectrum based on actual earthquake accelerograms

Complex and large structures include a large number of DOFs. Consequently, a large number of modes must be embedded in the analysis to yield representative results. EC8-2
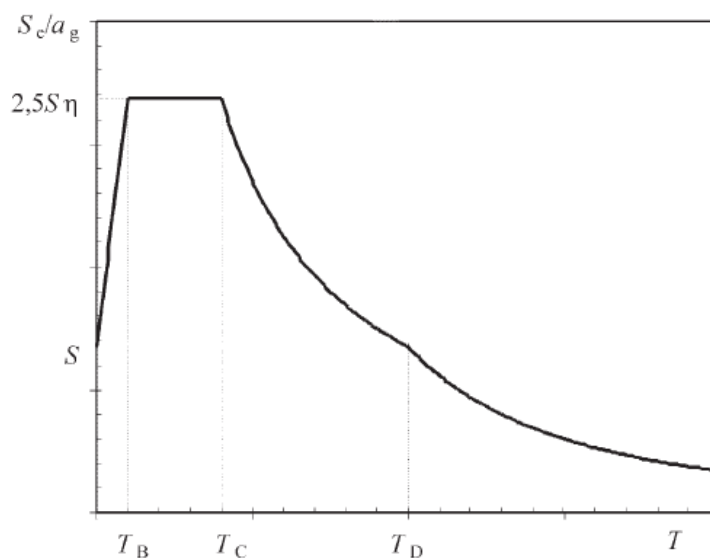
Figure 2.6: Elastic response spectrum from EC8-1(Figure 3.1)

requires that 90% of the effective modal mass must be represented by the modes. Because the response usually is dominated by modes of lower frequencies; the required number of modes will drop greatly due to the requirement. In addition, when combining the modal effects, EC8-2 recommends use of the SRSS-rule in (2.33), where i is the mode number and n is the number of modes included.

$$E = \sqrt{\sum_{i=1}^{n} E_i^2} \tag{2.33}$$

The SRSS-rule does not account for the coupling of modes. Therefore, the combination rule is not conservative for summation of modes with closely spaced periods. EC8-2 considers two natural periods as closely spaced if they satisfy the condition in (2.34). For closely spaced modes i and j, the National Annex requires use of the complete quadratic combination (CQC) rule in (2.35).

$$\frac{0.1}{0.1 + \sqrt{\xi_i \xi_j}} \le \rho_{ij} = T_i / T_j \le 1 + 10\sqrt{\xi_i \xi_j} \tag{2.34}$$

$$E = \sqrt{\sum_{i=1}^{n} \sum_{j=1}^{n} E_i r_{ij} E_j} \tag{2.35}$$

T_i and T_j are natural periods with damping ratio ξ_i and ξ_j, and the correlation factor r_{ij} is given as:

$$r_{ij} = \frac{8\sqrt{\xi_i \xi_j}(\xi_i + \rho_{ij}\xi_j)\rho_{ij}^{3/2}}{(1 - \rho_{ij}^2)^2 + 4\xi_i \xi_j \rho_{ij}(1 + \rho_{ij}^2) + 4(\xi_i^2 + \xi_j^2)\rho_{ij}^2} \tag{2.36}$$

Furthermore, for long span structures with members spanning 20 meters or more, EC8-1(4.3.3.5.2) requires combination of the effects from the three earthquake components. Two alternative summation methods are provided: the SRSS-rule in (2.37), or the most severe combination in (2.38)-(2.40)

$$E = \sqrt{E_x^2 + E_y^2 + E_z^2} \tag{2.37}$$

$$E = E_x \pm 0.30E_y \pm 0.30E_z \tag{2.38}$$

$$E = 0.30E_x \pm E_y \pm 0.30E_z \tag{2.39}$$

$$E = 0.30E_x \pm 0.30E_y \pm E_z \tag{2.40}$$

It is worth noticing that the maximum peak response from a THA and a RSA deviates for MDOF systems. Deviation is caused by summation of modal contributions. Priestley et al. (1996) point out that RSAs are only valid for linear elastic systems and small displacements. Large deformations expose the structure to nonlinear behaviour. Consequently, mode shapes will be dependent on the displacement amplitude and are no longer simple harmonics. The principle of superposition will no longer be valid.

In addition, Ye et al. (2012) stress that the classical response spectrum method is based on uniform excitations. Therefore, additional effects, such as local soil properties, loss of coherence, and the wave passage effect are not included. As an alternative, one may perform an RSA based on multi-support excitations. This is discussed in chapter 2.2.4.

2.2.4 Multi-Point Response Spectrum Analysis

Long-span structures with multiple supports may respond differently to seismic actions than what is estimated by the SPRS method. The effect of spatial variability will change the response between supports. In order to account for time-space variation of the seismic action, a large number of methods have been presented throughout time.

The principle of a multi-point response spectrum analysis (MPRS) is illustrated in Figure 2.7. As depicted, the SPRS analysis uses a single spectrum as seismic input, while the MPRS analysis uses different response spectra at each support. Berrah and Kausel (1992) proposed a modified response spectrum method, and introduced correction factors to simulate multi-support excitation. The method accounts for local seismic and structural properties by adjusting each spectral value with a correction factor. In addition, to simulate time-space variation, another coefficient is used to modify the mode correlation coefficients (Ye et al., 2012). However, the method presented by Berrah and Kausel (1992) does not account for pseudo-static effects.
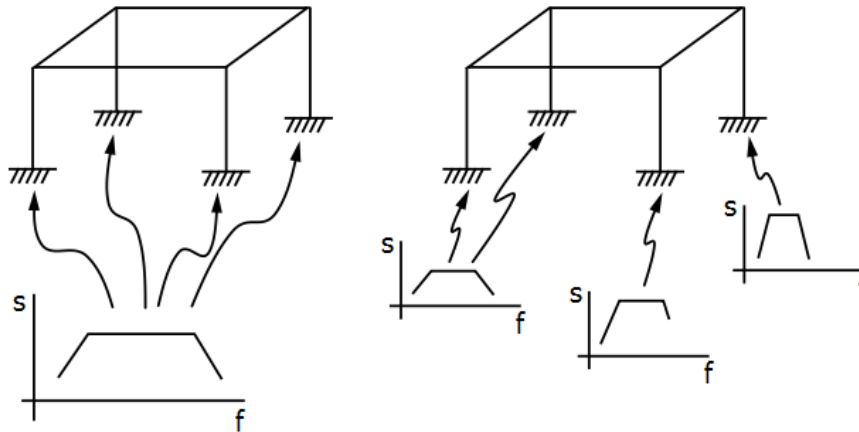
Figure 2.7: The principle of an MPRS analysis (ANSYS inc., 2017d)

Another method was presented by Yamamura and Tanaka (1990). They divided adjacent supports into groups of correlated and uncorrelated supports. Adjacent supports on continuous soil were assumed to move fully correlated, while a change of soil conditions gave fully uncorrelated motions.

Nevertheless, one of the most recognized methods for estimating response from multi-support excitation, was developed by Der Kiureghian and Neuenhofer (1992). The rigorous method is based on cross-PSDs, and considers both the incoherence effect, the wave-passage effect, and the site-response effect. A detailed description of the methodology is presented in Chapter 2.2.5. However, Der Kiureghian and Neuenhofer's method is by most designers considered as too cumbersome. Therefore, current research works on simplifying the method (Ye et al., 2012).

There are multiple advantages by performing an MPRS analysis instead of a THA. In a THA, a numerous amount of analyses are required in order to get a reliable and statistically stable response. Conversely, an MPRS analysis is based on statistics which implies that only one analysis is necessary to avoid statistical outliers. An MPRS analysis is also a lot less computationally demanding compared to a THA. These two advantages makes the MPRS method appealing to engineers working around the clock.

2.2.5   MPRS Method of Der Kiureghian and Neuenhofer

Der Kiureghian and Neuenhofer's method is perhaps the most recognized method for estimating response in a MPRS analysis. In fact, a slightly simplified version is to be found in EC8-2(Annex D.3.4.3). In this report, only a summary of the most important equations is presented. Nakamura et al. (1993, Fig. 2.2) have developed a data flow diagram of the method, which can be seen in Figure 2.8. For a complete understanding and derivation of equations, see Der Kiureghian and Neuenhofer (1992).

Equation of Motion for a Multi-Supported Structure

The method is based on the equation of motion for a discretized system (Clough and Penzien, 1993) with n unconstrained DOFs and m constrained support DOFs.

$$\begin{bmatrix} M & M_c \\ M_c^T & M_g \end{bmatrix} \begin{Bmatrix} \ddot{x} \\ \ddot{u} \end{Bmatrix} + \begin{bmatrix} C & C_c \\ C_c^T & C_g \end{bmatrix} \begin{Bmatrix} \dot{x} \\ \dot{u} \end{Bmatrix} + \begin{bmatrix} K & K_c \\ K_c^T & K_g \end{bmatrix} \begin{Bmatrix} x \\ u \end{Bmatrix} = \begin{Bmatrix} 0 \\ F \end{Bmatrix} \tag{2.41}$$
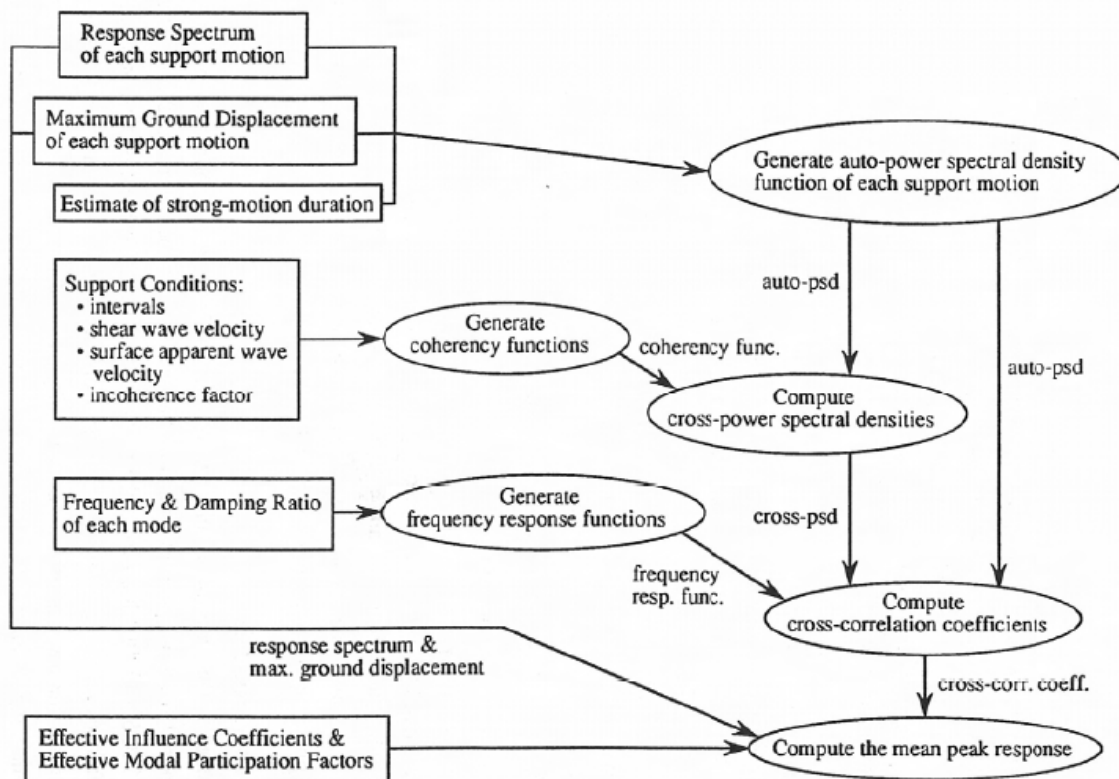
Figure 2.8: Flowchart for Der Kiureghian and Neuenhofer's method (Nakamura et al., 1993, Fig. 2.2)

The equation of motion is described by (2.41). It is organized such that M, C, and K are nxn mass, damping, and stiffness matrices of unconstrained DOFs; M_g, C_g, and K_g are mxm mass, damping, and stiffness matrices of constrained DOFs; M_c, C_c, and K_c are nxm mass, damping, and stiffness coupling matrices. Similarly, $\ddot{u}$, $\dot{u}$, and u are the acceleration, velocity and displacement at the support DOFs, while $\ddot{x}$, $\dot{x}$, and x are the acceleration, velocity and displacement at the unconstrained DOFs. F is an n-vector which provides forces at the support DOFs. In this chapter index $k = 1, ..., m$ and $l = 1, ..., m$ denote the support DOF number; $i = 1, ..., n$ and $j = 1, ..., n$ denote the natural frequency number, mode shape, and unconstrained DOFs.

$$R = -K^{-1}K_c \qquad (2.42)$$

R is the influence matrix, where r_k and r_l are the kth and l^{th} columns respectively.

Furthermore, β is the modal participation factor and is defined as

$$\beta_{ki} = \frac{\phi_i^T(Mr_k + M_c I_k)}{\phi_i^T M \phi_i} \qquad (2.43)$$

$$\beta_{lj} = \frac{\phi_j^T(Mr_l + M_c I_l)}{\phi_j^T M \phi_j} \qquad (2.44)$$

where ϕ_i is the ith mode shape, and I_k is the kth column of an mxm identity matrix.

Moreover, one may divide the response into a static and a dynamic component. It can be shown that the effective influence coefficient, a, contributes to a pseudo-static solution, while the effective modal participation factor, b, contributes to the dynamic solution.

$$b_{ki} = \mathbf{q}^T \phi_i \beta_{ki} \qquad (2.45)$$

$$b_{lj} = \mathbf{q}^T \phi_i \beta_{lj} \qquad (2.46)$$

$$a_k(t) = \mathbf{q}^T r_k \qquad (2.47)$$

$$a_l(t) = \mathbf{q}^T r_l \tag{2.48}$$

where $\boldsymbol{q}$ is a 1xn vector and is called a transfer vector. A generic response quantity of interest, $z(t)$, can in general be expressed as a linear function of the nodal displacements. In other words, the transfer vector takes care of the transition of displacements to the response quantity of interest, e.g. forces and moments.

MPRS Method of Der Kiureghian and Neuenhofer

Der Kiureghian and Neuenhofer's method is rooted in response spectra, see Chapter 2.2.3, which have been adjusted for local soil conditions. Based on the response spectra, D, the first order approximation of the power spectral densities (PSD) can be estimated by

$$G_{uu}(\omega)_1 = \frac{\omega^{p-2}}{\omega^p + \omega_f^p} \left(\frac{2\xi\omega}{\pi} + \frac{4}{\pi\tau} \right) \left[\frac{D(\omega,\xi)}{p_s(\omega)_0} \right]^2 , \omega \geq 0 \tag{2.49}$$

$$G_{\ddot{u}\ddot{u}}(\omega)_1 = \frac{\omega^{p+2}}{\omega^p + \omega_f^p} \left(\frac{2\xi\omega}{\pi} + \frac{4}{\pi\tau} \right) \left[\frac{D(\omega,\xi)}{p_s(\omega)_0} \right]^2 , \omega \geq 0 \tag{2.50}$$

where ω is the frequency, ω_f and p are parameters, ξ is the damping ratio, τ is the strong-motion duration of the earthquake, p_s is the peak factor for the oscillator response, and the index 1 refers to a first order approximation. The term $\frac{\omega^p}{\omega^p + \omega_f^p}$ is a factor which corrects spectral values for low frequencies. The modification factor is necessary in order to compensate for violation of the assumption of stationarity at low frequencies.

By rearranging (2.9), it is possible to calculate the cross-PSD between supports k and l.

$$G_{u_k u_l}(\omega) = -\omega^{-4} \gamma_{kl}(i\omega) \left[G_{\ddot{u}_k \ddot{u}_k}(\omega) * G_{\ddot{u}_l \ddot{u}_l}(\omega) \right]^{1/2} \tag{2.51}$$

$$G_{u_k \ddot{u}_l}(\omega) = -\omega^{-2} \gamma_{kl}(i\omega) \left[G_{\ddot{u}_k \ddot{u}_k}(\omega) * G_{\ddot{u}_l \ddot{u}_l}(\omega) \right]^{1/2} \tag{2.52}$$

$$G_{\ddot{u}_k \ddot{u}_l}(\omega) = \gamma_{kl}(i\omega) \left[G_{\ddot{u}_k \ddot{u}_k}(\omega) * G_{\ddot{u}_l \ddot{u}_l}(\omega) \right]^{1/2} \tag{2.53}$$

where γ_{kl} is the coherency function from Chapter 2.1.

In order to calculate the correlation coefficients, the frequency transfer functions, $H_i(i\omega)$ and $H_i(-i\omega)$, are required.

$$H_i(i\omega) = \frac{1}{\omega_i^2 - \omega^2 + i2\xi_i\omega_i\omega} \qquad (2.54)$$

$$H_i(-i\omega) = \frac{1}{\omega_i^2 - \omega^2 - i2\xi_i\omega_i\omega} \qquad (2.55)$$

ω_i denotes the structure's natural frequency number i. Correspondingly, ξ_i denotes the damping in mode number i, while i is the imaginary unit.

Assuming that the displacement function u_k is stationary and has zero mean, the root mean square, σ^2, can be calculated.

$$\sigma_{u_k}^2 = \int_{-\infty}^{\infty} G_{u_k u_k}(\omega) d\omega \qquad (2.56)$$

$$\sigma_{s_{ki}}^2 = \int_{-\infty}^{\infty} |H_i(i\omega)|^2 G_{\ddot{u}_k \ddot{u}_k}(\omega) d\omega \qquad (2.57)$$

Root mean squares, cross PSDs, and frequency transfer functions can be applied to estimate correlation coefficients.

$$\rho_{u_k u_l} = \frac{1}{\sigma_{u_k}\sigma_{u_l}} \int_{-\infty}^{\infty} G_{u_k u_l}(i\omega) d\omega \qquad (2.58)$$

$$\rho_{u_k s_{lj}} = \frac{1}{\sigma_{u_k}\sigma_{s_{lj}}} \int_{-\infty}^{\infty} H_j(-i\omega) G_{u_k \ddot{u}_l}(i\omega) d\omega \qquad (2.59)$$

$$\rho_{s_{ki} s_{lj}} = \frac{1}{\sigma_{s_{ki}}\sigma_{s_{lj}}} \int_{-\infty}^{\infty} H_i(i\omega) H_j(-i\omega) G_{\ddot{u}_k \ddot{u}_l}(i\omega) d\omega \qquad (2.60)$$

The correlation coefficients are limited within $[-1, 1]$, and describes how movement and acceleration at a support depend on acceleration and movement at other supports. A large correlation coefficient implies that movement and acceleration at support k and l are similar. Correspondingly, a correlation coefficient close to zero reveals that the two supports behave more or less independently. It is worth noting that only one natural frequency is excited at a time at each support. Implicitly, the correlation coefficients are dependant on which natural frequency numbers, i and j, that are excited at each support. The dependence of natural frequency number arise due to the matching mode shapes. Two mode shapes, corresponding

to two natural frequencies, may bring the motion at two supports in or out of phase.

After estimating correlation coefficients, a generic response of interest, $z(t)$, may be calculated. The generic response may be nodal displacements, internal forces, stresses or strains, depending on how the transfer function is set up. The expected value of the maximum response quantity is calculated by

$$
\begin{aligned}
E(max|z(t)|) = \Bigg(&\sum_{k=1}^{m} \sum_{l=1}^{m} a_k a_l \rho_{u_k u_l} u_{k,max} u_{l,max} \\
&+ 2 \sum_{k=1}^{m} \sum_{l=1}^{m} \sum_{j=1}^{n} a_k b_{lj} \rho_{u_k s_{lj}} u_{k,max} D_l(\omega_j, \xi_j) \\
&+ \sum_{k=1}^{m} \sum_{l=1}^{m} \sum_{j=1}^{n} \sum_{j=1}^{n} b_{ki} b_{lj} \rho_{s_{ki} s_{lj}} D_k(\omega_i, \xi_i) D_l(\omega_j, \xi_j) \Bigg)^{1/2}
\end{aligned}
\tag{2.61}
$$

2.2.6 MPRS from Eurocode 8, Part 2

EC8-2 (Annex D.3.4) contains guidelines for how to perform an MPRS analysis. The code suggests a simplified version of Der Kiureghian and Neuenhofer's method. The simplifications impose that (2.41)-(2.45) remain the same; however, the first order approximation of the PSDs differ. In EC8-2, PSDs are estimated by

$$
G_{uu}(\omega)_1 = \omega^{-2} \left(\frac{2\zeta\omega}{\pi} + \frac{4}{\pi\tau} \right) \left[\frac{D(\omega,\zeta)}{2.5} \right]^2, \omega \geq 0
\tag{2.62}
$$

$$
G_{\ddot{u}\ddot{u}}(\omega)_1 = \omega^{2} \left(\frac{2\zeta\omega}{\pi} + \frac{4}{\pi\tau} \right) \left[\frac{D(\omega,\zeta)}{2.5} \right]^2, \omega \geq 0
\tag{2.63}
$$

One may observe that the correction factor for low frequencies, $\frac{\omega^p}{\omega^p + \omega_f^p}$, has been discarded in (2.62) and (2.63). In addition, the peak factor for the oscillating response has been set to 2.5. This is in accordance with Der Khiureghian's recommendation of $p_s \geq 2$ (Der Kiureghian and Neuenhofer, 1992).

Furthermore, EC8-2 states one other simplification in the calculation of the maximum generic response.

$$
\begin{aligned}
E(max|z(t)|) = \Bigg(&\sum_{k=1}^{m} \sum_{l=1}^{m} a_k a_l \rho_{u_k u_l} u_{k,max} u_{l,max} \\
&+ \sum_{k=1}^{m} \sum_{l=1}^{m} \sum_{j=1}^{n} \sum_{j=1}^{n} b_{ki} b_{lj} \rho_{s_{ki} s_{lj}} D_k(\omega_i, \xi_i) D_l(\omega_j, \xi_j) \Bigg)^{1/2}
\end{aligned}
\tag{2.64}
$$

By comparing (2.61) to (2.64), one may observe that the triple sum has been omitted. EC8-2 (D.19) states that numerical analyses have proven the term to be insignificant and negligible. This is due to the fact that the correlation between acceleration and displacement is relatively small compared to correlation of two displacement histories or two acceleration histories.

Moreover, EC8-2 (Annex D.3.4(5)) claims that the site-response effect tends to dominate over the incoherence and the wave-passage effect. This legitimizes to neglect the cross-PSDs. Consequently, the equation for the estimated value of the maximum generic response becomes significantly simpler:

$$E(max|z(t)|) = \left(\sum_{k=1}^{m} a_k^2 u_{k,max}^2 \right.$$
$$\left. + \sum_{k=1}^{m} \sum_{i=1}^{n} \sum_{j=1}^{n} b_{ki} b_{kj} \rho_{s_{ki}s_{kj}} D_k(\omega_i, \xi_i) D_k(\omega_j, \xi_j) \right)^{1/2} \quad (2.65)$$

Chapter 3

Modelling in ANSYS

3.1 Choice of Finite Element Software and Learning Process

The main focus in this thesis, is the multi-point response spectrum method. Research has shown that there are one or few commercial finite element software that support this method. ANSYS mechanichal APDL (ANSYS inc., 2016) is one of them and was the software of choice. ANSYS also supports parametric design which means that both geometry and analysis configuration is written to a text file before being uploaded to the software. In this way, geometry can be transferred between two types of software. Because of the already existing model of the Chacao Bridge, this was a time saving feature.

The authors' experience with FE design originates from studies at NTNU and UC San Diego, where either ABAQUS (Dassault Systèmes, 2017) or OpenSees (McKenna et al., 2000) have been used. The thought process is more or less the same in all FE software using parametric design language; yet, the possibilities vary and the syntax is different. ANSYS is an enormous analysis software (27 GB) and has equally many possibilities. Due to lack of experience in ANSYS, both for the authors and co-workers, exploration of ANSYS' possibilities was necessary. ANSYS is able to solve a lot more than structural problems; hence, the user manual is long and intricate. Consequently, more than a month was spent on self-instruction; yet, it was a necessary process to ensure correct implementation.

In relation to this master's thesis, three structural models were made:

- A one storey shear frame

- A four-span beam bridge

- The Chacao bridge

In order to verify correct implementation in ANSYS, a one storey shear frame was modeled. At this level of simplicity, the model can be interpreted as a single-degree-of-freedom problem in hand calculations. Equal results from hand calculations and ANSYS imply that geometry and analyses was implemented correctly. However, results from the one storey shear frame were solely for verification and are not included in this thesis.

The more advanced four-span beam bridge is in this thesis referred to as *the Simple Bridge*, and is used to further increase knowledge of ANSYS and the software's possibilities for seismic analyses. This thesis focuses on comparing different methods for taking spatial variability into account. Consequently, the model of the Simple Bridge enhances the degree of certainty to whether a method over- or underestimates the response. Also, a simple model is likely to produce simple output such that complex effects may be avoided.

The model of the Chacao Bridge is the only model which was based on a real structure. Hence, it is the only model which produces realistic results. However, due to its level of complexity, the model's results may be disturbed by complex effects.

3.2   The Chacao Bridge

Modelling of the Chacao Bridge was carried out on the basis of an already constructed model in RM-Bridge by Aas-Jakobsen in Oslo. The entire structure, with exception of the South Approach Bridge, was designed linear-elastic. Aas-Jakobsen supplied the authors with structural reports and data sheets containing the information necessary to recreate the finite element model. To verify the implementation, a modal analysis was conducted. The computed natural frequencies from ANSYS and RM-bridge are listed in Table 3.1. In addition, the deviations listed in Table 3.1 compare ANSYS' frequencies with the frequencies obtained from RM-bridge. Results were considered more than satisfactory with a mean deviation of only 0.65% for the first 30 natural frequencies.

Table 3.1: Natural frequencies from RM-Bridge and ANSYS

Mode number	Frequency in RM-Bridge [Hz]	Frequency in ANSYS [Hz]	Deviation
1	0.061	0.061	0.00 %
2	0.074	0.074	0.00 %
3	0.093	0.096	3.23 %
4	0.118	0.120	1.69 %
5	0.125	0.124	-0.80 %
6	0.137	0.146	6.57 %
7	0.150	0.150	-0.66 %
8	0.151	0.152	1.33 %
9	0.173	0.173	0.00 %
10	0.182	0.184	1.10 %
11	0.201	0.202	0.50 %
12	0.231*	0.221*	0.45 %
13	0.220*	0.222*	-3.90 %
14	0.241	0.242	0.41 %
15	0.249	0.249	0.00 %
16	0.259	0.262	1.16 %
17	0.283	0.282	-0.35 %
18	0.288	0.290	0.69 %
19	0.289	0.292	1.04 %
20	0.294*	0.294*	0.00 %
21	0.292*	0.294*	0.68 %
22	0.298	0.299	0.34 %
23	0.309*	0.309*	0.00 %
24	0.309*	0.311*	0.65 %
25	0.309*	0.312*	0.97 %
26	0.315	0.317	0.63 %
27	0.348	0.351	0.86 %
28	0.349	0.354	1.43 %
29	0.356	0.358	0.56 %
30	0.369	0.372	0.81 %

[*] Natural frequencies having changed sequence relative to the RM-Bridge model

3.2.1   Description of the Finite Element Model

The Chacao Bridge model was constructed in six subsequent main steps:

1. Modeling of pylons with associated piles

2. Modeling of cables

3. Modeling of girder

4. Modeling of hangers

5. Applying boundary conditions and connecting structural components

6. Pre-tensioning of cables and hangers

All main components were modelled with BEAM188-elements and arbitrary cross sections. Beam188 is a two-node beam element based on Timoshenko Beam Theory, and includes effects from shear deformations (ANSYS inc., 2017c). The element is also suited for large-deformation theory, a property necessary to account for non-linear geometry during pre-tensioning of cables.

3.2.2   Structural Damping

Multiple mechanisms, such as friction and material hysteresis, will contribute to energy dissipation in the Chacao Bridge. Depending on whether an analysis was carried out in the frequency or time domain different methodologies were used to represent structural damping.

Spectrum analyses are based on mode superposition, thus structural damping was included through an equivalent damping ratio. ANSYS offers application of equivalent damping ratio at element level. Therefore, following EC8-2 and Chopra (2011)'s recommended damping ratio of 2% for welded steel and 5% for reinforced concrete, material dependent damping was defined for each element. Damping ratios used in the FE model of the Chacao bridge are listed in Table 3.2, where values for pre-tensioned cables and hangers were obtained from Aas-Jakobsen's design manual (Aas-Jakobsen et al., 2016b).

Table 3.2: Damping ratios for different structural components

Structural component	Damping ratio
Steel deck	2 %
Pylons and piers	5 %
Main cables	0.5 %
Hangers	2 %

In THA, damping was included by use of Rayleigh damping. Similar to equivalent damping ratio, ANSYS offers to apply Rayleigh damping at element level. Rayleigh damping combines mass- and stiffness-proportional damping, and is determined by (3.1) (Chopra, 2011). Low frequencies are dominated by mass proportional damping, while stiffness-proportional damping tend to be more important for higher frequencies (Priestley et al., 1996). a_0 and a_1 are Rayleigh constants, and $\mathbf{C}$, $\mathbf{M}$ and $\mathbf{K}$ are damping-, mass- and stiffness matrices.

$$\mathbf{C} = a_0 \mathbf{M} + a_1 \mathbf{K} \tag{3.1}$$

The procedure of finding Rayleigh constants is illustrated in Figure 3.1. First, a frequency interval ranging from natural frequency ω_i to ω_j was defined. Then, the Rayleigh constants were calculated such that the target damping ratio was achieved for natural frequency number i and j. All intermediate modes will be damped by a ratio equal to or lower than the target ratio, while modes outside the interval will be overdamped. Rayleigh constants used in the FE model of the Chacao bridge were calculated by use of the target ratios listed in Table 3.2. All calculations of Rayleigh constants were performed by Aas-Jakobsen et al. (2016b).

(a) Mass- and stiffness proportional damping

(b) Combined mass- and stiffness proportional damping
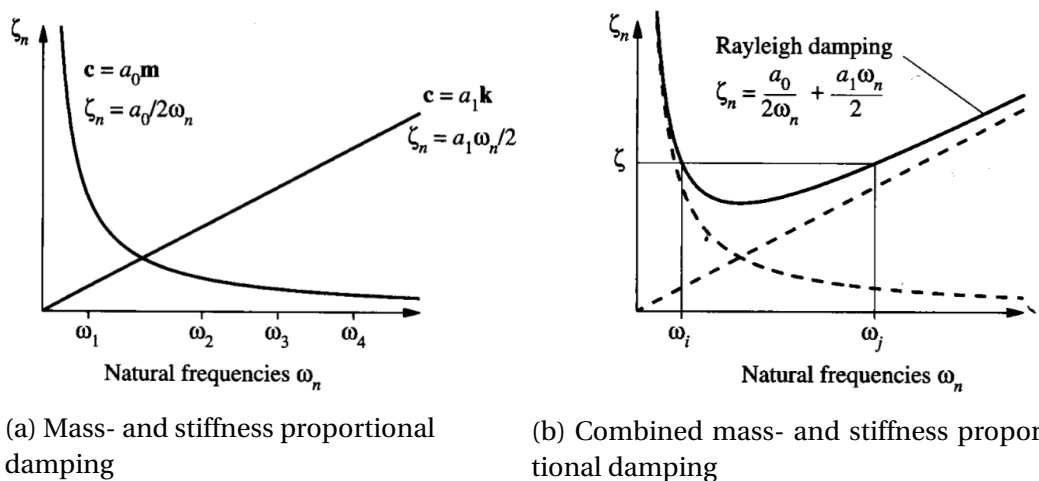
Figure 3.1: Illustration of Rayleigh damping (Chopra, 2011).

3.2.3   Pre-Tensioning of Cables and Hangers

Pre-tensioning of main cables and hangers is necessary to achieve correct geometry, capacity, and sufficient stiffness in the finite element models of suspension bridges. In reality, the cables are shorter prior to installation and stretched into position (Aas-Jakobsen et al., 2016b). Pre-tensioning was modeled by use of large-displacement theory and geometric non-linearity. Each element was subjected to a individually customized decrease in temperature, forcing the element to contract.

3.2.4   Soil-Structure Interaction

Soil conditions along the Chacao Bridge includes sedimentary rock layers above bedrock which will affect the behavior of the bridge (Aas-Jakobsen et al., 2016b). SYSTRA, a consultant company collaborating with Aas-Jakobsen, has conducted a soil-structure interaction (SSI) analysis in SASSI (Lysmer and Ostadan, 1981) and estimated foundation stiffness and damping. SSI was calculated for all supports, but due to simplifications in the finite element model, SSI was only included at the pylons. Furthermore, only soil stiffness was included in the conducted analyses. The absence of soil damping is expected to cause increased response for both RSAs and THAs.

Soil stiffness was modeled with use of MATRIX27-elements located in the transition between soil and foundation (ANSYS inc., 2017e). MATRIX27 is a massless element and represents the stiffness matrix developed in SASSI. The elements' location are illustrated in Figure 3.2 as yellow boundary conditions (BC).

(a) The South Pylon   (b) The Central Pylon   (c) The North Pylon
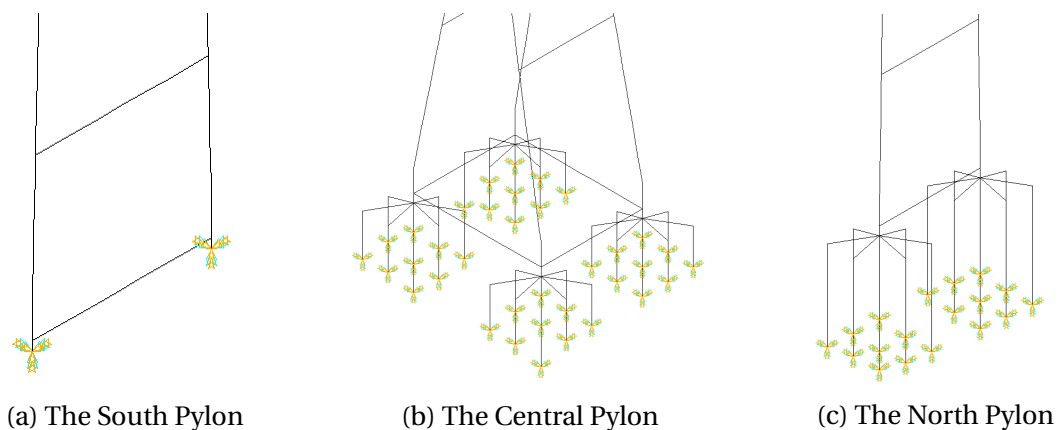
Figure 3.2: Location of SSI at the base of pylons

Dynamic foundation impedances are frequency dependent. Therefore, soil stiffness was chosen as the average of values corresponding to the most significant modes. The modal analysis showed that the most significant modes are within 0-1 Hz. Stiffness matrices were modeled identical for all interaction points associated with each pylon. The South Pylon is resting directly on the soil surface, and the massive stiff base plate forms a diagonal stiffness matrix (Aas-Jakobsen et al., 2016c). The Central Pylon and the North Pylon are supported by piles, and the softer support system gives rise to off-diagonal terms. As an example, the following matrix, conducted by SYSTRA, illustrates the stiffness matrix developed for the Central Pylon with units kN/m and kNm/rad.

$$
\mathbf{K}_{CentralPylon} = \begin{matrix} & \begin{matrix} x & \quad y & \quad z & \quad xx & \quad yy & \quad zz \end{matrix} \\ \begin{matrix} x \\ y \\ z \\ xx \\ yy \\ zz \end{matrix} & \begin{bmatrix} 14040 & 0 & 0 & 0 & 0 & -16940 \\ 0 & 25680 & 0 & 0 & 0 & 0 \\ 0 & 0 & 14035 & 16955 & 0 & 0 \\ 0 & 0 & 16955 & 60130 & 0 & 0 \\ 0 & 0 & 0 & 0 & 1488 & 0 \\ -16940 & 0 & 0 & 0 & 0 & 60230 \end{bmatrix} \end{matrix} \cdot 10^3
$$

3.2.5 Simplifications in the Finite Element Model

The most notable simplification in the structural model, compared to RM-bridge, is the absence of the South Approach Bridge Deck. The Deck was neglected due to advanced interaction between concrete and steel. In relation to the impact of spatial variability, the simplification was considered insignificant. See Figure 3.3 for illustration.

Furthermore, stress distributions in the fully constrained anchor blocks are not of relevance. Consequently, anchorages were represented by fixed supports, connecting the cables directly to the ground.

All elements were modelled with an arbitrary cross section. An arbitrary cross section is represented by a line, and does not account for cross sectional dimensions. This led to an

Figure 3.3: Finite element model of the Chacao Bridge in ANSYS

overlap of elements between crossbeams and pylon legs. Subsequently, the total length and mass of the crossbeams were increased. This was corrected by scaling the overall density for each pylon. The mass distribution deviates slightly from the RM-bridge model, but the total mass is correct. Scaling of the density was conducted for all structural components, except for the girder.

The girder was modeled with lumped mass and rotary inertia by use of single-node MASS21-elements. 2493.7 m is the total length of the girder and the mean length of the girder-elements is 9.6 m. This corresponds to a ratio of 0.004 between element length and total length. The ratio was considered as sufficiently small to justify the use of lumped masses. Compared to the rotary inertia about the longitudinal axis, the inertia about the vertical and transverse axes were considered insignificant and neglected. Figure 3.4 displays a section of the girder where MASS21-elements are illustrated by black dots.

Use of arbitrary cross sections may also result in geometric errors. In ANSYS, the girder elements appear as lines unable to account for the elements' physical extent. Therefore, the connections between girder and hangers were modeled as rigid links with master and slave nodes, see Figure 3.4. Rigid links were also used to connect the pylons to the main cable. In addition, horizontal rigid links were used as connection between the piles and the pylons to ensure that the piles act as a group.
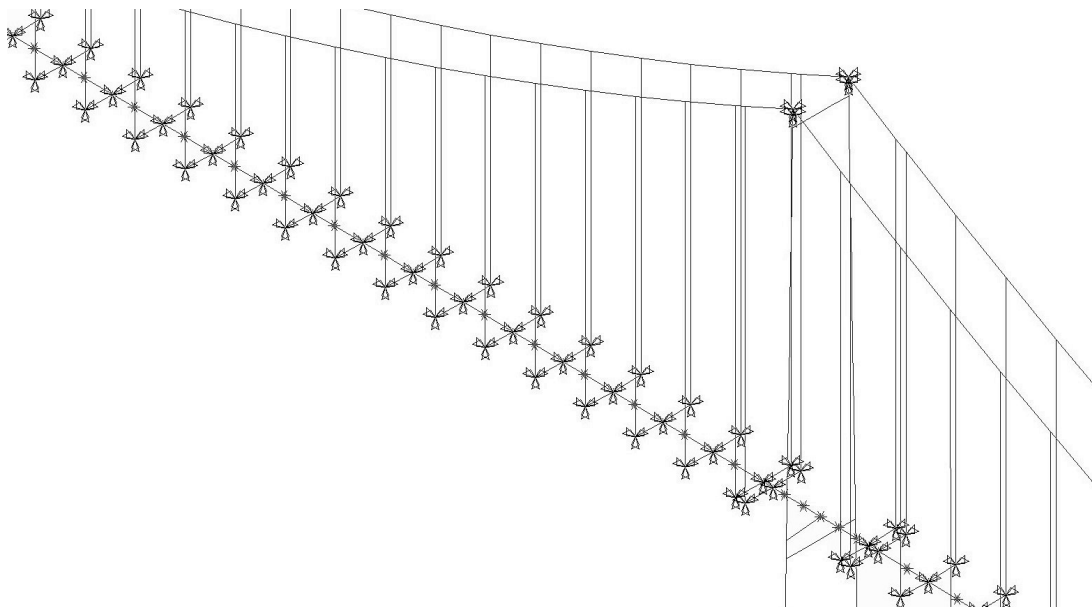
Figure 3.4: Lumped mass along the girder of the Chacao Bridge

3.3 The Simple Bridge

It was considered necessary to get familiar with the software by modelling a simple bridge, capable of running all analyses described in Chapter 2.2. Therefore, a four span beam bridge was chosen. In addition to the advantages discussed in the beginning of Chapter 3, the model was considered simple enough for manual implementation of Der Kiureghian and Neuenhofer's method. Due to limitation in time, the implementation of the method on the Chacao Bridge was not attempted.

3.3.1 Geometry and Boundary Conditions

The Simple Bridge is purely educational and consists of three single columns and four spans, as can be seen in Figure 3.5. Its design was chosen so it could represent a real bridge with realistic geometry. However, it does not follow all practical design conventions. For example, a real beam bridge is likely to have paired circular columns for better torsional resistance.

The columns were modelled as fixed at the lower ends. Furthermore, the bridge must be able to expand and contract longitudinally without creating restraint forces. Hence, the longitudinal DOF in the northern end of the girder remained unconstrained. For simplicity, the bridge was set to be 2-dimensional. Consequently, its movement is limited to translation in the longitudinal and vertical direction, in addition to rotation about the transverse axis.

Capacity of rectangular cross sections made from concrete is easily controlled by hand, thus, rectangular cross sections were chosen for columns and girder. Each span is 30 m and has a cross section of 10x0.5 m, while the columns are 10 m tall and have quadratic cross sections of 0.6x0.6 m.
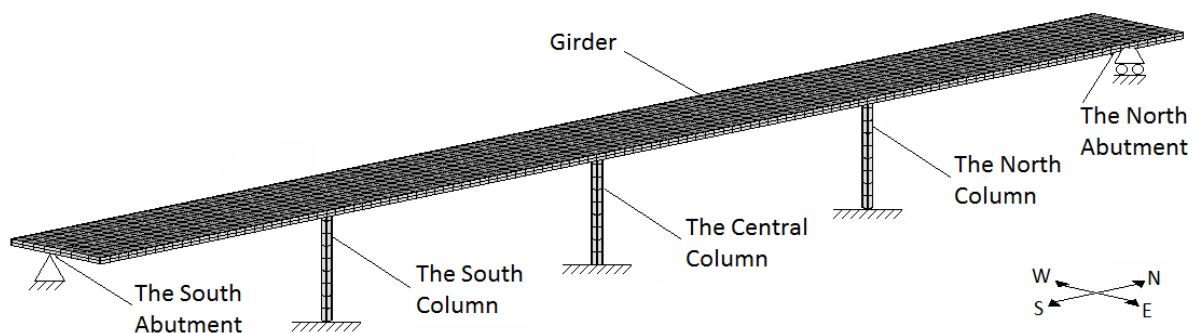
Figure 3.5: Geometry and boundary conditions for the Simple Bridge

The two-node beam element, BEAM188, was used for all components. A poorly refined mesh might result in inaccurate results; however, a finite element model with small elements is computationally expensive. Therefore, elements of length 1.0m were chosen and considered sufficiently accurate.

3.3.2   Loads and Verification

In order to verify the cross sections capacity, the bridge was loaded by self weight and a standardized traffic load (Standard Norge, 2003). The concrete's density was set to 25 kN/m^3 and the traffic load was estimated to be 2.8 kN/m^2, resulting in a total horizontally distributed load of 153 kN/m. For verification of the static analysis, an analytical estimation of the response was carried out according to Figure 3.6. It is worth noting that the estimated response neither accounts for the fixed connection between the columns and girder nor the moment in the columns.

Table 3.3 presents satisfactory similarities between the analytical and numerical response. Considering the simplifications in the analytical approach, the results were found to be comparable. The similarities are a confirmation of correct implementation of the finite element model.

The values from Table 3.3 were also used to assure realistic geometry and verify sufficient capacity by an M-N-diagram. Note that no reinforcement has been specified in the model of the Simple Bridge. Figure 3.7 presents the calculated M-N diagram and verifies that the geometry is realistic for $f_{ck} = 35 GPa$, $A_s F_{yk}/bh f_{ck} = 0.7$ and $d_2/h = 0.20$ (Øverli, 2016).
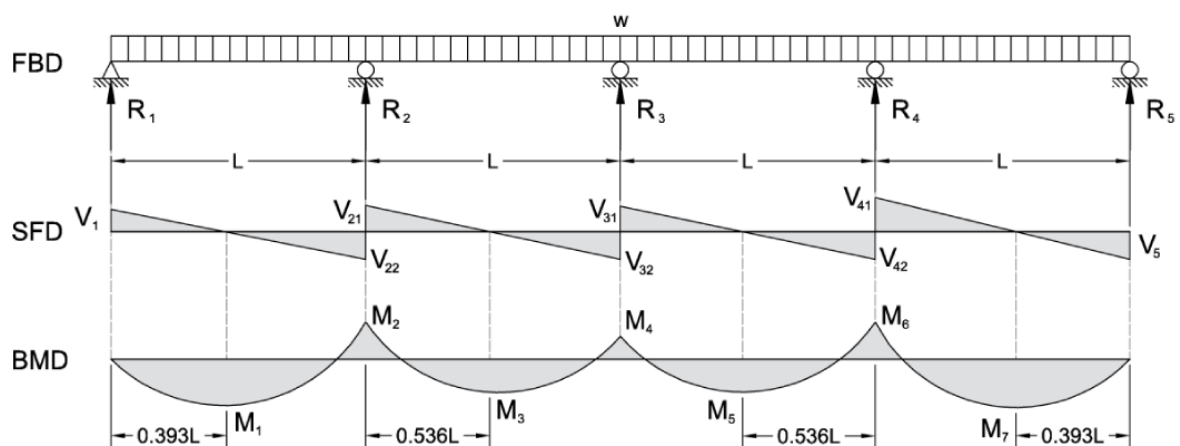
Figure 3.6: Shear and moment diagram for the Simple Bridge

Table 3.3: Comparison of analytical and numerical solution

Response	Analytical solution	ANSYS APDL	Ratio
R_1 [kN]	1804	1765	1.022
R_2 [kN]	5246	5149	1.019
R_3 [kN]	4260	4249	1.003
M_1 [kNm]	10630	10328	1.029
M_2 [kNm]	14748	14845	0.993
M_3 [kNm]	5012	5028	0.997
M_4 [kNm]	9832	9951	0.988
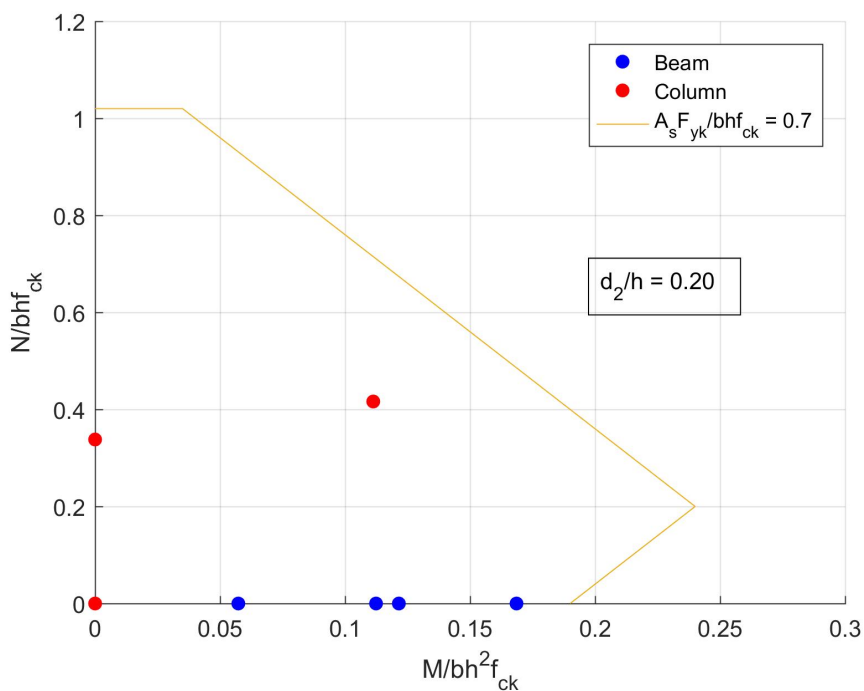
Figure 3.7: M-N diagram for the girder and columns based on Table 3.3

3.3.3 Structural Damping and Soil-Structure Interaction

Decisions were made such that the Simple Bridge would retain its simplicity; yet, the model must yield realistic response. Therefore, SSI was not included in the finite element model. However, a constant damping ratio was included in the RSAs following EC8-2's recommended value for reinforced concrete of 5% (EC8-2, 4.2.3(1)). In time domain, Rayleigh damping was estimated such that it would correspond to a damping ratio of 5%. Damping is further discussed in Chapter 4.3.2.

Chapter 4

Implementation of Analyses

In line with EC8-2, analyses in both time and frequency domain have been conducted. Table 4.1 presents an overview of which analyses that has been conducted on the two finite element models.

Table 4.1: Overview of conducted analyses

Domain	Analysis	The Chacao Bridge	The Simple Bridge
Time domain	THA	x	x
Frequency domain	MPRS	x	x
	Simplified	x	x
	SPRS	x	x
	Der K. & N.		x
	EC8-2's version of Der K. & N.		x

4.1 Response Spectra and Time Histories

The time histories and equivalent response spectra provided by Aas-Jakobsen, represent a maximum probable earthquake-event with a return period of 1030 years (Aas-Jakobsen et al., 2016e). According to Aas-Jakobsen et al. (2016d), the dominating seismic event at the Chacao Channel is caused by subduction between the Nazca- and the South American Plate. The subduction zone is located 80km-150km from the planned location of the Chacao Bridge and is expected to cause earthquakes with moment magnitudes ranging 7.5-8.5.

In order to preserve both seismic and local characteristics, Aas-Jakobsen et al. (2016e) used a total of seven sets of accelerograms to create the seismic input for the Chacao Bridge.

39

More specific, the accelerograms were taken from the seismic databank of the University of Chile, and originate from seismic events that occurred in Maule and Valparaiso.

Due to challenging geotechnical site conditions, few accelerograms matched the conditions at the location of the Chacao Bridge. All seven sets of accelerograms was scaled such that their corresponding response spectra matched the site-specific target spectra for rock motion (Aas-Jakobsen et al., 2016e). In order to minimize the distance to the target spectrum, a convergence criterion of 5% at all frequencies was set. The geometric mean of all seven horizontal response spectra is depicted in Figure 4.1. A similar match was obtained in all principal directions; hence, a good representation of the target spectra was achieved in terms of the mean spectra.

In order to represent free-field surface motion, accelerograms were adjusted for local soil conditions at all seven support locations (Aas-Jakobsen et al., 2016a). A total of seven sets of site-specific accelerograms were calculated for each location.

In addition, Aas-Jakobsen et al. (2016a) estimated equivalent response spectra for all support locations in all three directional components. Each response spectrum was calculated as the mean of seven response spectra, corresponding to the seven site-specific time histories in the direction of interest. To account for varying damping, spectra were calculated with 0, 1, 2, 4, 5, 6, 10 and 20% damping ratio.

As stated above, time histories and response spectra were adjusted for local soil conditions. Hence, the site-response effect described in Chapter 2.1 is accounted for through use
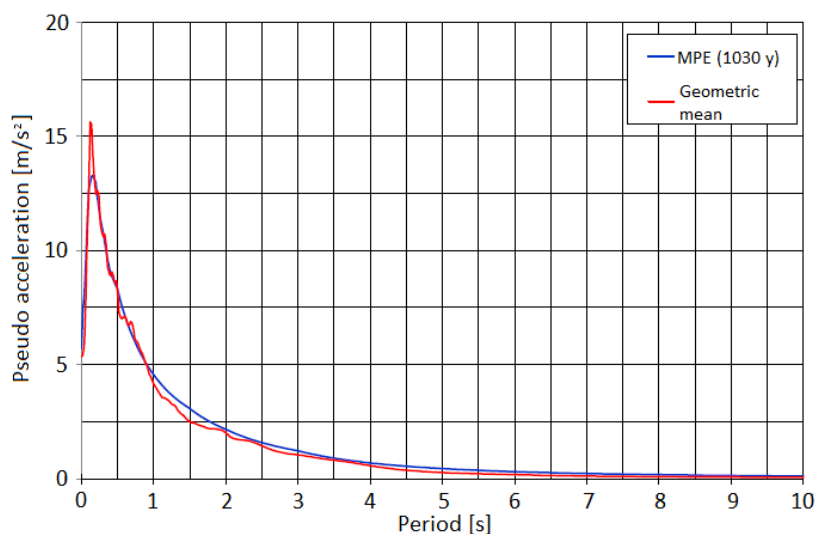

Figure 4.1: Horizontal target and mean spectrum at bedrock (Aas-Jakobsen et al., 2016e).

Table 4.2: Naming convention for filenames used in the analyses

Location (The Chacao Bridge)	Direction	Filename THA	Filename SPRS	Filename MPRS
The South Anchor Block	Longitudinal	THA_SAn_L_XX	SPRS_SAn_L_YY	MPRS_SAn_L_YY
	Transverse	THA_SAn_T_XX	SPRS_SAn_T_YY	MPRS_SAn_T_YY
	Vertical	THA_SAn_V_XX	SPRS_SAn_V_YY	MPRS_SAn_V_YY
The South Pylon	Longitudinal	THA_SP_L_XX	SPRS_SP_L_YY	MPRS_SP_L_YY
	Transverse	THA_SP_T_XX	SPRS_SP_T_YY	MPRS_SP_T_YY
	Vertical	THA_SP_V_XX	SPRS_SP_V_YY	MPRS_SP_V_YY
The Central Pylon	Longitudinal	THA_CP_L_XX	SPRS_CP_L_YY	MPRS_CP_L_YY
	Transverse	THA_CP_T_XX	SPRS_CP_T_YY	MPRS_CP_T_YY
	Vertical	THA_CP_V_XX	SPRS_CP_V_YY	MPRS_CP_V_YY
The North Pylon	Longitudinal	THA_NP_L_XX	SPRS_NP_L_YY	MPRS_NP_L_YY
	Transverse	THA_NP_T_XX	SPRS_NP_T_YY	MPRS_NP_T_YY
	Vertical	THA_NP_V_XX	SPRS_NP_V_YY	MPRS_NP_V_YY
The North Abutment	Longitudinal	THA_NAb_L_XX	SPRS_NAb_L_YY	MPRS_NAb_L_YY
	Transverse	THA_NAb_T_XX	SPRS_NAb_T_YY	MPRS_NAb_T_YY
	Vertical	THA_NAb_V_XX	SPRS_NAb_V_YY	MPRS_NAb_V_YY
The North Anchor Block	Longitudinal	THA_NAn_L_XX	SPRS_NAn_L_YY	MPRS_NAn_L_YY
	Transverse	THA_NAn_T_XX	SPRS_NAn_T_YY	MPRS_NAn_T_YY
	Vertical	THA_NAn_V_XX	SPRS_NAn_V_YY	MPRS_NAn_V_YY

XX: Earthquake number (1-7)
YY: Damping ratio (0, 1, 2, 4, 5, 6, 10, 20 %)

of the provided seismic input motions. Time histories and response spectra do not account for the incoherence effect, the wave-passage effect or the attenuation effect.

A complete list of the time histories and response spectra used in this thesis is listed in Table 4.2. Note that the name convention is used in Chapter 4.3 in order to refer to which seismic action that was adapted from the Chacao Bridge to the Simple Bridge.

4.2 Implementation of Analyses for the Chacao Bridge

Earthquakes are triggered in the ground; therefore, all supports in contact with the ground will be excited by the earthquake's motion. Figure 4.2 names the components which are being excited. However, the Chacao Bridge spans over varying soil conditions. This made it necessary to adjust the earthquake motion to match the local soil conditions, see Chapter 2.1.3. Consequently, it was used different seismic input at the six named components in Figure 4.2. The Central Pylon and the North Pylon rest on multiple piles. Therefore, in
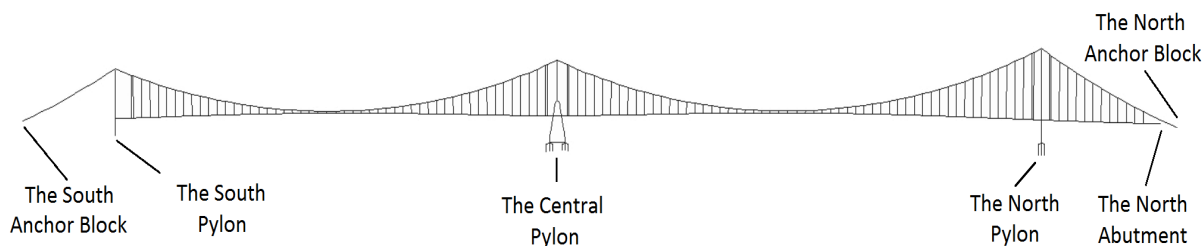
Figure 4.2: Locations of input on the Chacao Bridge

all analyses conducted, the same seismic input was used for all piles at one location. Even though the methods investigated in this paper are based on different theory, the procedure described in this paragraph applied to all of them.

Seismic analyses accounts for spatial variability differently, and may include the effects of local soil conditions, incoherency and wave-passage. Due to lack of information regarding wave velocities, incidence angle of arrival etc., only the effect of local soil conditions was included in the conducted THAs and RSAs. However, this is justified in EC8-2, which claims that the site-response effect tends to dominate the other two phenomena (EC8-2, D.3.4.3). The THAs were conducted with site-specific acceleration histories, while the RSAs were conducted with site-specific response spectra. The simplified method does not account for spatial variability in terms of the three phenomena. Conversely, spatial variability was accounted for by pseudo-static displacements estimated by local soil factors and span widths.

4.2.1   Seismic Input Motions

Large scale earthquakes will form permanent soil displacements and introduce additional static forces. The time histories provided by Aas-Jakobsen et al. (2016a) already account for the effects of permanent displacements. However, RSAs do not account for permanent displacements directly, and static effects must be added separately. Therefore, an additional static analysis with permanent displacements was carried out. The results from permanent displacements were added to the results from SPRS and MPRS.

Similar to Aas-Jakobsen et al. (2016b), maximum permanent displacements were assumed to occur at the end of each displacement history. Due to seven sets of displacement histories for each support location, design values were calculated as the mean of final
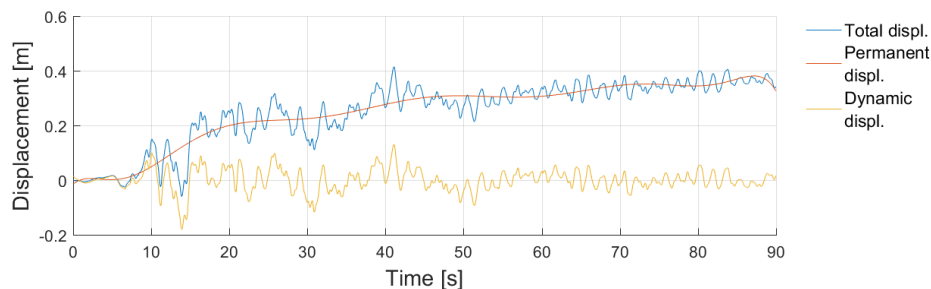
Figure 4.3: Displacement history with and without permanent displacements

displacements in each directional component. To illustrate the quantity of permanent displacements in each time history, Figure 4.3 depict a longitudinal displacement history for the South Pylon.

4.2.2 Time History Analysis

Time history analyses are computationally expensive and require multiple analyses. Yet, they are considered to provide accurate results due to their deterministic approach. Two identical earthquakes will never occur; therefore, multiple THAs must be performed in order to get a statistical average of the structure's response. EC8-2 states that the mean of seven pairs of horizontal ground motions is sufficient to estimate the maximum response (EC8-2, 4.2.4.3(1)).

As described in Chapter 4.1, each seismic event is represented by six three-component accelerograms. ANSYS allows structural systems to be excited by multiple accelerograms simultaneously, including varying directions. In line with EC8-2, seven seismic events have been simulated, and an equivalent number of THAs have been conducted.

In ANSYS, the full transient analysis method was used. The full method is based on a modified version of the equation of motion corresponding to Newmark's method, see (2.31). Furthermore, ANSYS includes a numerical dissipation algorithm in the integration parameters. Consequently, δ and α were set to 0.5050 and 0.2525. The values correspond to an amplitude decay factor of 0.0050.

Accelerograms provided by Aas-Jakobsen were generated with a time step of 0.01 seconds and a duration equal to 90 seconds. The size and weight of the Chacao Bridge give rise to large natural periods, such that long-lasting accelerograms are necessary to capture the effects of low natural frequencies. Moreover, to account for the Bridge's large natural fre-

quencies, a small time step is required. The given values for time step and duration were believed to provide sufficient accuracy.

4.2.3   Single-Point Response Spectrum Analysis

All SPRS analyses were performed with a total of 1500 modes. Figure 4.4 shows how the cumulative effective modal mass varies with increasing number of modes. 90% of the effective modal mass is included in all translational and rotational directions by use of 1064 modes. However, similar to Aas-Jakobsen et al. (2016b), 1500 modes was used, and a minimum 98% of the effective modal mass was included in all directions.

By use of the criterion in (2.34), modes were considered closely spaced. Hence, modal contributions had to be combined by use of the CQC-rule. The CQC-rule requires a defined modal damping ratio for all modes included in the analysis. Therefore, mode dependent damping ratios were calculated by (4.1) during the modal analysis, with the material dependent damping ratios defined in Table 3.2 as input.

$$\xi_i = \frac{\sum_{k=1}^{N_m} \xi_k E_{k,i}}{\sum_{k=1}^{N_m} E_{k,i}} \tag{4.1}$$

Equation (4.1) is based on the ratio of strain energy in each material in each mode (ANSYS inc., 2017a). N_m is the number of materials, ξ_k is the damping ratio for material number k, and $E_{k,i}$ is the strain energy produced in material k in mode i.

All spectra were created with an equivalent damping ratio, and do not account for the mode dependent damping ratios. This was solved by interpolation of spectra with different equivalent damping ratio. Consequently, new spectra where all 1500 modes are assigned their actual damping ratio from (4.1) were created.

Unfortunately, an SPRS analysis in ANSYS only allows 100 values to be defined in a set of input response spectra. Therefore, the amount of spectral values were reduced by the recursive Douglas-Peucker polyline simplification method (Douglas and Peuker, 2011). However, removing a minimum of 1400 points does not leave a perfect match.

Figure 4.5 illustrates that 100 points are incapable of providing the same information as 1500 points. The input spectral acceleration will be changed; therefore, an error may occur in the response of the Bridge. Depending on the frequency, Figure 4.5 suggests that both

under- and overestimation of the spectral acceleration occur.

ANSYS allows three principle directions to be excited in one analysis; yet, the limit of 100 values still applies. In order to preserve the most information from each response spectrum, the SPRS analyses were limited to one principle direction. 18 SPRS analyses have been conducted, one for each support, in all three principle directions.

Equivalent to Aas-Jakobsen et al. (2016b), it was assumed that the responses from site-specific spectra are uncorrelated. Hence, results for the South Pylon were calculated with the spectrum for the South Pylon as input, results for the Central Pylon were calculated with the spectrum for the Central Pylon as input, and so on. The exception was components spanning several locations, such as the girder. Results for these components were obtained from an envelope of SPRS analyses conducted for the South Pylon, the Central Pylon, the North Pylon and the North Abutment. In addition, the response from excitation in different principle directions were combined using the SRSS-rule.

After performing the SPRS analyses, it was noted that the use of Douglas-Peucker polyline simplification on the response spectra for the North Pylon led to a significantly increased response. For that reason, the spectra for the North Pylon was replaced by the spectra from the North Abutment. Both set of spectra are similar in magnitude and shape, and were expected to produce similar effects.
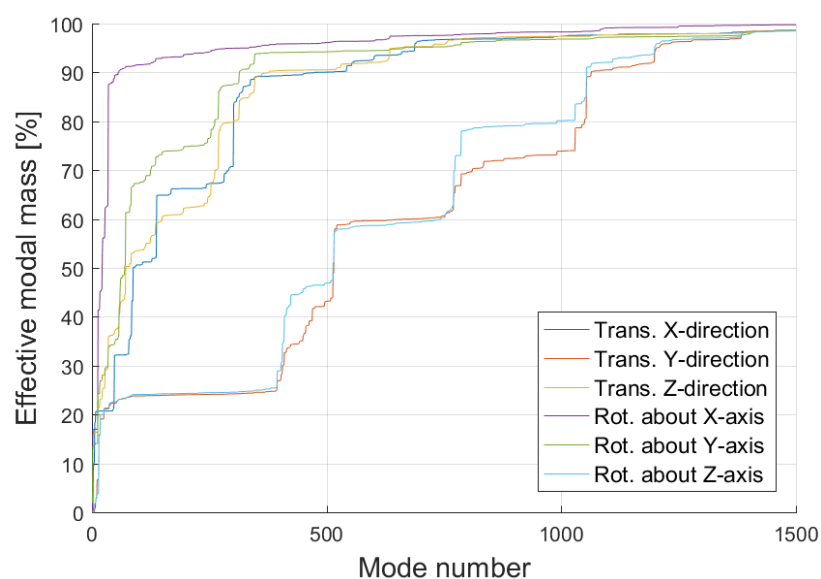

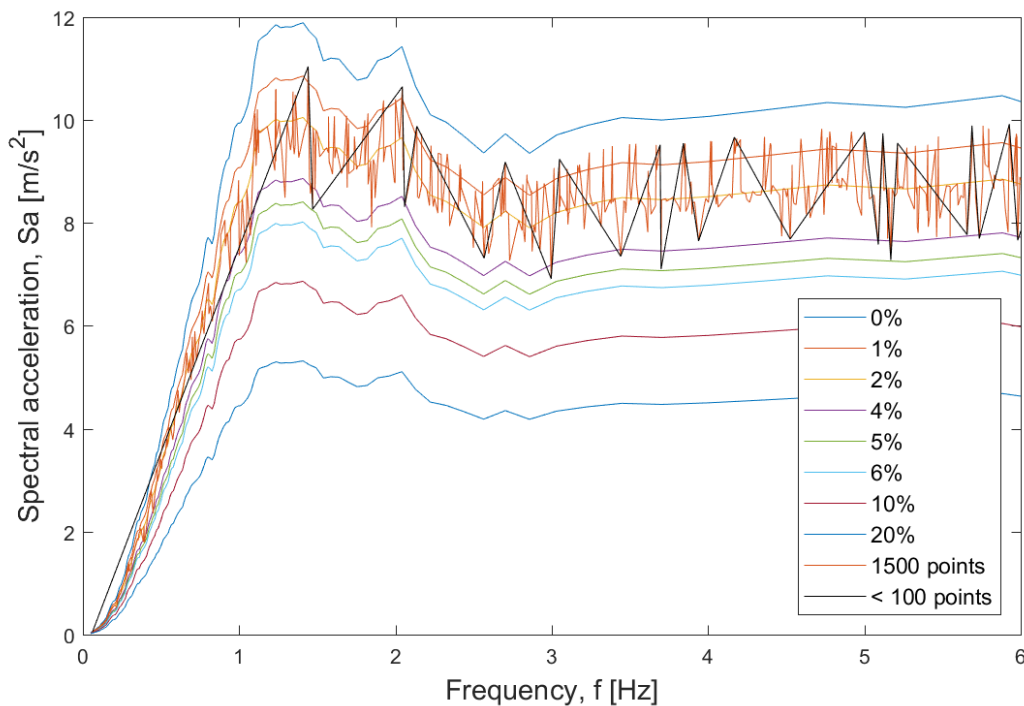Figure 4.4: Cumulative effective modal mass for the Chacao Bridge

Figure 4.5: Low frequencies of the transverse response spectra for the Central Pylon

4.2.4 Multi-Point Response Spectrum Analysis

In contrast to SPRS analyses, MPRS analyses do not excite all fixed boundary conditions by each response spectrum. ANSYS enables the user to choose which nodes to be excited, and in what principle direction (ANSYS inc., 2017b). In addition, ANSYS has no restriction for the maximum number of values in a response spectrum. All 1500 modes were assigned the exact modal damping ratio calculated with (4.1). As in SPRS analyses, modal response was combined using the CQC-rule, and response from different spectra were combined using the SRSS-rule.

The main difference between the MPRS and the SPRS method, is that all spectra are defined in a single analysis. The nodes for the South Pylon were excited by spectra for the South Pylon, nodes for the North Pylon were excited by spectra for the North Pylon, and so on. Subsequently, the number of spectrum analyses was reduced from 18 to 1. When running the analysis, ANSYS activates one spectrum at a time, and saves the response. The MPRS-function combines the response from each spectrum by use of the SRSS-rule. The function also assumes all spectra to be uncorrelated, meaning that excitation from one spectrum is not affected by excitation from other spectra (ANSYS inc., 2017b).

4.2.5 The Simplified Method

Due to varying spans and tower design, the Chacao Bridge is asymmetrical about its transverse axis. The simplified method requires a bridge end to be chosen as a reference point; therefore, two cases were evaluated. The South Abutment is the reference support of case 1, while the North Abutment is the reference support of case 2. Displacement shapes from the two cases are illustrated in Figure 4.6. Note that the South Abutment was not included in the model; yet, horizontal displacements were calculated as if it was present. In addition, Set B is based on the intermediate distances of supports, making Set B identical for both cases.

The simplified method require use of elastic response spectra defined by EC8-1; however, no geotechnical reports were available for the location of the Chacao Bridge. Consequently, site-specific spectra provided by Aas-Jakobsen et al. (2016a) were used. Choice of spectra was based on the magnitude of spectral acceleration and equivalent damping ratio. During calculation of modal damping ratios, it was observed that the first 1500 modes were dominated by a damping ratio about 2%. Thus, spectra for the South Pylon were chosen based on their large spectral magnitude for 2% equivalent damping ratio.

(a) Case 1, Set A

(b) Case 1, Set B
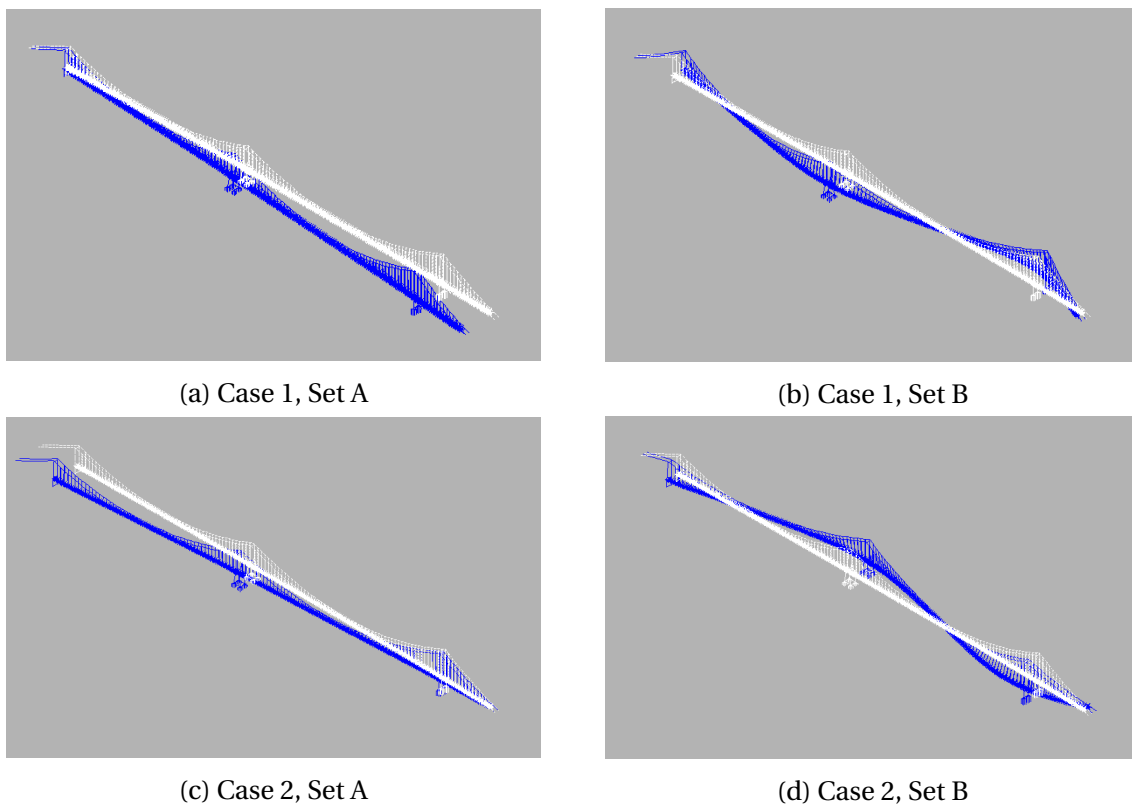
(c) Case 2, Set A

(d) Case 2, Set B

Figure 4.6: Horizontal displacement sets used in the simplified method

The inertia response was calculated using three-component response spectra. As for the SPRS analyses, modal contributions were combined using the CQC-rule, and response from each principle direction was combined using the SRSS-rule. Furthermore, response from pseudo-static displacements were obtained as the envelope of both sets and cases. The inertia and pseudo-static solution were combined by the SRSS-rule.

In estimation of pseudo-static displacements, the design ground displacement was calculated such that it represented the site-specific spectra for the South Pylon. The procedure is described by (4.2)-(4.5). Furthermore, by guidance from professor Amir M. Kaynia, local ground conditions were assumed to correspond to ground type C below all supports. The general expression for horizontal elastic response spectrum, valid for periods in the domain $T_D \leq T \leq 4s$, is given by

$$S_a(T) = a_g \cdot S \cdot \eta \cdot 2.5 \cdot \left[\frac{T_C T_D}{T^2} \right] \tag{4.2}$$

where η is a correction factor for damping, $(a_g \cdot S)$ is the peak ground acceleration (PGA), T is the period of the structure, and T_C and T_D are limit-values in the spectrum (EC8-1, 3.2.2.2). The correction factor was neglected and the relationship between the acceleration and displacement response spectrum was utilized:

$$S_d(T) = \frac{T^2}{4\pi^2} \cdot S_a(T) \tag{4.3}$$

$S_a(T)$ and $S_d(T)$ correspond to spectral acceleration and displacement. Constant spectral displacement was achieved by combination of (4.2) and (4.3):

$$S_d(T) \approx 0.0633 \cdot a_g \cdot S \cdot T_C T_D \quad T_D \leq T \leq 4s \tag{4.4}$$

Figure 4.7 illustrates the displacement response spectrum for the South Pylon estimated by (4.3). The constant spectral displacement in (4.4) is equivalent to the PGD in Figure 4.7, and equal to $S_d(T) = 0.3224$. Equation (2.23), which expresses the design ground displacement, was simplified to:

$$d_g = \frac{0.025}{0.0633} \cdot S_{e,d}(T) \approx 0.1273m \tag{4.5}$$

The design ground displacement is required for estimation of displacement set A and B. Design values for both sets and cases are listed in Table 4.3.

Table 4.3: Displacements used in the simplified method

| Case 1	The South Abutment	The South Pylon	The Central Pylon	The North Pylon	The North Abutment
Support index i	0	1	2	3	4
L_i [m]	0	140	1195	2350	2634
$L_{\alpha v,i}$ [m]	140	597.5	1105	719.5	284
d_i, Set A [m]	0	0.0630	0.1800	0.1800	0.1800
d_i, Set B [m]	0.0157	-0.0672	0.1243	-0.0809	0.0319
Case 2	The North Abutment	The North Pylon	The Central Pylon	The South Pylon	The South Abutment
Support index i	0	1	2	3	4
L_i [m]	0	284	1439	2494	2634
$L_{\alpha v,i}$ [m]	284	719.5	1105	597.5	140
d_i, Set A [m]	0	0.1278	0.1800	0.1800	0.1800
d_i, Set B [m]	-0.0319	0.0809	-0.1243	0.0672	-0.0157
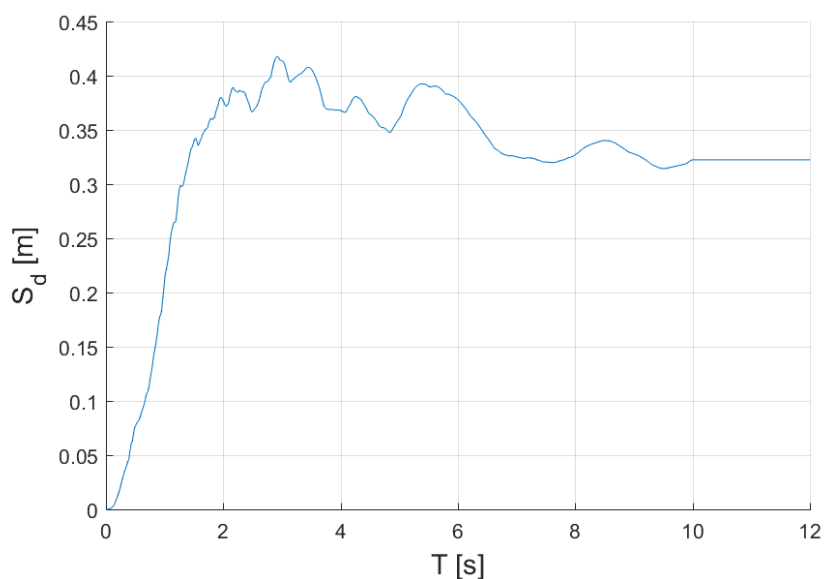
Figure 4.7: Transverse displacement response spectrum for the South Pylon

4.3   Implementation of Analyses for the Simple Bridge

As listed in Table 4.1, two versions of Der Kiureghian and Neuenhofer's method were conducted on the Simple Bridge in addition to THA, SPRS, MPRS and the simplified method. Compared to the Chacao Bridge, the analyses were implemented in the same manner or simpler. Subsequently, there is a significant difference in terms of excitation. The Chacao Bridge was excited by 3-dimensional seismic loads, while the Simple Bridge was restricted to longitudinal excitation. All transverse movement was restrained, resulting in a 2-dimensional load distribution. Longitudinal excitation was implemented in order to avoid complex 3-dimensional effects. Furthermore, Der Kiuereghian and Neuenhofer's method became simpler to implement.

Spatial variability was accounted for in the same manner as for the Chacao Bridge. The exception is Der Kiuereghian and Neuenhofer's method, which also accounted for the incoherence and wave-passage effect.

4.3.1   Seismic Input Motions

The seismic actions were adopted from the analyses conducted on the Chacao Bridge. However, the accelerograms and permanent displacements were created in relation to the size of the Chacao Bridge. Using the same seismic input on a bridge 1/20th of the length induced too dominating static forces. For that reason, new THAs and RSAs were conducted with absence of permanent displacements.

Effects from permanent displacements were removed using the digital Butterworth high-pass filter. A high-pass Butterworth filter attenuates signals below a customized "cutoff" frequency, while signals above the frequency remain intact (MathWorks, 2017b). To illustrate the effect of high-pass filters, Figure 4.8 depicts two longitudinal displacement histories for the North Abutment. In addition, equivalent acceleration histories are illustrated in Figure 4.9. The blue line in Figure 4.8 represents the displacement history for the Chacao Bridge, while the red line represents the filtered displacement history for the Simple Bridge. The difference of the two lines are supposedly the permanent displacements and is represented by the yellow line.
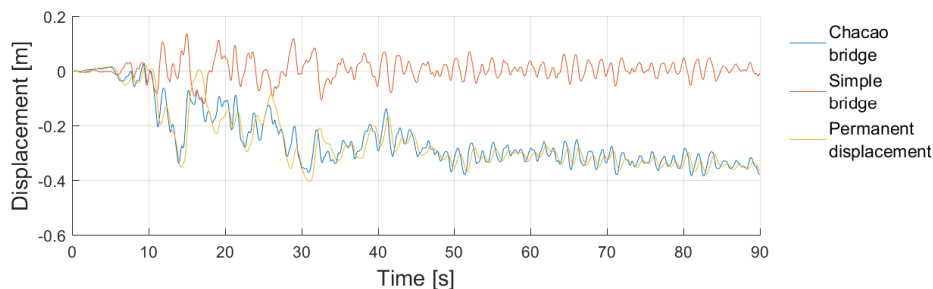
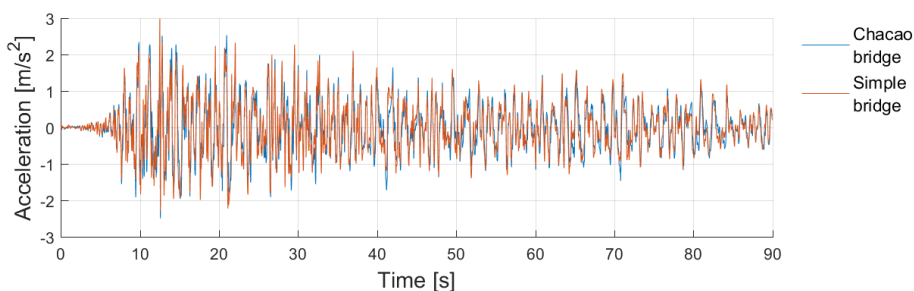Figure 4.8: Displacement histories for the North Abutment

Figure 4.9: Acceleration histories for the North Abutment

The permanent displacements in Figure 4.8 can be represented by low frequency signals. This applies to all the displacement histories. Therefore, a 6th-order high-pass Butterworth filter was used to remove permanent displacements from the time histories. The cutoff frequency was set to 0.10 Hz, which, for a Nyquist frequency of 50 Hz, corresponds to 0.002π rad/sample (MathWorks, 2017a).

4.3.2 Structural Damping

As for the Chacao Bridge, a modal analysis was carried out in order to estimate effective modal masses. Figure 4.10 illustrates the cumulative effective modal mass for the Simple Bridge. The requirement in EC8-2 (4.2.1.2(2)) of 90% effective mass is reached within the first 30 modes.

In addition, EC8-2 (4.2.3(1)) recommends 5% equivalent damping ratio for reinforced concrete. The recommended value was used in RSAs; however, equivalent damping ratio cannot be defined in time domain. Therefore, Rayleigh damping was used for THAs.

Rayleigh damping is defined by the frequency interval bounded by ω_i and ω_j in Figure 3.1. Intermediate frequencies are underdamped, while frequencies larger than ω_j are overdamped. It was observed that an interval including the 30 first modes would signifi-

cantly underdamp the response. Therefore, by Figure 4.10 it was determined that the first 13 modes were of most significance. Hence, ω_i and ω_j were set to 1 and 13 in order to make Rayleigh damping comparable to 5% equivalent damping ratio. As a result, Rayleigh constants $a_0 = 0.583$ and $a_1 = 0.0014$ were obtained.
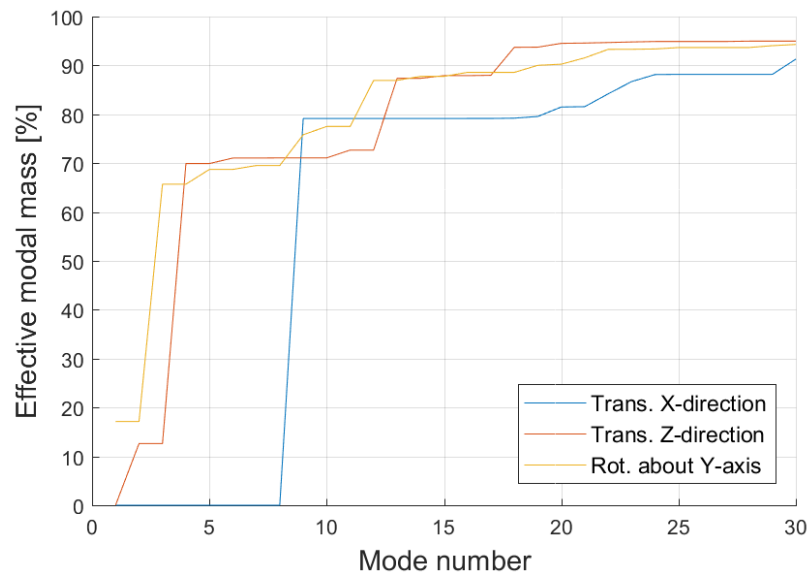

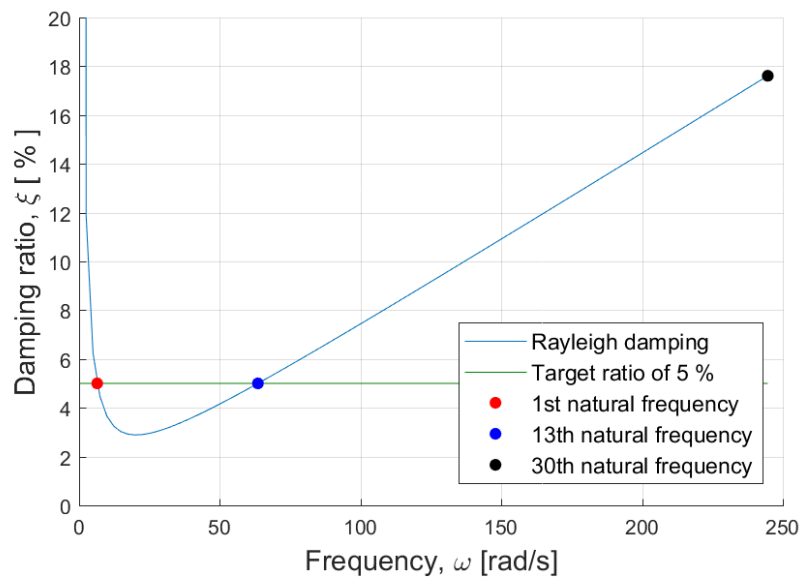Figure 4.10: Cumulative effective modal mass for the Simple Bridge

Figure 4.11: Rayleigh damping for the Simple Bridge

4.3.3 Time History Analysis

The Simple Bridge is purely educational; therefore, no customized accelerograms exist. As an alternative, accelerograms customized for the supports of the Chacao Bridge were reused. Accelerograms and locations of excitation are listed in Table 4.4. Furthermore, the implementation of THA on the Simple Bridge was the same as for the Chacao Bridge: Newmark's method with $\alpha = 0.2525$ and $\delta = 0.5050$ were used, and nonlinear geometry was included.

Table 4.4: Reuse of accelerograms created for the Chacao Bridge at the Simple Bridge

Support at the Simple Bridge	Input motion THA
The South Abutment	THA_SAn_L_XX
The South Column	THA_SP_L_XX
The Central Column	THA_CP_L_XX
The North Column	THA_NP_L_XX

4.3.4 Single-Point Response Spectrum Analysis

Similar to THA, the SPRS analyses were implemented with spectra customized for the Chacao Bridge. Table 4.5 lists which response spectra that were used at different locations. However, in contrast to the Chacao Bridge, all modes were assigned 5% equivalent damping ratio, and spectra with 5% constant damping ratio were used.

Table 4.5: Reuse of SPRS-spectra created for the Chacao Bridge at the Simple Bridge

Support at the Simple Bridge	Input motion SPRS
The South Abutment	SPRS_SAn_L_5%
The South Column	SPRS_SP_L_5%
The Central Column	SPRS_CP_L_5%
The North Column	SPRS_NP_L_5%

Spectra calculated with 5% constant damping ratio consist of 502 values. Compared to spectra with variational damping, they appear a lot smoother. The reduction to the necessary 100 points in the SPRS analysis was far more accurate than for the Chacao Bridge. Figure 4.12 illustrates that almost no information was lost by use of the recursive Douglas-Peucker polyline simplification method.

As indicated in Chapter 4.2.3, it is favorable to run one SPRS analysis for each spectrum in each principal direction. Since there were four different response spectra involved, four
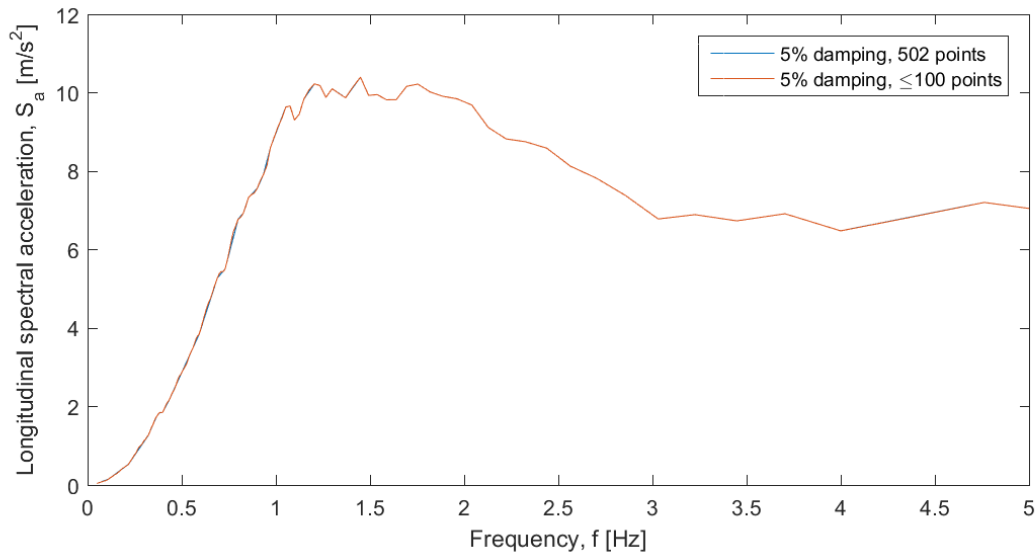
Figure 4.12: Comparison of response spectra before and after Douglas-Peuker simplification

SPRS analyses were conducted. These spectra were assumed uncorrelated. Furthermore, in order to fulfill EC8-2's requirement for 90% effective modal mass, a total of 30 modes were included in all SPRS analyses.

As for the Chacao Bridge, EC8-2 (4.2.1.3(2)) was used to choose mode combination method. At least one pair of modes satisfied the conditions in (2.34); therefore, CQC was used in the analyses.

Even though the implementation of SPRS analyses were similar to the ones conducted on the Chacao Bridge, the results were treated differently. Due to far shorter bridge spans, one can no longer assume that the response in one component is dominated by the closest spectrum. Therefore, a component's response was set to be the maximum response from any of the four SPRS analyses.

4.3.5   Multi-Point Response Spectrum Analysis

The MPRS analysis is generally similar to the SPRS analysis. However, the ability to excite the structure by different response spectra simultaneously reduced the number of required analyses from four to one. Equivalent to the SPRS analyses, the model solutions were combined by the CQC-rule. Furthermore, the solution from each spectrum was combined by the SRSS-rule, as described in Chapter 4.2.4. Table 4.6 lists which response spectra that were used at different locations.

Table 4.6: Reuse of MPRS-spectra created for the Chacao Bridge at the Simple Bridge

Support at the Simple Bridge	Input motion MPRS
The South Abutment	MPRS_SAn_L_5%
The South Column	MPRS_SP_L_5%
The Central Column	MPRS_CP_L_5%
The North Column	MPRS_NP_L_5%

4.3.6 The Simplified Method

The simplified method is based on the response from pseudo-static displacements and an RSA. Similar to the implementation on the Chacao Bridge, a spectrum for the South Pylon was used in the spectrum analysis. The pseudo-static displacements were obtained in the same manner as in Chapter 4.2.5. However, in order to include transverse pseudo-static displacements, the transverse constraints described in Chapter 3.3.1 were removed.

Even though the simplified method is intended for 3-dimensional models, it was carried out according to EC8-2 (3.3). Using the value in (4.5) as the design ground displacement, the resulting pseudo-static displacements listed in Table 4.7 were obtained.

Table 4.7: Displacements used in simplified the method on the Simple Bridge

Case 1	The South Abutment	The South Column	The Central Column	The North Column	The North Abutment
Support index	0	1	2	3	4
$L_i[m]$	0	30	60	90	120
$L_{\alpha v,i}[m]$	30	30	30	30	30
$d_i, Set A[m]$	0.0000	0.0135	0.0270	0.0405	0.0540
$d_i, Set B[m]$	0.0034	-0.0034	0.0034	-0.0034	0.0034

4.3.7 MPRS Method of Der Kiureghian and Neuenhofer

As indicated in Chapter 2.2.5, Der Kiureghian and Neuenhofer's method involves quite complicated expressions and mathematics. The method has yet to be implemented in any commercial software; therefore, the method was manually implemented in MatLab following the chronology presented in Figure 2.8.

Response Spectra, Peak Ground Displacement, and Strong-Motion Duration

The response spectra used as input were the same as the ones used in the MPRS analysis, and the relation between spectra and locations can be observed in Table 4.6.

Displacement response spectrum were developed through

$$S_d = \omega^{-2} S_a \tag{4.6}$$

where S_a is the acceleration response spectrum and ω is the frequency. Furthermore, PGD is equal to the value of S_d at low frequencies. Even though the method describes u_{max} to be equivalent to PGD, the permanent displacements estimated by Aas-Jakobsen were used as u_{max} for comparative reasons.

There are multiple definitions of strong-motion duration; therefore, no unambiguous value for τ exists (Salmon et al., 1992). Regardless of definitions, strong-motion duration relates to how wide the dominating part of an accelerogram is. Figure 4.13 illustrates that it is difficult to choose a strong-motion duration which is representative for all time histories at all excitation points. In the analyses conducted in this paper, the strong-motion duration was set to 30 seconds.

Power Spectral Densities

Due to the fact that the bridge's first natural frequencies are relatively small, the first order approximation proposed in (2.49) and (2.50) was used for the auto-PSDs. Similar to (Nakamura et al., 1993, p. 11), $\omega_f = 0.705$ rad/sec and $p = 3$ were used. However, Der Kiureghian and Neuenhofer state that the response is not overly sensitive to neither of these parameters, nor the strong-motion duration (Der Kiureghian and Neuenhofer, 1992). In accordance with EC8-2 (D.22), the peak factor for the oscillator response was set to $p_s(\omega) = 2.5$.

Support Conditions, Coherency Functions, and Cross-Power Spectral Densities

As stated in Chapter 4.2.5, ground type C was assumed to correspond to the applied response spectra. Consequently, the shear wave velocity should be $180 - 360$ m/s (EC8-1, Table 3.1). Due to lack of information, $v_s = 250$ m/s was chosen. Figure 2.2 presents the relation between v_{app} and v_s through ψ. Due to lack of information regarding the origin of shear waves,
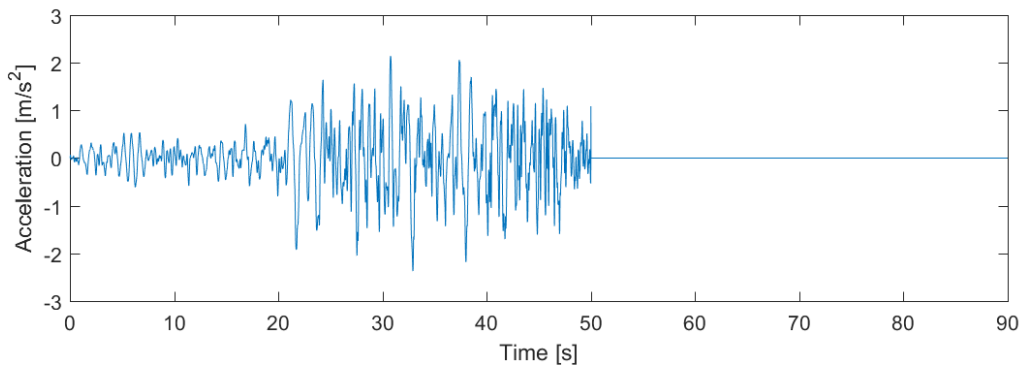
(a) Short strong-motion duration
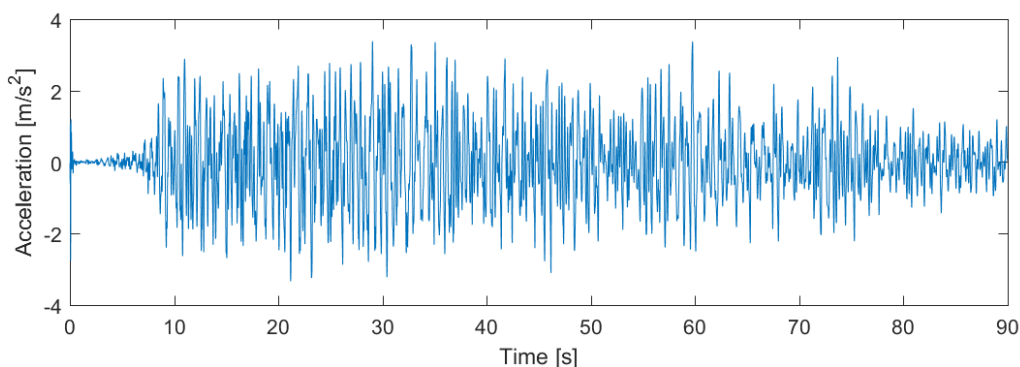
(b) Long strong-motion duration

Figure 4.13: Short and long strong-motion duration

the propagation angle, ψ, was set to be 90 degrees, making $v_{app} = v_s = 250$ m/s.

Comparable to strong-motion duration, the incoherency factor, α, is difficult to set. Authors such as Luco and Wong (1986), Nuti et al. (2011), and Zerva (2016) have tried to evaluate the factor's importance. In general, the factor decreases with increasing frequencies and intermediate distance between supports. E.g., Nuti et al. (2011) propose α within [0.02, 0.5]. Due to the bridge's medium size and relatively high frequencies compared to other bridges, the incoherence factor was set to $\alpha = 0.10$ (Todorovska et al., 2015).

The earthquake motion was assumed to travel along the longitudinal axis of the bridge. Therefore, the horizontal distance, d_{kl}, and the projected horizontal distance, d_{kl}^L, between support k and l were equal. Consequently, d_{kl} corresponds to the intermediate distances between the supports.

The cross-PSDs were found by (2.51)-(2.53), which combines the coherency effect from wave passage and incoherency with the auto-PSDs.

Natural Frequencies, Frequency Response Functions, and Cross-Correlation Coefficients

The first 30 natural frequencies were found by performing a modal analysis in ANSYS. In correspondence with Chapter 4.3.4, the damping ratios of all modes were set to 5%. In addition, frequency transfer functions, mean squares, and cross-correlation coefficients were found by use of (2.54)-(2.60).

Effective Influence Coefficients and Modal Participation Factors

In order to calculate effective influence coefficients and modal participation factors, one must first express the mass and stiffness matrices in (2.41). The matrices were extracted from ANSYS; however, ANSYS does not return values for restrained DOFs. Consequently, a stiffness and mass matrix was extracted from an unconstrained model. In order to match (2.41), the elements of the matrices were sorted manually. Accordingly, 441 unconstrained and 12 constrained DOFs were used, equivalent to the other analyses for the Simple Bridge.

The modal participation factors require mode shapes as input. Mode shapes cannot be extracted directly from ANSYS. However, mode shapes are relative displacements and rotations. Therefore, the shapes were obtained as displacements and rotations from the modal analysis. Similar to the RSAs, the first 30 modes were used.

Mean Peak Response

Der Kiureghian and Neuenhofer's method can be adjusted to calculate various responses, such as forces, stress, strains, displacements, etc. For comparative reasons, the forces and moments were of interest. The transfer vector for the ith run of the method was chosen to be:

$$\mathbf{q}_i^T = [0_1, 0_2, ... 0_{i-1}, 1_i, 0_{i+1}, ..., 0_n] \tag{4.7}$$

A transfer vector in this fashion will cause the response quantity, z, to return the displacement or rotation in DOF i. Therefore, the method was run n (=441) times, each with a different transfer vector. The forces and moments were found by conventional FE theory (Bell, 2012) described by

$$\mathbf{F} = \mathbf{Kz} \tag{4.8}$$

where **K** is the *n*x*n* stiffness matrix and **F** is a vector containing forces and moments at un-constrained DOFs.

Eurocode 8-2, Annex D.3.4 Response Spectrum for Multiple-Support input

The implementation of the multi-point response spectrum method described in EC8-2 (D.3.4.3), was analogous to the steps described for Der Kiureghian and Neuenhofer's method. The only differences were the simplified expressions in (2.62), (2.63), and (2.65).

Chapter 5

Results

This chapter presents a selection of forces and moments obtained from conducting the procedures described in the previous chapter. The selection of results is believed to be representative for the bridges' structural behaviour due to seismic loading. However, a complete set of extracted results are given in Appendix A and B.

The response is expressed in terms of structural components, with directions corresponding to both element and global coordinate systems. Naming conventions and associated abbreviations are listed in Figure 5.1 and 5.2, and the relation between element and global coordinate systems are presented in Table 5.1 and 5.2. Due to the fact that RSAs are based on mode superposition, there is no reason to distinguish between positive and negative quantities. Hence, response from all analyses are presented in absolute values.

In dialogue with Aas-Jakobsen, it was decided to limit the results from the Chacao Bridge to pylon legs, crossbeams, piles and girder. The choice was made on the basis of which components that were most likely to be designed by the seismic action. However, due to symmetry, only results from eastern pylon legs are presented. In addition, the results from the Central Pylon are limited to piles and crossbeams due to complex load distributions in the Pylon's four inclined legs. The results from piles are restricted to the maximum moments occurring at the pile tops.

The Simple Bridge is 2-dimensional, and its movement is limited to rotation about global transverse axis and translation in global longitudinal and vertical direction. Furthermore, due to 1-dimensional excitation, effects parallel to the global longitudinal direction are considered to be of most significance. The results in 5.14-5.16 are therefore limited to axial forces

in the girder, shear forces in the columns, and moments in all components.

In addition, in order to justify the implementation of THA in ANSYS, comparative plots between RM-Bridge and ANSYS are presented in Chapter 5.2.

Table 5.1: Numeration of nodes and local coordinate systems for the Chacao Bridge

Bridge component	Node series	Element X-direction	Element Y-direction	Element Z-direction
Legs, the South Pylon	4000-	Along element axis, positive upwards	Global X-direction, positive towards South	Global Z-direction, positive towards East
Legs, the Central Pylon	6000-	Along element axis, positive upwards	Global X-direction, positive towards South	Global Z-direction, positive towards East
Legs, the North Pylon	8000-	Along element axis, positive upwards	Global X-direction, positive towards South	Global Z-direction, positive towards East
Crossbeams	Same as legs	Along element axis, positive towards East	Global Y-direction, positive upwards	Global X-direction, positive towards South
Piles, the Central Pylon	56000-	Along element axis, positive upwards	Global X-direction, positive towards South	Global Z-direction, positive towards East
Piles, the North Pylon	58000-	Along element axis, positive upwards	Global X-direction, positive towards South	Global Z-direction, positive towards East
Girder	11000-	Along element axis, positive towards North	Global Y-direction, positive upwards	Global Z-direction, positive towards East

Table 5.2: Numeration of nodes and local coordinate systems for the Simple Bridge

Bridge component	Node series	Element X-direction	Element Y-direction	Element Z-direction
The South Column	1001-1010	Along element axis, positive upwards	Global Y-direction, positive towards West	Global X-direction, positive towards South
The Central Column	2001-2010	Along element axis, positive upwards	Global Y-direction, positive towards West	Global X-direction, positive towards South
The North Column	3001-3010	Along element axis, positive upwards	Global Y-direction, positive towards West	Global X-direction, positive towards South
Girder	4001-4121	Along element axis, positive towards North	Global Y-direction, positive towards West	Global Z-direction, positive upwards

1: The South Pylon, eastern leg
Abbreviation: SP leg

2: The North Pylon, eastern leg
Abbreviation: NP leg

3: The South Pylon, lower crossbeam
Abbreviation: SP LC

4: The Central Pylon, lower crossbeam
Abbreviation: CP LC

5: The North Pylon, lower crossbeam
Abbreviation: NP LC

6: The South Pylon, upper crossbeam
Abbreviation: SP UC

7: The Central Pylon, upper crossbeam
Abbreviation: CP UC

8: The North Pylon, upper crossbeam
Abbreviation: NP UC

9: Girder
Abbreviation: Girder

10: The Central Pylon, pile tops
Abbreviation: CP pile

11: The North Pylon, pile tops
Abbreviation: NP pile

Figure 5.1: Naming convention for structural components for the Chacao Bridge

1: The South Abutment
Abbreviation: SAb

2: The North Abutment
Abbreviation: NAb

3: Girder
Abbreviation: Girder

4: The South Column
Abbreviation: SC

5: The Central Column
Abbreviation: CC

6: The North Column
Abbreviation: NC
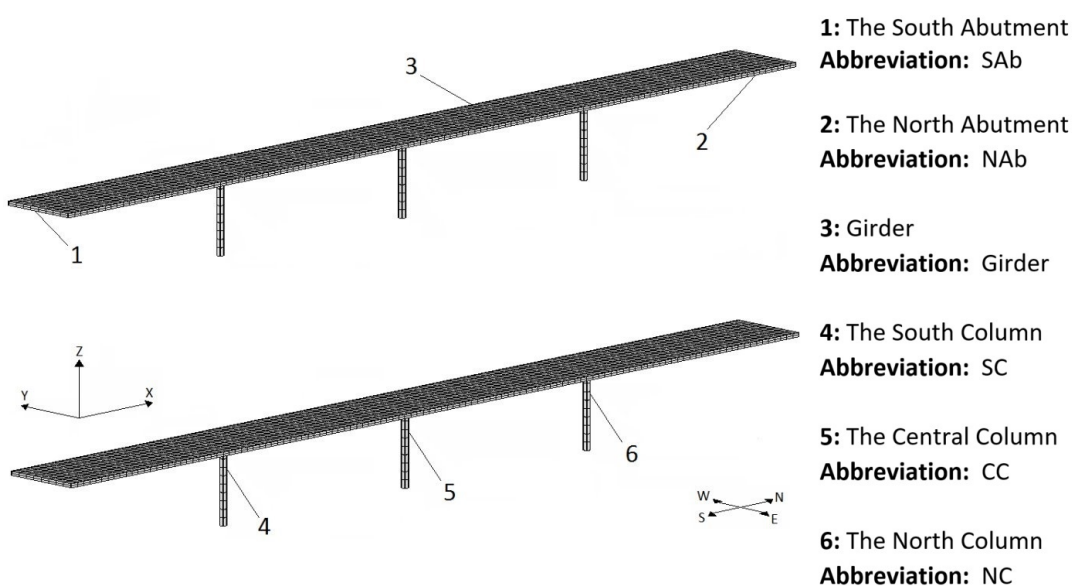
Figure 5.2: Naming convention for structural components for the Simple Bridge

5.1 Results from the Chacao Bridge

(a) Moment about global longitudinal axis (My)

(b) Moment about global transverse axis (Mz)
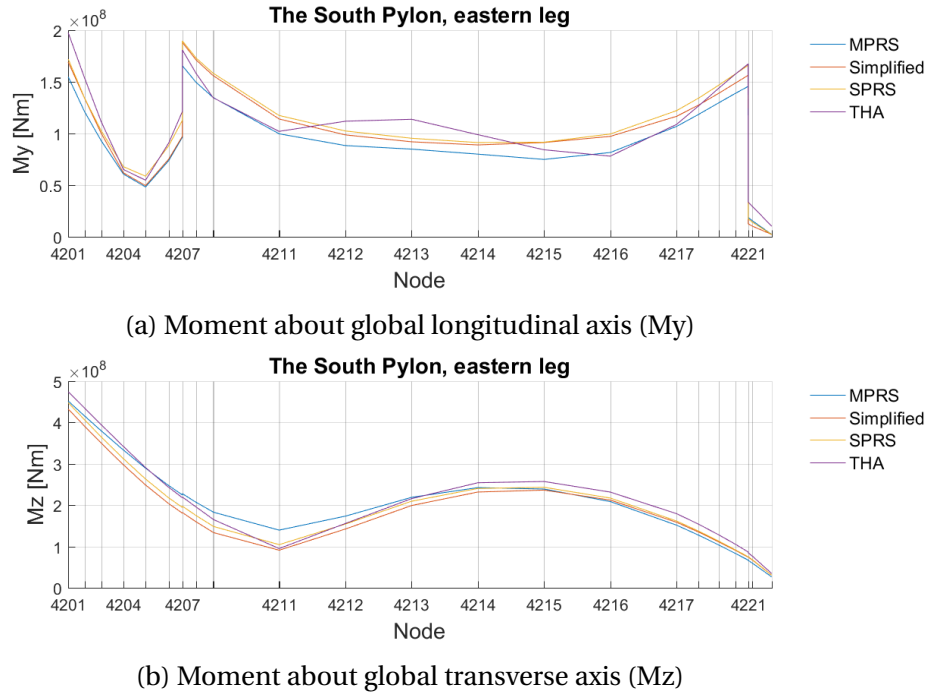
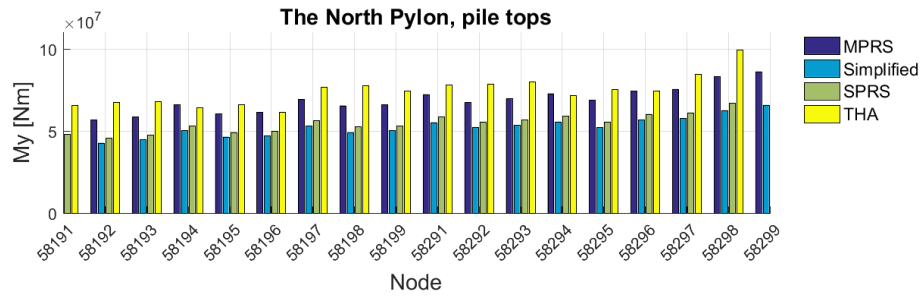Figure 5.3: Comparison of response in the South Pylon, eastern leg
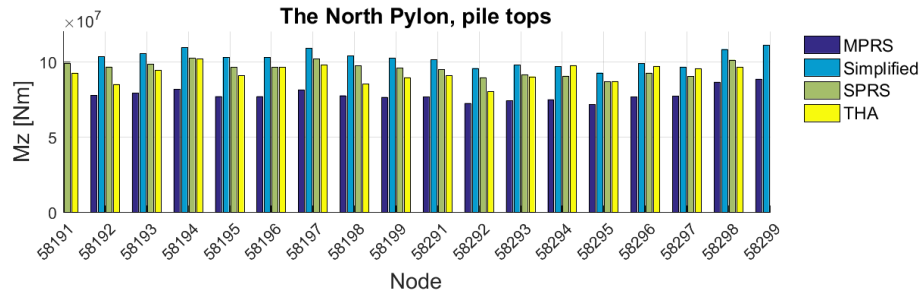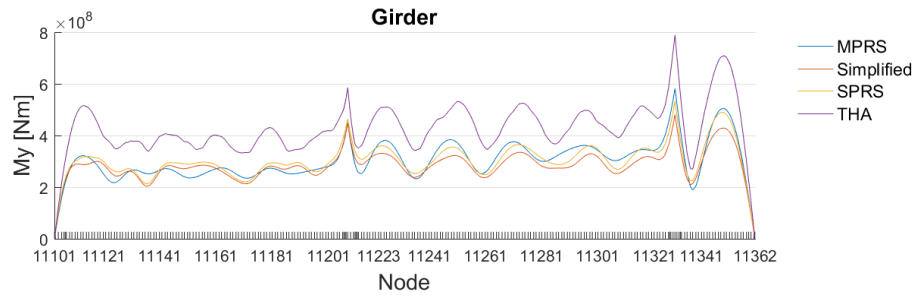

(a) Moment about global transverse axis (Mx)

(b) Moment about global vertical axis (My)
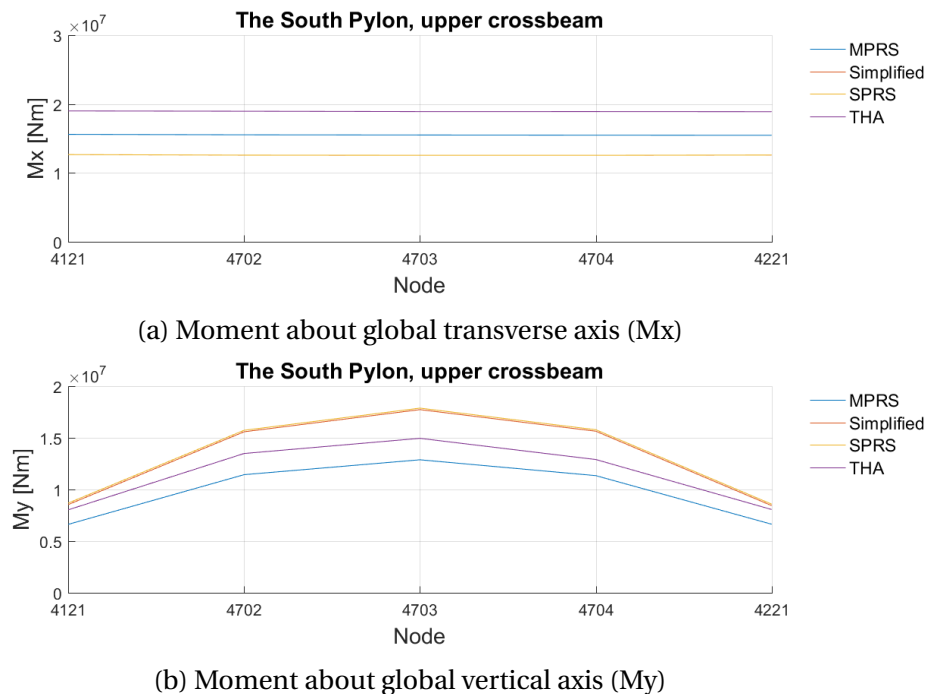
Figure 5.4: Comparison of response in the South Pylon, upper crossbeam
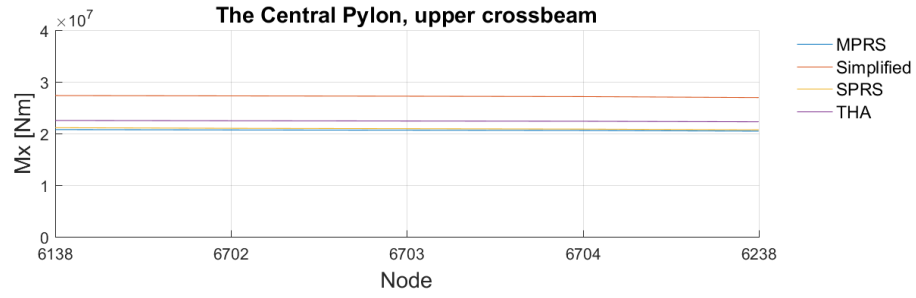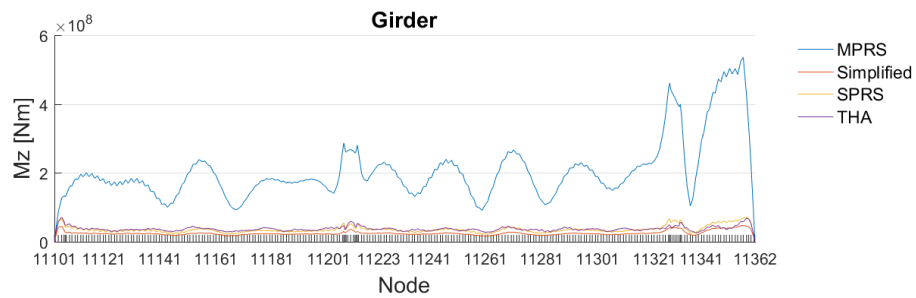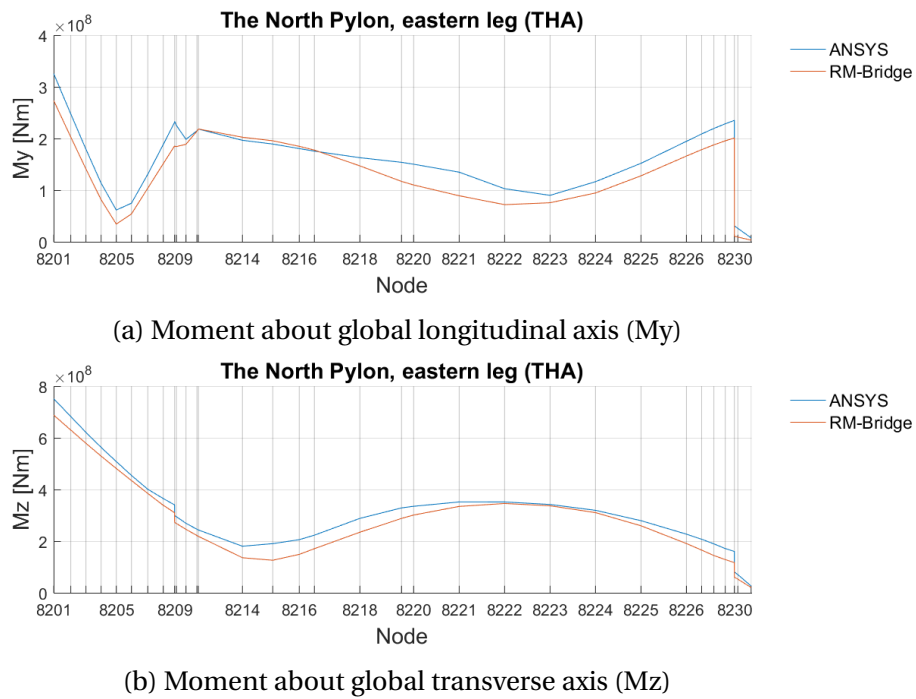
(a) Moment about global transverse axis (Mx)
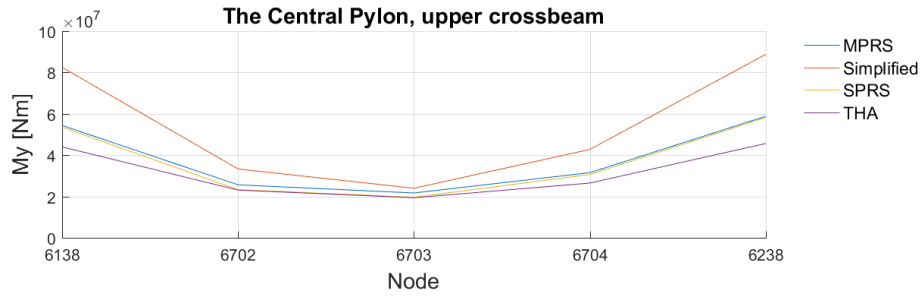
(b) Moment about global vertical axis (My)

Figure 5.5: Comparison of response in the Central Pylon, upper crossbeam
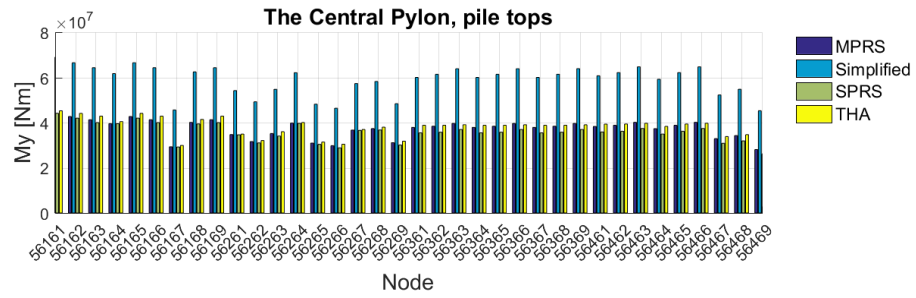
(a) Moment about global longitudinal axis (My)
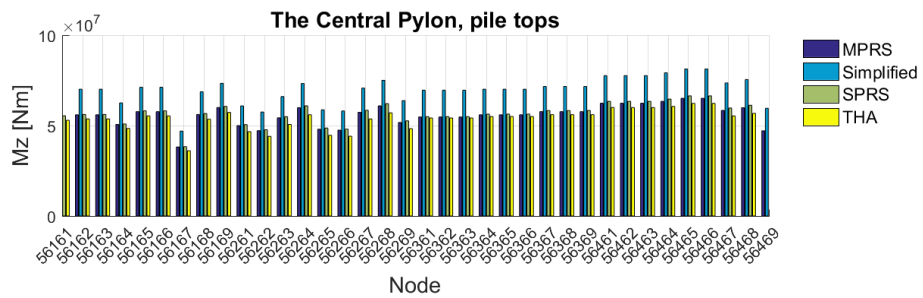
(b) Moment about global transverse axis (Mz)

Figure 5.6: Comparison of response in the Central Pylon, pile tops
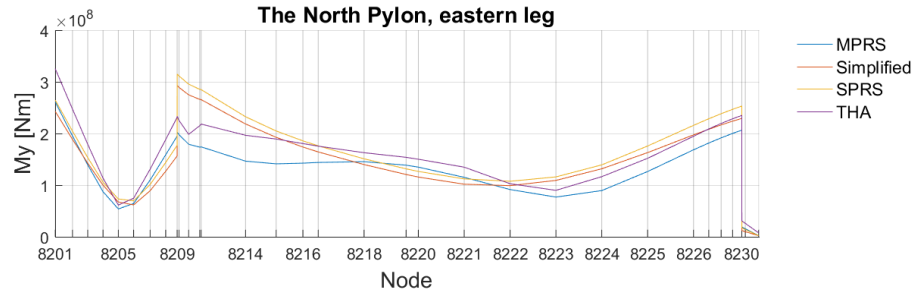
(a) Moment about global longitudinal axis (My)
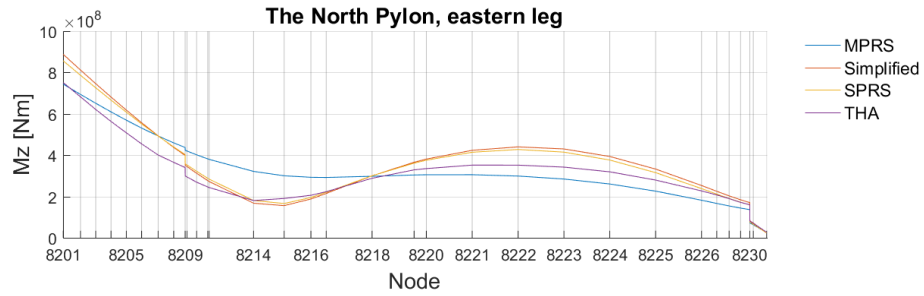
(b) Moment about global transverse axis (Mz)
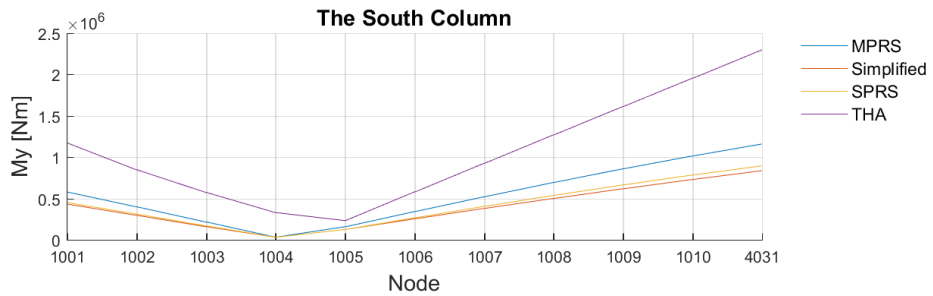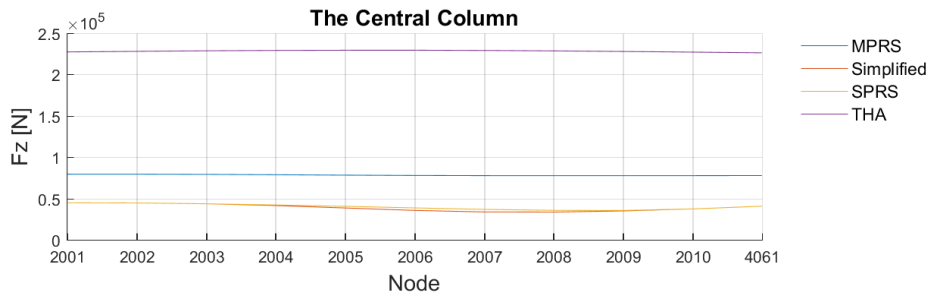
Figure 5.7: Comparison of response in the North Pylon, eastern leg
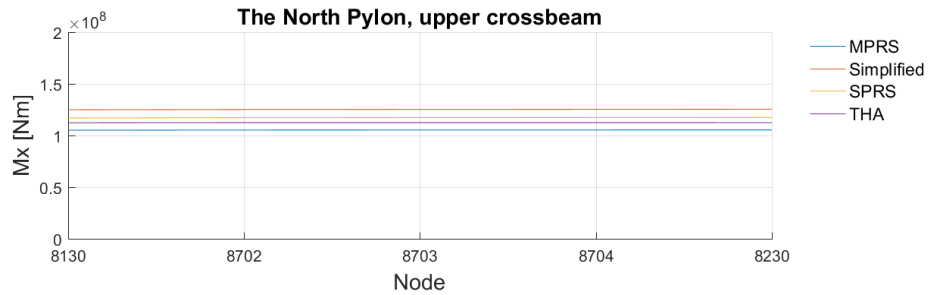
(a) Moment about global transverse axis (Mx)
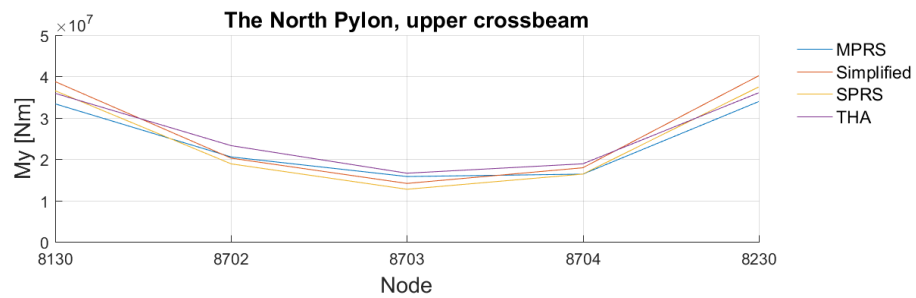
(b) Moment about global vertical axis (My)

Figure 5.8: Comparison of response in the North Pylon, upper crossbeam

(a) Moment about global longitudinal axis (My)

(b) Moment about global transverse axis (Mz)

Figure 5.9: Comparison of response in the North Pylon, pile tops

(a) Moment about global vertical axis (My)

(b) Moment about global transverse axis (Mz)

Figure 5.10: Comparison of response in the girder

5.2   Results From the Chacao Bridge in ANSYS and RM-Bridge

(a) Moment about global longitudinal axis (My)

(b) Moment about global transverse axis (Mz)

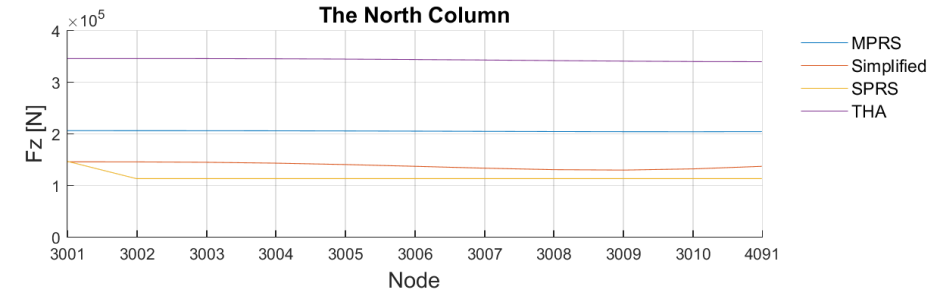Figure 5.11: Comparison of response in the North Pylon, eastern leg

(a) Moment about global vertical axis (My)

(b) Moment about global transverse axis (Mz)
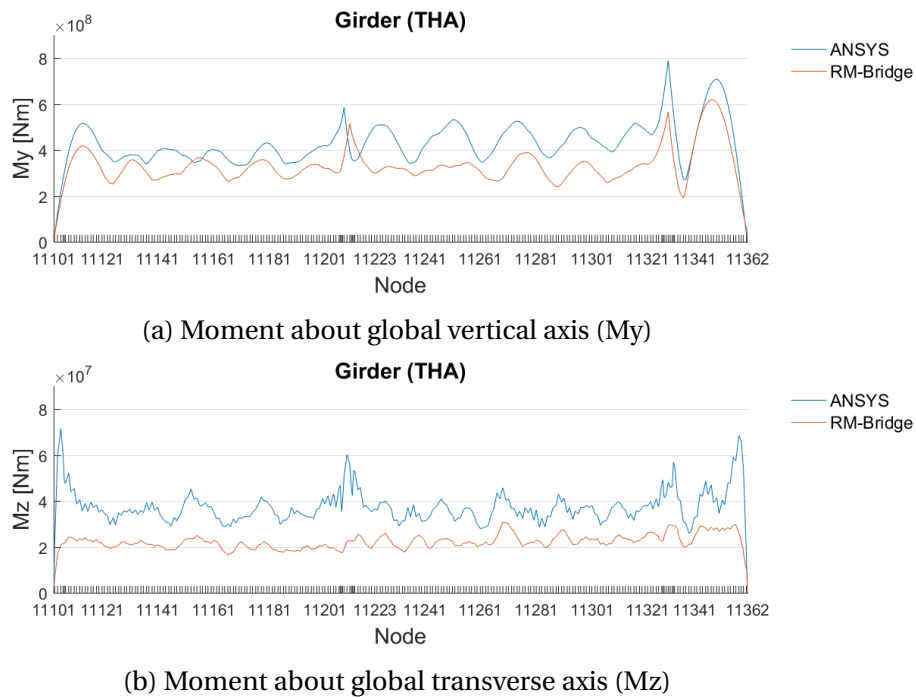
Figure 5.12: Comparison of response in the girder

5.3 Results From the Simple Bridge
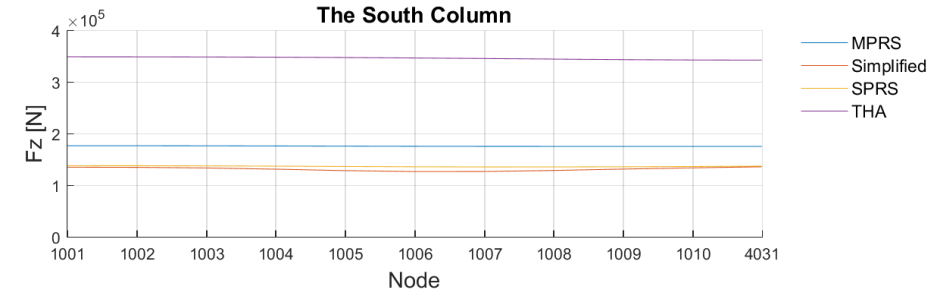
(a) Force along global longitudinal axis (Fz)

(b) Moment about global transverse axis (My)

Figure 5.13: Comparison of response in the South Column
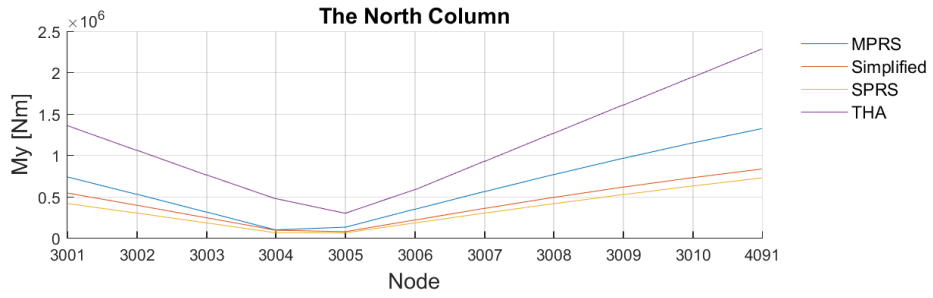

(a) Force along global longitudinal axis (Fz)
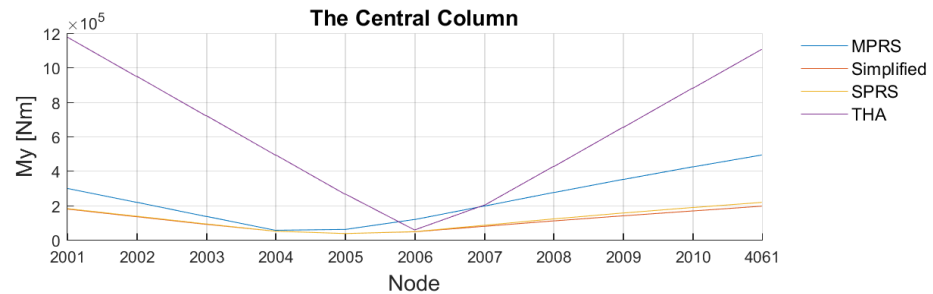
(b) Moment about global transverse axis (My)

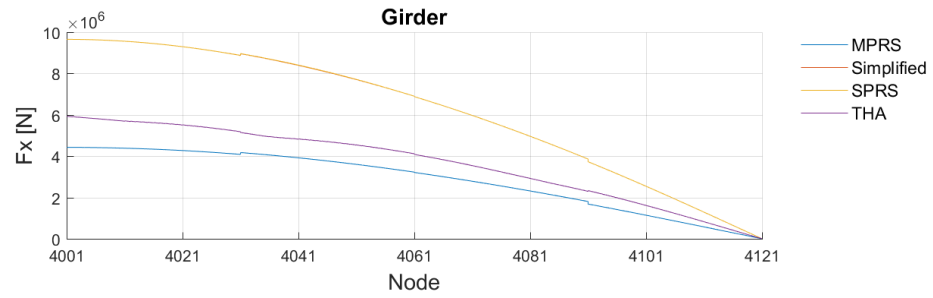Figure 5.14: Comparison of response in the Central Column
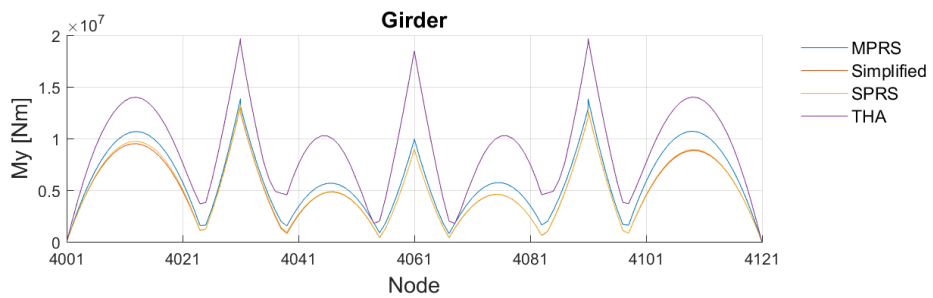
(a) Force along global longitudinal axis (Fz)

(b) Moment about global transverse axis (My)

Figure 5.15: Comparison of response in the North Column

(a) Force along global longitudinal axis (Fx)

(b) Moment about global transverse axis (My)

Figure 5.16: Comparison of response in the girder

Chapter 6

Discussion

6.1 Comparison of ANSYS and RM-Bridge

Chapter 3.2 presents a comparison of modal analyses conducted in RM-bridge and ANSYS. Results are close to identical because of a mean deviation of just 0.65% for the first 30 natural frequencies. Due to the principle of mode superposition, a similar correlation is expected for results from response spectrum analyses.

In contrast, THA is not based on mode superposition; therefore, the responses from the two finite element programs are compared. It should be noted that neither the finite element model nor the implementation of analyses are identical in ANSYS and RM-Bridge. Even though the FE model in ANSYS was based on information from Aas-Jakobsen, minor deviations are inevitable. Nevertheless, if implemented correctly, there should be a clear correlation of the results.

Accelerograms are identical for THA in both FE models such that the deviations arise due to differences in the FE models and implementation of analyses. Figure 5.11 indicates correspondent results for the North Pylon. Therefore, pylons and THA are assumed to be implemented correctly. Nevertheless, small deviations are observed, and believed to originate from the absence of soil damping in ANSYS.

Figure 5.12 displays an overwhelming difference of moment distributions in the girder. Additionally, in Figure A.23-A.25, THA appears significantly larger than the RSAs conducted in ANSYS. Therefore, the ANSYS-model is believed to overestimates the girder's response in THAs, especially for Mz.

Since deviations are far greater in the girder than the other components, the cause of error is not believed to be the lack of soil-damping. Therefore, the overall discussion for the Chacao Bridge is limited to pylon legs, crossbeams and piles. The deviating results in the girder are further investigated in Chapter 7.

6.2   Time History Analysis as Reference

Results obtained from a complex finite element model will always display minor deviations compared to reality, yet, a thorough model may provide sufficiently accurate results. Results obtained from THAs are deterministic, while RSAs are statistically founded. Therefore, THA is assumed to provide the most accurate results, and is used as basis for comparison in the following discussion.

THAs are, to a certain extent, influenced by assumptions. Chapter 4.2.2 mentions that results from individual analyses may be combined differently depending on the number of seismic events simulated. In this research, seven seismic events were simulated, such that the response is taken as the average. When less than seven events are available, the maximum response must be used.

Figure 6.1 illustrates the difference between using maximum and mean values for the seven seismic events simulated on the Chacao Bridge. The blue horizontal zero-axis corresponds to the maximum response using mean values, while the red dots represent the deviation using maximum values. The maximum values are in general 10-25% higher than the mean. However, statistical outliers representing deviation up to 35% are observed.

Figure 6.1 proves that choice of combination may have great impact on the response from THAs. Because the results from the THAs are chosen as reference results, deviations to the
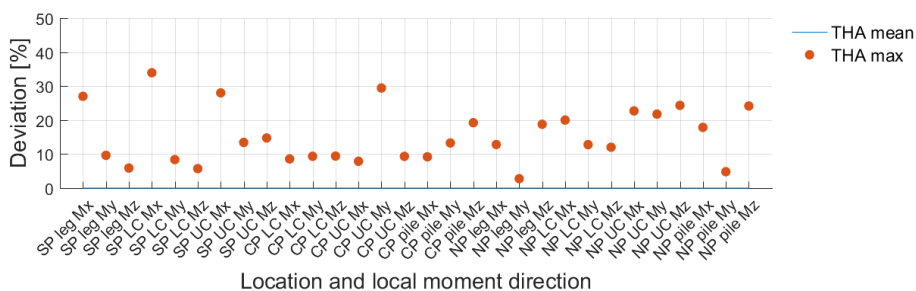

Figure 6.1: Deviations for THAs with maximum and mean values for the Chacao Bridge

other analyses are affected by the choice of combination. In addition, since THAs and RSAs are fundamentally different, even greater deviations must be tolerated. Therefore, a general deviation of ±30% relative to THA is considered reasonable.

6.3 The Chacao Bridge

6.3.1 Investigation of Relative Magnitudes

The results from the Chacao Bridge are summarized in Figure 6.2 and 6.3. The purple zero-line represents results from THA, while the scatter plots denote the corresponding deviation from the remaining analyses. Figure 6.2 illustrates the deviation from maximum response in each component, while Figure 6.3 demonstrates the mean deviation. In addition, Table 6.1 and 6.2 lists the corresponding ranking. E.g. SPRS yields largest maximum response in 5/30 cases, and produces the largest mean deviation in 13/30 cases.

The simplified method tends to overestimate the maximum response and is the most conservative analysis in 15/30 cases. Furthermore, in 18/30 cases, the simplified method provides the largest deviation from the mean response. Note that huge deviations are observed at the Central Pylon. Out of the analyses of investigation, the simplified method provides the undoubtedly worst statistics in terms of magnitude. However, as intended, the method is in general conservative and provides results within the 30% threshold.

Compared to the simplified method, SPRS provides results of equal or better magnitude. No statistical outliers are observed, and all results are considered acceptable. However, the deviations from the maximum response are fluctuating, such that no conclusion can be made of whether the analysis is conservative or in general underestimates the response.

On the contrary, MPRS yields more stable results. All deviations, from both mean and maximum, are within the tolerable threshold. In 20/30 cases MPRS provides the lowest maximum results, which implies that the analysis tends to underestimate the response. Consequently, the need for a safety factor may be discussed and bring the response even closer to the THA.
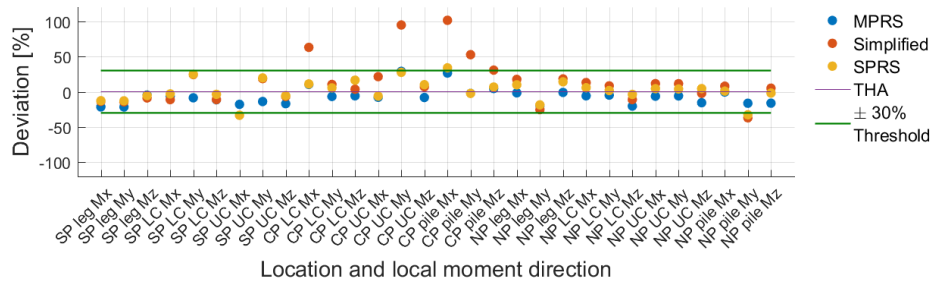
Figure 6.2: Deviation from maximum response in THA for all components and forces

Table 6.1: Results ranked from highest to lowest response

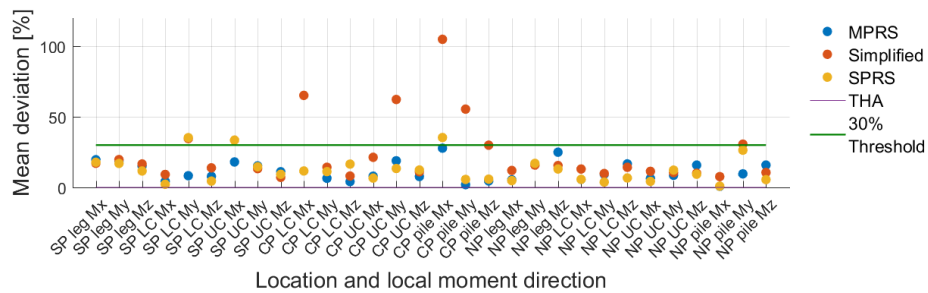| Relative magnitude	MPRS	Simplified	SPRS	THA
1st	0	15	5	10
2nd	4	4	18	4
3rd	6	6	6	12
4th	20	5	1	4

Figure 6.3: Mean deviation from THA for all components and forces

Table 6.2: Mean deviation from THA ranked from lowest to highest

Mean deviation from THA	MPRS	Simplified	SPRS
1st	13	4	13
2nd	10	8	12
3rd	7	18	5

6.3.2 Impact of Pseudo-Static and Permanent Displacements

Effects from pseudo-static and permanent displacements are in general low, and the results are dominated by the response from the spectrum analyses. Significant effects are only observed in the pylons. Compared to the spectrum solution, magnitudes are within 10%. Figure 6.4 illustrates the low impact of displacements in the leg of the South Pylon. The pseudo-static displacements are limited to the global transverse direction, while the SPRS and MPRS analyses include permanent displacements in all translational directions. Due to low impact from permanent displacements on the total response, contribution from each direction has not been investigated.

6.3.3 The Simplified Method

The simplified method is usually conducted with the design spectrum from EC8-1 as input. However, due to lack of geotechnical reports, the intended design spectra could not be made. Therefore, the analysis was conducted with the site-specific spectrum made for the South Pylon, making the procedure identical to the SPRS analysis for the South Pylon. As a result, the difference in Figure 5.3-5.4, is due to the impact of permanent and pseudo-static displacements.

The simplified method uses the same seismic input motion for all supports. Large deviations are observed for the Central Pylon in Figure 6.2 and 6.3, and occur due to use of too conservative spectra at the Pylon's location. The transverse spectra for the South Pylon, the Central Pylon and the North Abutment are displayed in Figure 6.5. The figure illustrates a considerable difference for periods below 1s. Natural frequency number 98 is approximately at 1 Hz; consequently, the response from larger natural frequencies may be significantly af-
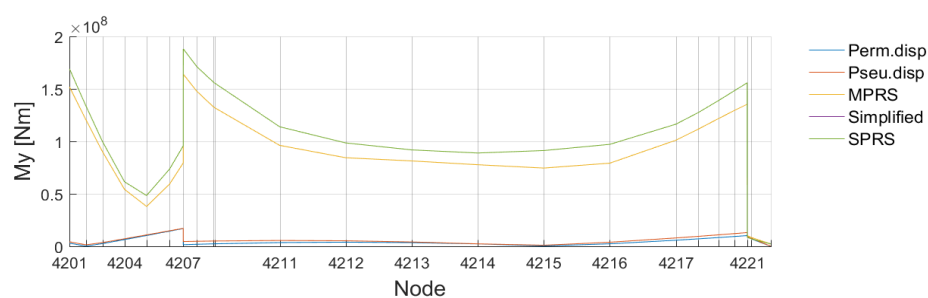

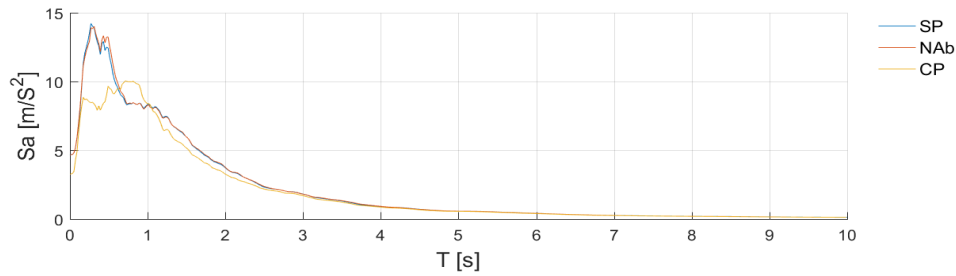Figure 6.4: Effects from displacements in the South Pylon, eastern leg

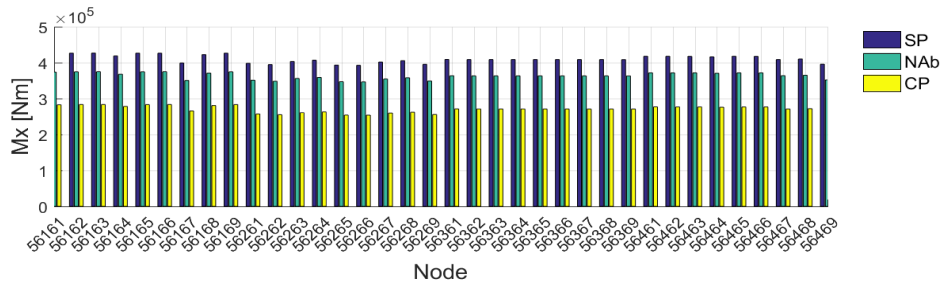Figure 6.5: Transverse response spectrum at different locations

Figure 6.6: Results from the simplified method with different spectra

fected by choice of spectrum. To illustrate how results may vary with different input spectra, an additional SPRS analysis was conducted. Figure 6.6 displays the results from the pile tops at the Central Pylon. From the Figure, it is evident that the choice of spectra is of great importance, and that the spectra for the South Pylon is likely to overestimate the response compared to THA. As a result, the use of the spectra for the South Pylon may have resulted in unrealistically large responses in the components of the Chacao Bridge.

6.3.4 MPRS and SPRS Analyses

There are three main differences between the MPRS analysis and the SPRS analysis in AN-SYS: 1) the number of spectral values allowed in each response spectrum, 2) the number of supports being excited at the same time, and 3) the use of multiple spectra in one analysis.

The impact of reducing the number of spectral values is uncertain without further investigation. However, it is clear from Figure 4.5 that the reduced spectrum no longer represent the damping-dependent response spectrum with 1500 values. Some modes will be amplified while other modes will be attenuated. The change in response is dependent on which modes that dominate the response in the direction and component of interest. In order to produce more comparable results from MPRS and SPRS analyses, one may neglect the variation of modal damping ratio and use spectra with equivalent damping. Use of spectra with

equivalent damping ratio and the corresponding consequences have not been investigated.

In order to examine the effect of exciting individual supports, MPRS analyses were conducted with the same combination of spectra as used in SPRS. This approach is called "MPRS/SPRS approach". A total of 18 MPRS/SPRS approach analyses were conducted in ANSYS, one for each directional component in each set of site-specific spectra. Figure 6.7 is a representative example from the results, and presents My in the leg of the North Pylon. Overall, good agreement was observed between the response from the MPRS/SPRS approach and the response from the regular MPRS analysis. Therefore, the number of spectra in one analysis have low impact on the final results. The deviation between MPRS and SPRS arise either due to excitation of an unequal number of supports at the same time, or due to the difference of spectral values allowed in each spectrum.

MPRS is not a common feature in FE software. In order to be established as a reliable method, it must yield response comparable to already well established methods, such as the SPRS. The methodology behind SPRS analyses is well recognized. Conversely, the approach of the MPRS-function in ANSYS has not been tested thoroughly. Implicitly, the consequences of using the MPRS-function are unknown. By excitation of only one support, certain mode shapes may be excited more than others. E.g., when exciting the North Pylon, mode shapes dominated by the North Pylon may be of greatest impact. For a better understanding of the methodology behind the MPRS-function, an investigation is carried out in Chapter 7.

Inconsistent results were observed for the MPRS analysis' response in the girder. Especially, the moment about the transverse axis is deviant, see Figure 5.10b. The response is of extreme magnitude, and is believed to arise either due to modelling error or the combination of a complex model and the methodology of the MPRS-function. The deviating results for Mz and Fy in the girder are investigated in Chapter 7.
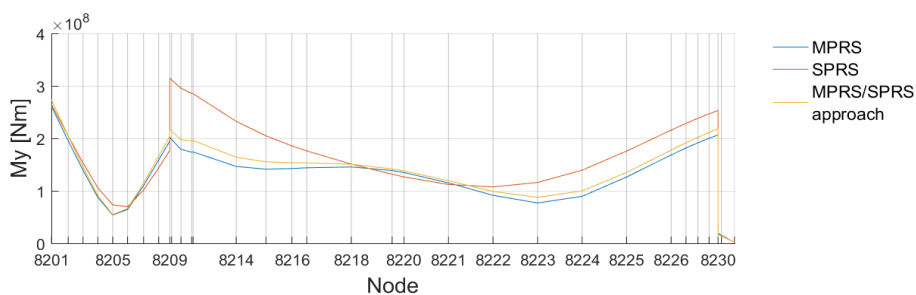

Figure 6.7: MPRS analysis with SPRS approach for the North Pylon

6.3.5   Shape of the Response

All of the methods investigated in this research present similar shape of response. This is observed in Figure 5.3-5.10. By Figure 5.7a, one may observe that the largest deviations occur for the SPRS and the simplified method in the transition between the pylon legs and the cross beams. The greatest match in relation to THA is observed for the MPRS-function.

6.4   The Simple Bridge

6.4.1   Time History Analysis

The results from the Simple Bridge reveals that THA provides the highest response in 11/12 cases. Since the other methods are alleged to be conservative, the results seem worrying. However, the results are likely to be misleading. At first, the analyses were conducted with inclusion of permanent displacements. Results from the Simple Bridge showed that the permanent displacements dominated the response of the THA. Consequently, the static effects were attempted removed.

Chapter 4.3.1 describes that permanent displacements were removed using the Butterworth high-pass filter. The cutoff frequency for the Butterworth filter was chosen based on the visual appearance of the displacement histories, and the only requirement was that the displacements oscillated about the zero-axis. Due to the large response from THAs, the cutoff frequency of 0.10 Hz is most likely too low. Consequently, not all traces of permanent displacements may have been removed, which might have lead to additional static forces in the THA.

In addition, inaccuracies may have occurred due to potential underestimation of damping. Natural frequency number 1 and 13 were used to estimate Rayleigh constants. Intermediate frequencies are underdamped compared to the RSAs. Due to high effective modal mass in this frequency range, the response from the THA may have been amplified.

6.4.2 Investigation of Relative Magnitudes

As for the Chacao Bridge, scatter plots and tables are made to present the deviation and ranking relative to THA. Correspondingly, deviation relative to the maximum values are displayed in Figure 6.8 and Table 6.3, while deviation relative to the mean is illustrated by Figure 6.9 and Table 6.4.

Figure 6.8 and 6.9 present deviations in the range 30-80%. However, as discussed in Chapter 6.2 and 6.4.1, there are multiple factors which may have enhanced the response from the THA. Due to uncertainties regarding THA, the ranking tables may be misguiding. Nevertheless, the scatter plots propose good agreement between the RSAs.

Striking similarities between the simplified method and SPRS can be observed in the scatter plots. The two analyses are almost indistinguishable, apart from the results for the North Column. Regardless of the THA's potential inaccuracies, except from the axial forces in the columns, deviations for the SPRS analysis and the simplified method do not seem to fluctuate much. Nonetheless, the SPRS analysis and the simplified method undoubtedly present the response of smallest magnitude.

MPRS provides results of equal or greater magnitude than SPRS and the simplified method in 11/12 response quantities. In addition, the deviations between MPRS and SPRS are relatively consistent for all components.

Gravitational loads were assumed to dominate the response vertically. Therefore, regardless of analysis, shear forces (Fz) and moment (My) in the girder, and axial forces (Fx) in the columns were expected to be close to identical. The results prove otherwise. By further investigation, one may observe that the shear forces in the girder are of greater magnitude in the THA. Consequently, more shear forces from the girder are transferred as axial forces in the columns in the THA.
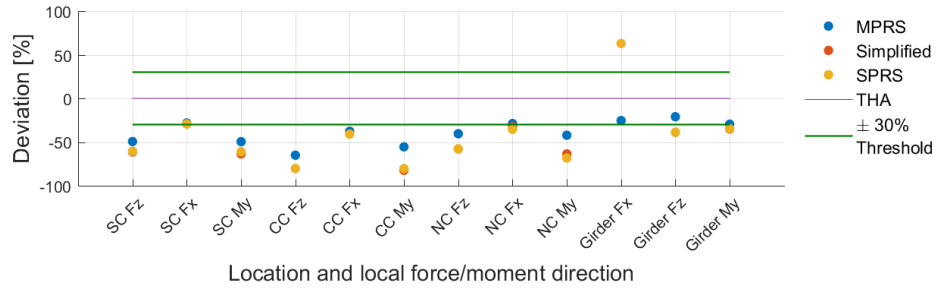
Figure 6.8: Deviation from maximum response in THA for all components and forces

Table 6.3: Results ranked from highest to lowest response

Relative magnitude	MPRS	Simplified	SPRS	THA
1st	0	1*	1*	11
2nd	11	0	0	1
3rd	0	8*	9*	0
4th	1	3*	2*	0

* Simplified and SPRS share seven positions
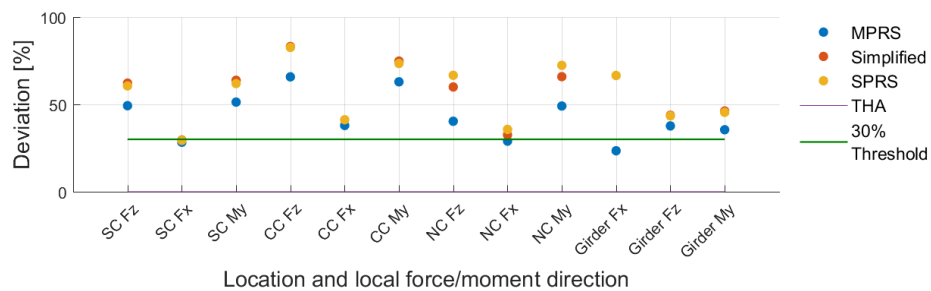
Figure 6.9: Mean deviation from THA for all components and forces

Table 6.4: Mean deviation from THA ranked from lowest to highest

Mean deviation from THA	MPRS	Simplified	SPRS
1st	12	0	0
2nd	0	9*	9*
3rd	0	3*	3*

* Simplified and SPRS share six positions

6.4.3 The Simplified Method

Due to striking similarities between the simplified method and SPRS, two conclusions can be made. Firstly, the effect of pseudo-static displacements is marginal. Even though permanent displacements demonstrated great impact in Chapter 4.3.1, the pseudo-static displacements in the simplified method prove small to insignificant influence. Similar to the Chacao Bridge, pseudo-static displacements account for less than 10% of the total response. The displacements were calculated based on the Simple Bridge's geometry and were applied in the transverse direction. Thus, the displacements match the size of the Bridge and do not dominate the response. Application of transverse displacements mainly give rise to forces in the corresponding direction. Therefore, pseudo-static displacements hardly affect the results in Figure 5.13-5.16.

Secondly, because the spectrum solution outweighs the pseudo-static solution, the simplified method is sensitive to choice of spectrum. However, the method is normally based on a design spectrum from EC8-1, yet, the method's sensitivity of spectrum still applies. Therefore, it is important to create a spectrum based on the poorest soil condition along the structure of interest.

6.4.4 MPRS and SPRS Analyses

Conversely to the Chacao Bridge, the MPRS method yields the largest response of the RSAs. Furthermore, one of the distinctions between the SPRS and MPRS analyses has been eliminated for the Simple Bridge. Due to the choice of 5% equivalent damping ratio for all modes, 100 values are sufficient to describe a response spectrum. Therefore, the difference originate either from the excitation process or due to multiple spectra in one analysis. The latter is probably of impact; yet, it was proven to be of low significance for the Chacao Bridge in Chapter 6.3.4.

The difference between the response from the MPRS and the SPRS analyses is believed to emerge mainly due to the procedures of excitation. Mode superposition is reliant on which mode shapes that are excited during the analysis. However, which modes are being activated may vary depending on whether one or all supports are excited simultaneously. In addition, the impact from each mode is based on the mode's effective modal mass. If a different mode with different effective modal mass is excited, the response may change significantly.

Based on the different results from MPRS and SPRS for the Chacao Bridge and the Simple Bridge, a theory built upon change of activated mode shapes has been developed. The impact from change of dominating mode shapes may be dependent on the stiffness and size of a structure. By exciting only one support in a rather stiff and small structure, most modes will affect all structural components. These modes are from hereon referred to as "global modes".

Subsequently, the entire structure will be affected by each spectrum defined in the MPRS analysis. This may be associated with a single SPRS analysis. When a full MPRS analysis is conducted, the response from each spectrum is summed by the SRSS-rule. If one excitation is similar to one SPRS analysis, the total response will be significantly amplified for MPRS compared to SPRS.

Conversely, by exciting only one support in a large and soft structure, "local modes" will be excited, and local response may be observed. This is similar to the observation in the North Pylon as discussed in Chapter 6.3.4. As a consequence, each component's response is dominated by local excitation when using the MPRS-function. When using the SPRS-function on a large and soft structure, it excites the entire bridge, and the resulting response is likely to surpass MPRS'. This theory has been explored in Chapter 7.3.

6.4.5   Shape of the Response

In addition to magnitude, the shape of the response is of relevance. The shapes displayed in Figure 5.13-5.16 suggest great similarities. It seems like if a response from a method was scaled by a constant value, it would be possible to replicate the shape and magnitude from the THA. However, as indicated in Chapter 6.4.1, THA has most likely overestimated the response for the Simple Bridge.

6.4.6   Der Kiureghian and Neuenhofer's Method

Even though Der Kiureghian and Neuenhofer's method is well recognized and even written in EC8-2 (Annex D.3.4), the method has yet to be implemented in any commercial software. Provisionally, the user must implement the method manually. As can be seen in Chapter 2.2.5, the method involves multiple complex terms; thus, the user must be careful during

implementation. Furthermore, in order to set up the stiffness, mass, and mode shape matrices, one is reliant of some kind of FE software.

The process of implementing Der Kiureghian and Neuenhofer's method was found to be strenuous and time consuming. However, the most significant downside is the uncertainty of the results due to complicated expressions and the need for self-implementation.

Although the procedure described in Chapter 4.3.7 was successfully implemented, the results from Der Kiureghian and Neuenhofer's method turned out to be incorrect. Therefore, resulting forces and moments are not included in this thesis. Note that the theory behind the method is fully capable of producing the correct response. Due to lack of time, the authors were not able to correct the error. However, the method is further investigated in Chapter 7.1.

Assumed successful implementation, the method is believed to yield the most accurate results of the RSAs due to its ability to include both the incoherency and the wave passage effect. However, the method is only capable of estimating the response in unconstrained DOFs. In other words, response at support DOFs cannot be extracted directly. This is unfortunate since the response at supports often is of greatest magnitude.

6.5   Run Time

In the industry, and especially in the consulting business, time is of the essence; therefore, accuracy must be set up against time consumption. One may believe that whether an analysis takes a couple of minutes or a couple of hours is insignificant. Generally, that is true; however, the methods are often implemented incrementally and people make mistakes. As a results, the same analyses are likely to be ran multiple times, amplifying the effect of run time. Table 6.5 and 6.6 present approximate run times for the analyses conducted in this research. Note that the tables present values for the required number of analyses. Hence, execution of analyses during implementation is not accounted for, such that the real difference for total run time is a lot greater.

As previously stated, THA is a time consuming method. Table 6.5 and 6.6 prove this statement and display huge differences in regard to run time. E.g. the most time consuming method is THA with a total run time of 14 hours for the Chacao Bridge, while MPRS only re-

quire 20 minutes to calculate the response. Moreover, the effect of having to conduct multiple analyses is not included. Multiple input files must be constructed and the software must be restarted. In addition, results from individual analyses must be combined manually, and methods that require more than one analysis would require considerably more time than what the tables suggest.

Table 6.5: Run time for analyses performed on the Chacao Bridge

Method	Number of analyses required	Approximate run time	Total run time
THA	7	2 hours	14 hours
MPRS	1	20 min	20 min
SPRS	18	20 min	6 hours
Simplified	3	20 min	1 hour

Table 6.6: Run time for analyses performed on the Simple Bridge

Method	Number of analyses required	Approximate run time	Total run time
THA	7	1 hour	7 hours
MPRS	1	10 sec	10 sec
SPRS	4	10 sec	40 sec
Simplified	1	10 sec	10 sec
Der K. & N.	1	10 min	10 min

Chapter 7

Methodology of Further Investigation

7.1   Der Kiureghian and Neuenhofer's Method

The procedure described in Chapter 4.3.7 proved to be incapable of returning forces and moments. Der Kiureghian and Neuenhofer's method involves multiple steps; therefore, it was possible to perform each step in a chronological order and examine the results. E.g. it was verified that the correlation coefficient s in (2.58) were equal to 1 for $k = l$. This means that the displacements at support k were fully correlated with itself. Displacements were obtained for both the full method and for EC8-2's simplified version, meaning that all steps until estimation of forces and moments were examined and evaluated.

The results were compared to an MPRS analysis. However, Der Kiureghian and Neuenhofer's method only yields a trivial static solution when PGDs are excluded. For comparative reasons, response from a static analysis with displacements equal to the PGDs was added to the response of the MPRS analysis.

7.2   Justification of the MPRS-Function in ANSYS

The methodology of the MPRS-function in ANSYS is explained in Chapter 4.2.4. In order to justify this approach, an analogy to THA was made: If the principle of superposition works for THAs, the MPRS-function's combination of response from multiple spectra can be justified. The analogy was tested for two cases: 1) longitudinal and 2) vertical loading of the Simple Bridge. In both cases THAs were performed with accelerograms adjusted for perma-

nent displacements. The principle is illustrated in Figure 7.1, which presents superposition of vertical displacements for the girder of the Chacao Bridge.

The principle of superposition involves partition of the response (Holden, 2017). In this research, the principle was tested for four single-input THAs. In other words, only one node in one direction was loaded in each analysis. The total response was obtained as the sum of the response from each single-input THA. Table 7.1 and 7.2 present which DOFs that were excited in each analysis, both for longitudinal and vertical loading. The tables also list which accelerograms that were used. For the naming conventions, see Table 4.2.
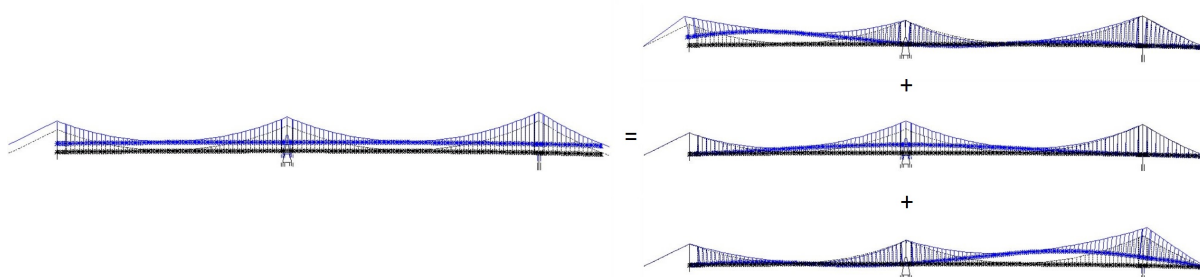
Figure 7.1: Simultaneous excitation versus sequential excitation of the Chacao Bridge

Table 7.1: Relation of horizontal input motion and location on the Simple Bridge

Analysis number	The South Abutment	The South Column	The Central Column	The North Column
1	THA_SAn_L_1		-	-
2	-	THA_SP_L_1	-	-
3	-	-	THA_CP_L_1	-
4	-	-	-	THA_NP_L_1
5	THA_SAn_L_1	THA_SP_L_1	THA_CP_L_1	THA_NP_L_1

Table 7.2: Relation of vertical input motion and location on the Simple Bridge

Analysis number	The South Abutment	The South Column	The Central Column	The North Column
6	THA_SAn_V_1		-	-
7	-	THA_SP_V_1	-	-
8	-	-	THA_CP_V_1	-
9	-	-	-	THA_NP_V_1
10	THA_SAn_V_1	THA_SP_V_1	THA_CP_V_1	THA_NP_V_1

7.3 Mode Superposition in MPRS

In order to explore the theory described in Chapter 6.4.4, multiple MPRS analyses were conducted. The MPRS-function in ANSYS combines the response from each spectrum with the SRSS-rule. In order to examine if there is a shift in dominating modes, MPRS analyses were conducted with one transverse spectrum at a time. A total of 12 analyses were conducted, seven on the Chacao Bridge and five on the Simple Bridge. The analyses and employed spectra are listed in Table 7.3 and 7.4. Note that the names of the analyses are correspondent with the legends in the results.

Table 7.3: Relation of transverse input motion and location for the Simple Bridge

Name of analysis	The South Abutment	The South Column	The Central Column	The North Column	The North Abutment
SAn	M_SAn_T_5%	-	-	-	-
SC	-	M_SP_T_5%	-	-	-
CC	-	-	M_CP_T_5%	-	-
NC	-	-	-	M_NP_T_5%	-
NAb	-	-	-	-	M_NAb_T_5%
All	M_SAn_T_5%	M_SP_T_5%	M_CP_T_5%	M_NP_T_5%	M_NAb_T_5%

Table 7.4: Relation of transverse input motion and location for the Chacao Bridge

Name of analysis	The South Anchor	The South Pylon	The Central Pylon	The North Pylon	The North abutment	The North anchor
SAn	M_SAn_T	-	-	-	-	-
SP	-	M_SP_T	-	-	-	-
CP	-	-	M_CP_T	-	-	-
NP	-	-	-	M_NP_T	-	-
NAb	-	-	-	-	M_NAb_T	-
NAn	-	-	-	-	-	M_NAn_T
All	M_SAn_T	M_SP_T	M_CP_T	M_NP_T	M_NAb_T	M_NAn_T

All spectra have been adjusted to account for mode specific damping ratio

Chapter 8

Results from Further Investigation

The response from Der Kiureghian and Neuerhofer's method does not include gravitational impact. Therefore, Figure 8.1-8.4 contain plots of displacements parallel to the direction of excitation and rotations about the global transverse axis.

The legends in Figure 8.5-8.8 are correspondent with the analysis numbers given in Table 7.1 and 7.2. The abbreviation, *A. #*, stands for *Analysis number*.

8.1   Der Kiureghian and Neuenhofer's Method

(a) Displacement along global longitudinal axis (Uz)

(b) Rotation about global transverse axis (Rot y)
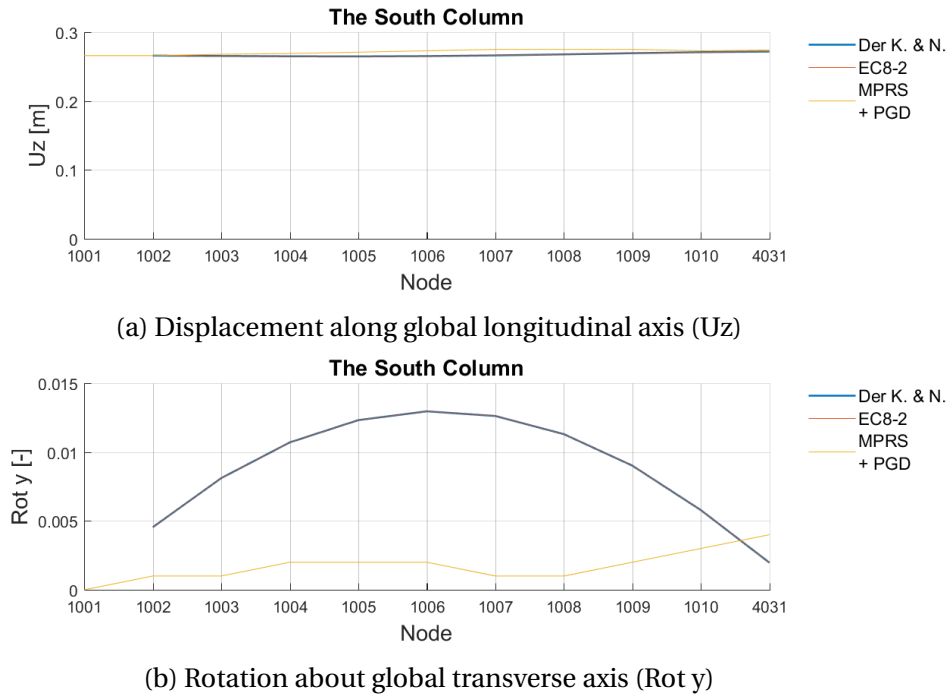
Figure 8.1: Comparison of the response in the South Column of the Simple Bridge

(a) Displacement along global longitudinal axis (Uz)

(b) Rotation about global transverse axis (Rot y)
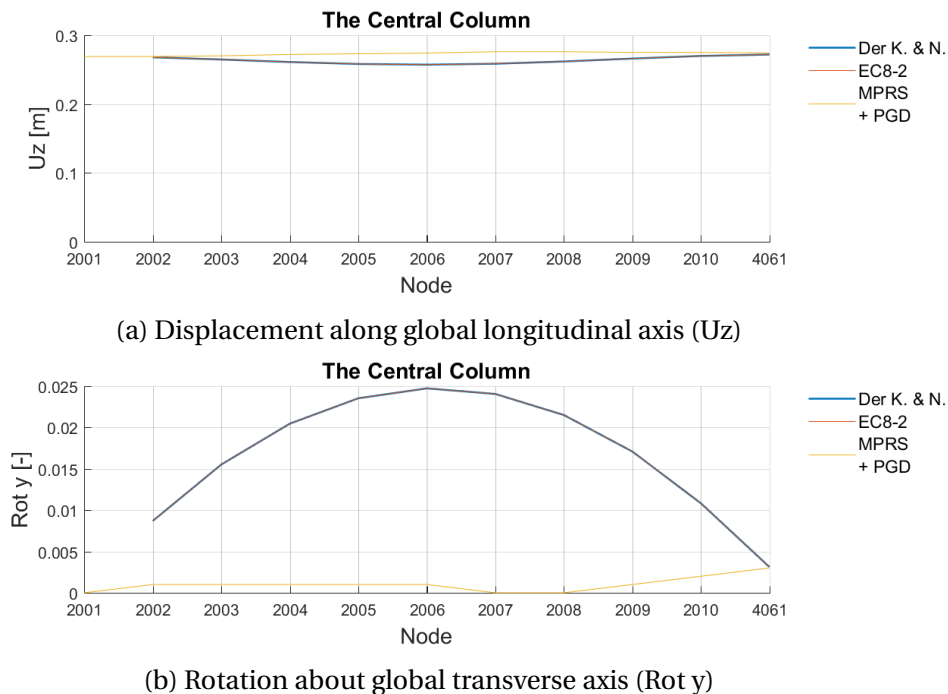
Figure 8.2: Comparison of the response in the Central Column of the Simple Bridge
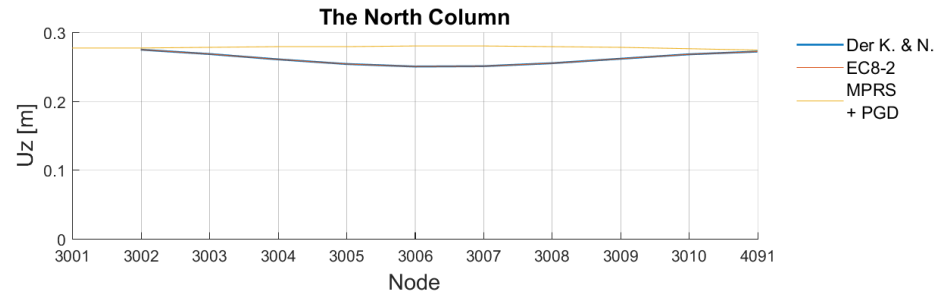
(a) Displacement along global longitudinal axis (Uz)
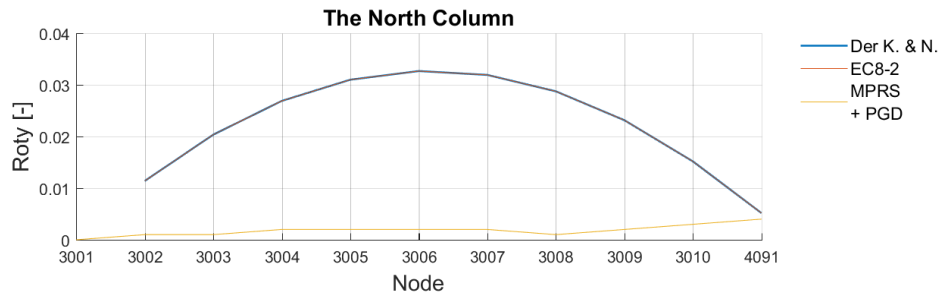
(b) Rotation about global transverse axis (Rot y)

Figure 8.3: Comparison of the response in the North Column of the Simple Bridge
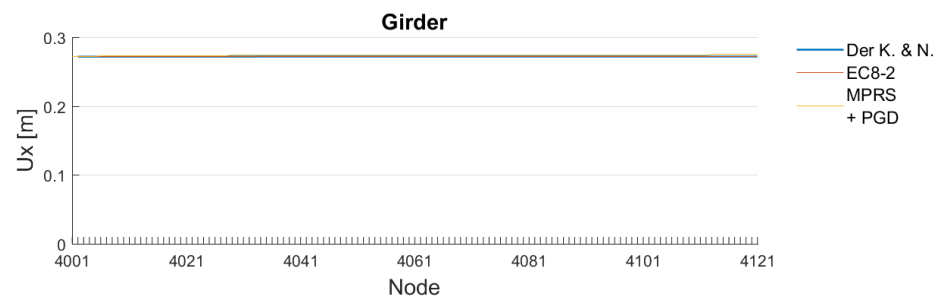
(a) Displacement along global longitudinal axis
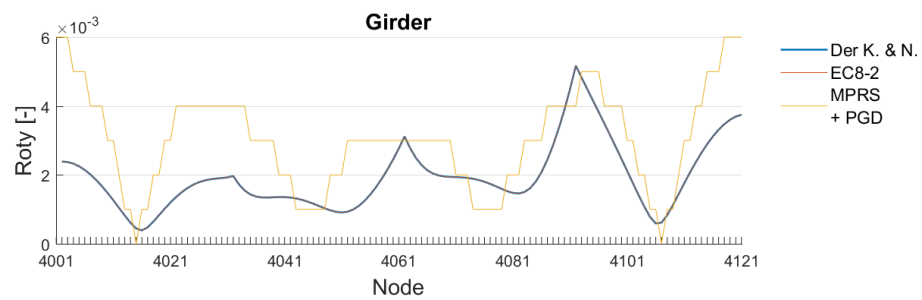
(b) Rotation about global transverse axis (Rot y)

Figure 8.4: Comparison of the response in the girder of the Simple Bridge

8.2   Justification of the MPRS-Function in ANSYS
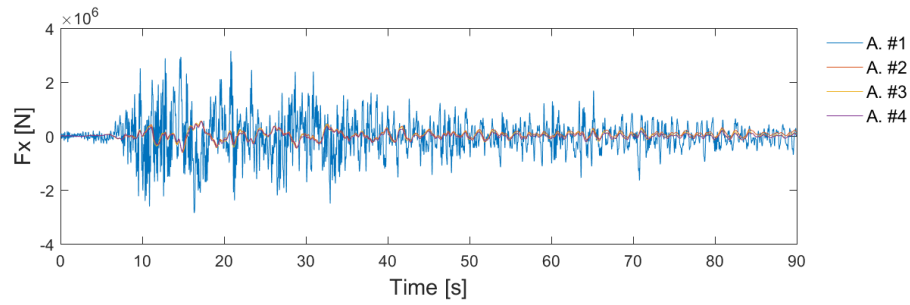
Figure 8.5: Force history from separate THAs with longitudinal excitation
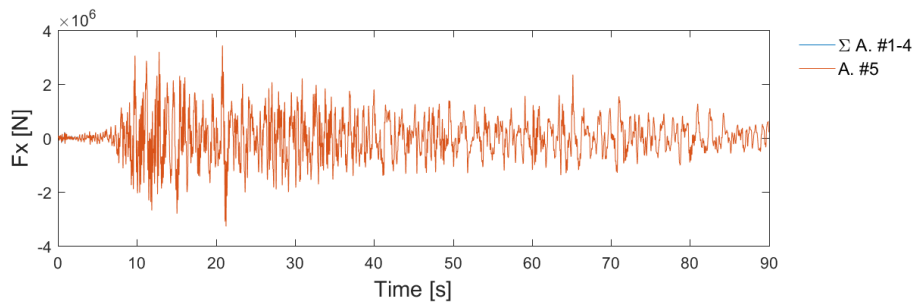
Figure 8.6: Sum of four THAs versus one THA with four longitudinal input motions
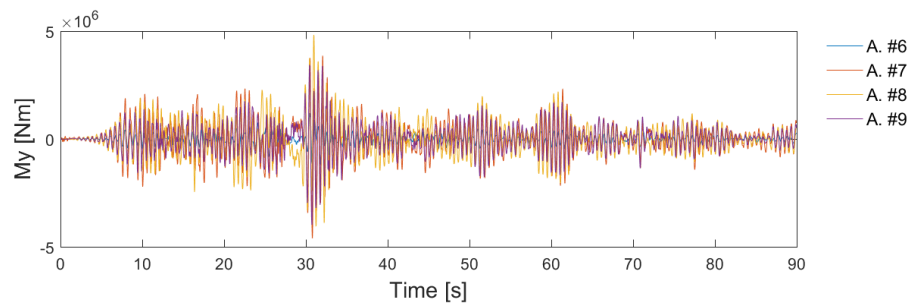
Figure 8.7: Moment history from separate THAs with vertical excitation
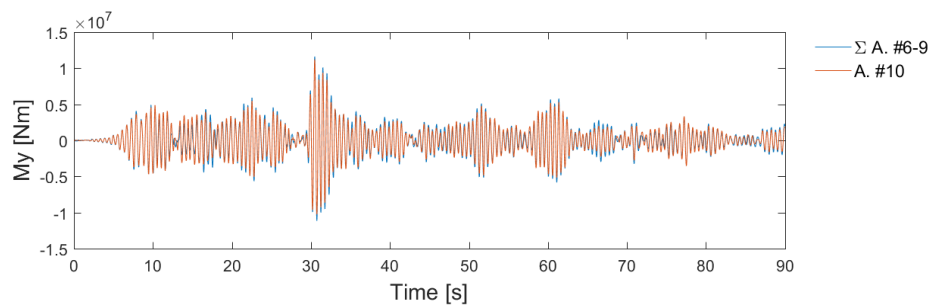
Figure 8.8: Sum of four THAs versus one THA with four vertical input motions

8.3 Mode Superposition in MPRS

8.3.1 Results from the Simple Bridge
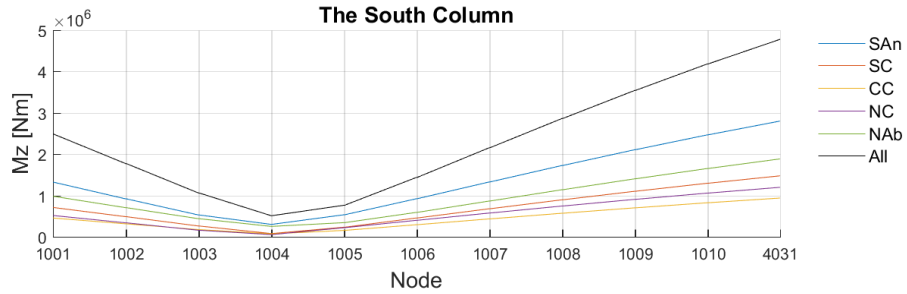
Figure 8.9: Moment about global longitudinal axis (Mz)
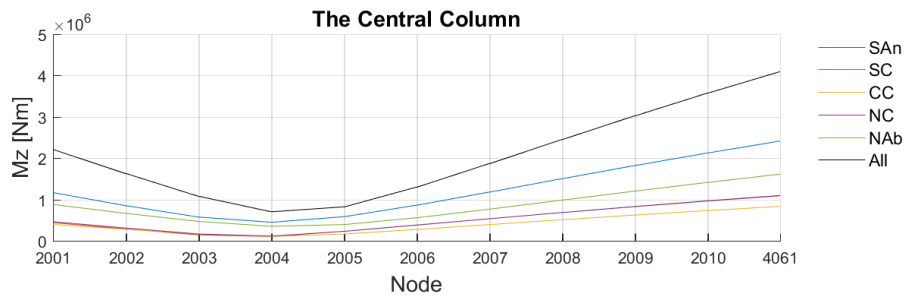
Figure 8.10: Moment about global longitudinal axis (Mz)
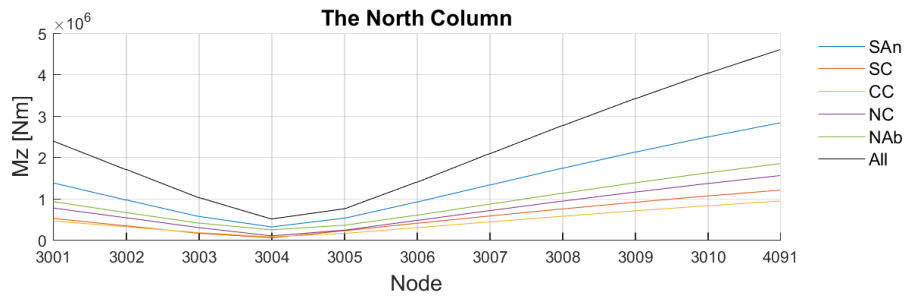
Figure 8.11: Moment about global longitudinal axis (Mz)
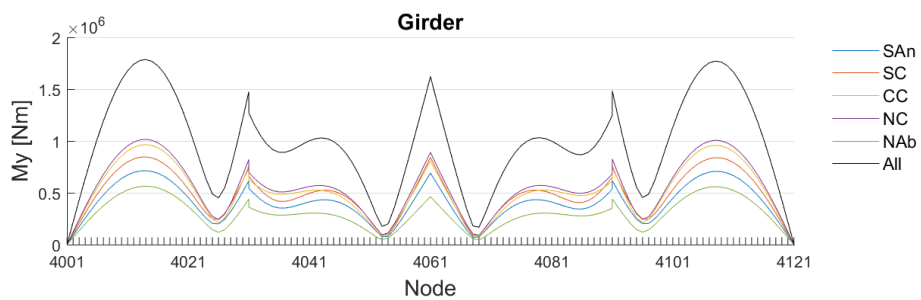
Figure 8.12: Moment about global transverse axis (My)

8.3.2 Results from the Chacao Bridge
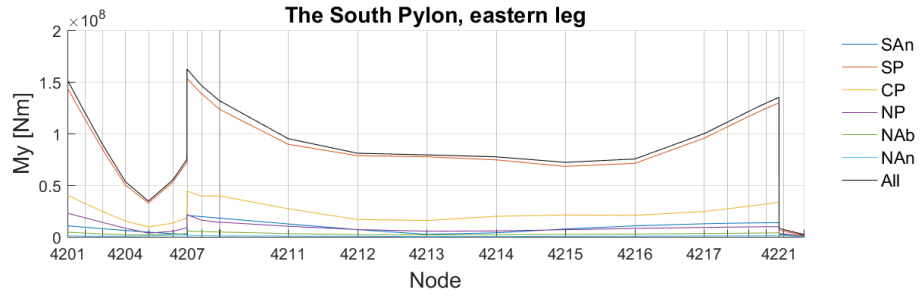
Figure 8.13: Moment about global longitudinal axis (My)
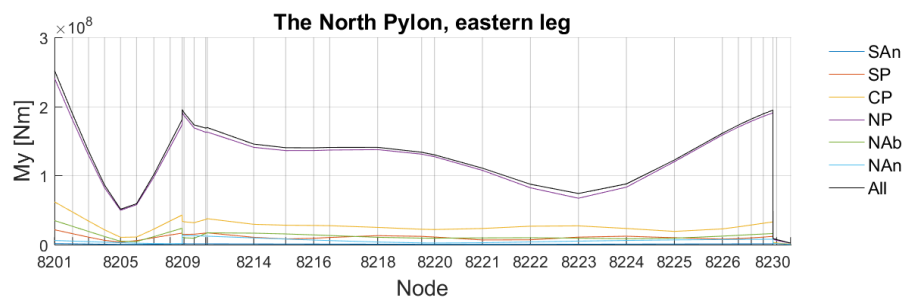
Figure 8.14: Moment about global longitudinal axis (My)
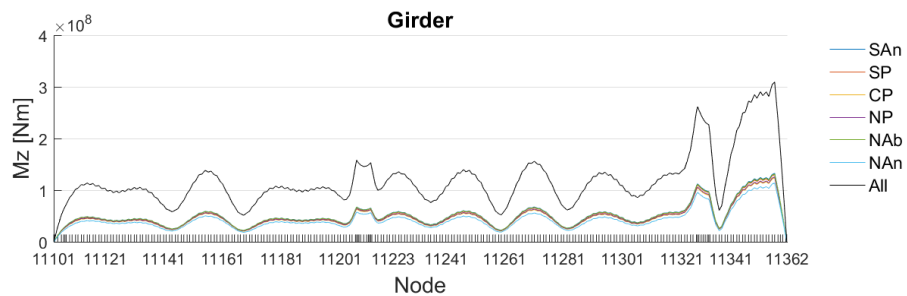
Figure 8.15: Moment about global transverse axis (Mz)

Chapter 9

Discussion of Further Investigation

9.1 Der Kiureghian and Neuenhofer's Method

Even though the forces and moments calculated by Der Kiureghian and Neuenhofer's method were far off, the displacements and rotations depicted in Figure 8.1-8.4 are believed to be correct. However, the static solution has major impact on the displacements. Because the PGDs are close to identical for all spectra, the results are dominated by rigid-body motion. Consequently, the difference of the methods may have appeared greater if only the dynamic contributions were included. The dominance of rigid-body motion is especially evident in Figure 8.4. The rotations are so small such that the MPRS solution appears discontinuous because each step is equal to the level of accuracy in ANSYS.

Because the forces were incorrect and the displacements are believed to be correct, $\mathbf{F} = \mathbf{Kz}$ cannot be used to extract forces. A possible reason is that $\mathbf{z}$ only takes positive values. This means that in order to extract forces, the transfer function, $\mathbf{q}$, must be changed such that it relates displacements/rotations to forces/moments. However, due to lack of time and knowledge, this was not investigated further and should be the focus of future work.

One may observe that EC8-2's simplified version coincide perfectly with Der Kiureghian and Neuenhofer's full method in Figure 8.1-8.4. Therefore, the neglecting of the correlation between the pseudo-static and dynamic response in EC8-2 can be justified. Furthermore, in estimation of PSD, the factor adjusting for low-frequent content is excessive for the Simple Bridge. For larger structures with lower natural frequencies, the simplifications in EC8-2 are likely to be of greater impact.

9.2   Justification of the MPRS-Function in ANSYS

Figure 8.5 presents force histories from each longitudinal single-input THA, while Figure 8.6 displays the summed response of analysis number 1-4. The figures suggest that the four single-input THAs are equivalent to exciting all four support DOFs simultaneously. Note that response is obtained from a longitudinal DOF located in the transition between the South Column and the girder of the Simple Bridge.

Similarly, Figure 8.7 and 8.8 display the moment history in a node located in the transition between the Central Column and the girder. Again, the summed response is close to identical with the results obtained from exciting all supports simultaneously. However, because the sum generally provides a slightly greater response, there is reason to believe that not all permanent displacements have been removed during the Butterworth filtering. Consequently, forces due to the displacements may have been accounted for multiple times, such that the total response appears greater.

Due to vast similarities between the two approaches for both longitudinal and vertical loading, a parallel to MPRS can be made. Combining the results from four single-input THAs is comparable to combining the results from four single-input response spectra. The latter is essentially what the MPRS-function in ANSYS does. However, the response of the function is not estimated by sum, it is estimated by the SRSS-rule. The methodology of the MPRS-function is therefore justified; yet, it is not verified.

9.3   Mode Superposition in MPRS

The results presented in Chapter 8.3 support the theory developed for the MPRS-function. By exciting only one support, other mode shapes are initiated compared to exciting all supports simultaneously. Furthermore, mode shapes initiated by exciting one support is strongly dependent on which support is being excited. The dependence is particularly evident in Figure 8.13 and 8.14 for the Chacao Bridge. The figures display that the spectrum from the South Pylon dominates the response in the South Pylon, correspondingly, the spectrum from the North Pylon dominates the response in the North Pylon. When the SRSS-rule is applied on values where one value is remarkably greater, the outcome is approximately equal to the greatest value. E.g. $\sqrt{1^2 + 1^2 + 1^2 + 4^2} \approx 4$.

The Chacao Bridge is a rather soft construction with two long spans. This give rise to local modes, meaning that certain mode shapes more or less are restricted to movement of one component. However, components spanning multiple supports are excited by several spectra. The outcome is that multi-supported components receive significant contributions from more than one spectrum. Due to the MPRS-function's use of the SRSS-rule, this may result in an overestimated response. The reason is that when similar values are combined by the SRSS-rule, the outcome is significantly larger than any of the values. E.g. $\sqrt{2^2 + 2^2 + 2^2 + 2^2} >> 2$. This effect was observed for the girder of the Chacao Bridge in Chapter 6.3.4, and confirmed in Figure 8.15. The figure shows that each response spectrum provides significant contributions, and the combined effect is greatly amplified.

The effect of change in dominating mode shapes appear differently for shorter and stiffer bridges. Movement in one component affects adjacent components. As a consequence, each response spectrum initiates global modes and generate significant effects in multiple components. This effect was observed on the Simple Bridge, which is much stiffer and shorter than the Chacao Bridge. Figure 8.9-8.12 show that the columns and girder are no longer dominated by a single spectrum. Each spectrum contributes with a significant response, and the final response is amplified by the SRSS-rule.

The results indicate that the MPRS-function in ANSYS is sensitive to the configuration and stiffness of a structure. The function is believed to overestimate the response for stiff and short structures. However, if supports are able to move independently, the function may provide results in good agreement with results from THA.

Chapter 10

Conclusion

In this thesis, various methods for estimation of structural response due to asynchronous seismic ground motion have been tested and compared. Two finite element models were developed in ANSYS: 1) the Chacao Bridge designed by Aas-Jakobsen for the Chacao-project in Chile, and 2) a four span beam bridge referred to as the Simple Bridge. Five methods were tested based on recommendations in Eurocode 8, part 2 for bridges (EC8-2): time history analysis (THA), single- and multi-point response spectrum analysis (RSA), the simplified method in chapter 3.3 of EC8-2, and Der Kiureghian and Neuenhofer's response spectrum method.

THAs and RSAs are fundamentally different. While THA is deterministic, computationally expensive, and is carried out in the time domain, RSA is statistically based, is fast, and is carried out in the frequency domain. Due to its deterministic approach, THA was considered as the most accurate method and was used as reference for comparison of the results. However, the accelerograms used in THAs for the Simple Bridge were adopted from the Chacao Bridge. Using the same seismic input on a bridge 1/20th of the length induced too dominating static forces from the permanent displacements. Consequently, the basis for comparison of the dynamic response was lost. The effects from permanent displacements were attempted removed using the Butterworth filter; however, effects are still believed to be present. The THAs conducted on the Simple Bridge are therefore considered invalid as reference.

The simplified method from EC8-2 is supposed to be quick, simple and easy to implement. However, the adapted method in this thesis is more complex due to custom made

response spectra. The method turned out to be the most conservative of the four methods implemented on the Chacao Bridge. Mean deviations ranged from 10-30%, but extreme values with 105% deviation were observed. The pseudo-static displacements were of low or no impact for both bridges. Consequently, the analysis failed to account for the varying seismic characteristics. In addition, the simplified method calculates the inertia effect from a spectrum corresponding to the poorest soil conditions along the bridge. A significant difference in soil conditions will therefore generate too conservative results, which is unfavorable in design situations.

The SPRS method follows the same methodology as the simplified method in regards to the response spectrum analysis. Results from the two methods showed good agreement, particularly for the Simple Bridge. However, the SPRS-function in ANSYS in limited to one input spectrum per analysis. Therefore, in order to account for local soil conditions, the analysis was repeated with site-specific spectra for all supports. Compared to THA, SPRS deviated ±20% for the Chacao Bridge. Repeated shifts of over- and underestimation of the response is undesirable for design situations. The shifts are believed to occur due to simplification of the response spectra by use of the recursive Douglas-Peucker polyline simplification method. This process reduced the number of spectral values from 1500 to less than 100. Since 1500 values were necessary to represent damping in all included frequencies, the limitation of 100 values is considered as a major weakness in the SPRS-function provided by ANSYS.

The MPRS-function developed by ANSYS is by far the least time consuming method tested in this research. Compared to the SPRS method on the Chacao Bridge, run time was reduced from 6 hours to 20 minutes. However, the results from the two bridge models led to different observations. The MPRS-function generated the lowest response for the Chacao Bridge, while it generated the largest response of the RSAs for the Simple Bridge. Therefore, the full MPRS analysis was divided into separate analyses, each with only one input response spectrum at one support. The results from the Chacao Bridge indicated that the mode shapes initiated by exciting only one support was strongly dependent on which support was being excited. The long and soft construction gave rise to "local modes". In other words, exciting one support initiated modes restricted to movement of one component. On the other hand, exciting only one support in the shorter and stiffer Simple Bridge initiated "global modes", which generated significant effects in all components. Therefore, there is

reason to believe that the MPRS-function is sensitive to the configuration and stiffness of the structure. In order for the MPRS-function to provide close and correlated results compared to THA, supports must be able to move independently.

Der Kiureghian and Neuenhofer's multi-point response spectrum method is the most sophisticated method discussed in this paper. It has yet to be implemented in any commercial finite element software, and was implemented manually in MatLab for the Simple Bridge. Due to its complexity in MatLab implementation and limited time, the authors were unable to produce forces by this method. However, displacements and rotations were extracted for both the full and EC8-2's simplified version. Both versions presented great similarities to the peak ground displacements; consequently, EC8-2's simplifications are justified. Because displacements and rotations could not be directly related to forces and moments in the MatLab implementation, it is recommended that the transfer functions, which relate the forces/moments to the displacements/rotations, are studies in future thesis research.

Bibliography

Aas-Jakobsen (2014). Chacao bridge. [13.05.17]. Available from: `http://www.aaj.no/english/nyheter/nyheter.html`.

Aas-Jakobsen, SYSTRA, E&C, H., and OAS (2016a). 2d site response analyses. *Report CHB-SAJ-DGN-DOC-GB-0222*.

Aas-Jakobsen, SYSTRA, E&C, H., and OAS (2016b). Global analysis, dynamic seismic analyses results. *Report CHB-SAJ-DGN-DOC-GB-0106*.

Aas-Jakobsen, SYSTRA, E&C, H., and OAS (2016c). Global analysis, static analyses results. *Report CHB-SAJ-DGN-DOC-GB-0103*.

Aas-Jakobsen, SYSTRA, E&C, H., and OAS (2016d). Probabilistic seismic hazard assessment for the chacao channel bridge design (chile). *Report CHB-SAJ-DGN-DOC-GB-0202*.

Aas-Jakobsen, SYSTRA, E&C, H., and OAS (2016e). Rock time histories for seismic analyses – maximum probable earthquake. *Report CHB-SAJ-DGN-DOC-GB-0220*.

ANSYS inc. (2016). Ansys mechanical apdl 17.2 [computer software]. [31.01.17] Available from: `http://www.ansys.com/`.

ANSYS inc. (2017a). 14.3.4. mode-superposition analysis. *ANSYS Help Viewer*.

ANSYS inc. (2017b). 15.7. spectrum analysis. *ANSYS Help Viewer*.

ANSYS inc. (2017c). Ansys help, 13.188. beam188 - 3-d 2-node beam. *ANSYS Help Viewer*.

ANSYS inc. (2017d). Ansys help, 6.1. understanding spectrum analysis. *ANSYS Help Viewer*.

ANSYS inc. (2017e). Matrix27 element description. *ANSYS Help Viewer*.

Bell, K. (2012). *Matrisestatikk*. Tapir akademisk forlag.

Berrah, M. and Kausel, E. (1992). Response spectrum analysis of structures subjected to spatially varying motions. *Earthquake Engineering and Structural Dynamics*, 21(6):461–470.

Chopra, A. K. (2011). *Dynamics of Structures - Theory and Applications to Earthquake Engineering*. Pearson Prentice Hall, Upper Saddle River, N.J., 4th edition.

Clough, R. and Penzien, J. (1993). *Dynamics of Structures*. Civil Engineering Series. McGraw-Hill, New York, NY.

Dassault Systèmes (2017). Abaqus [computer software]. [20.05.17] Available from: `https://www.3ds.com/products-services/simulia/products/abaqus/abaquscae/`.

Der Kiureghian, A. (1996). A coherency model for spatially varying ground motions. *Earthquake Engineering and Structural Dynamics*, 25:99–111.

Der Kiureghian, A. and Neuenhofer, A. (1992). Response spectrum method for multi-support seismic excitations. *Earthquake Engineering and Structural Dynamics*, 21:713–740.

Douglas, D. H. and Peuker, T. K. (2011). *Algorithms for the Reduction of the Number of Points Required to Represent a Digitized Line or its Caricature*. John Wiley & Sons, Ltd, Chichester, UK.

Holden, H. (2017). Superposisjonsprinsippet. [18.05.17]. Available from: `https://snl.no/superposisjonsprinsippet`.

Incorporated Bentley Systems (2016). Rm bridge advanced connect edition10.1010/.005./022016 [computer software]. Available from: `https://www.bentley.com/en/products/product-line/bridge-analysis-software/rm-bridge`.

Luco, J. E. and Wong, H. L. (1986). Response of a rigid foundation to spatially random ground motion. *Earthquake Engineering and Structural Dynamics*, 14:891–908.

Lysmer, J., T.-R. M. T. F. V. S. and Ostadan, F. (1981). Sassi - a system for analysis of soil-structure interaction. *Report UCB/GT 81-02*, Univ. of California, Berkeley, USA.

Mathisen, K. M. (2016a). Lecture 7: Solution of the dynamic equilibrium equations by explicit direct integration. From: TKT4197.

Mathisen, K. M. (2016b). Lecture 8: Solution of the dynamic equilibrium equations by implicit direct integration. From: TKT4197.

MathWorks (2017a). Butterworth filter design. [01.06.17]. Available from: `https://se.mathworks.com/help/signal/ref/butter.html`.

MathWorks (2017b). Design high-pass filters using matlab. [01.06.17]. Available from: `https://se.mathworks.com/discovery/high-pass-filter.html`.

MathWorks (2017). Matlab 2017a [computer software]. [23.02.17] Available from: `https://www.mathworks.com/products/matlab.html`.

McKenna, F., Fenves, G., Scott, M., et al. (2000). Open system for earthquake engineering simulation. *University of California, Berkeley, CA.*

Nakamura, Y., Der Kiureghian, A., and Liu, D. (1993). Multiple-support response spectrum analysis of the golden gate bridge. *Report no. UCB/EERC-93/05*, Earthquake Engineering Research Center, University of California at Berkeley, Berkeley.

Newland, D. (2012). *An Introduction to Random Vibrations, Spectral & Wavelet Analysis: Third Edition.* Dover Civil and Mechanical Engineering. Dover Publications.

Nuti, C., Biondi, S., and Vanzi, I. (2011). Design actions for continuous deck bridges considering non-synchronous earthquake motion. *5th International Conference on Earthquake Geotechnical Engineering*, Santiago, Chile.

Priestley, M., Seible, F., and Calvi, G. (1996). *Seismic Design and Retrofit of Bridges.* A Wiley interscience publication. Wiley.

Rönnquist, A. (2016). Lecture 26/27: Step by step time integration. From: TKT4201.

Salmon, M. W., Short, S. A., and Kennedy, R. P. (1992). Strong motion duration and earthquake magnitude relationships. Master's thesis, University of California Livermore.

Sextos, A. and Kappos, A. (2005). Evaluation of the new eurocode 8-part 2 provisions regarding asynchronous excitation of irregular bridges. *Proceedings of the 4th European Workshop on the Seismic Behavior of Irregular and Complex Structures.*

Sextos, A. and Kappos, A. (2009). Evaluation of seismic response of bridges under asynchronous excitation and comparisons with eurocode 8-2 provisions. *Bulletin of Earthquake Engineering,* 7:519–545.

Standard Norge (2003). Eurocode 1: Actions on structures - part 1: Traffic loads on bridges. *Norsk Standard NS-EN 1991-1-1:2002+NA:2008.*

Standard Norge (2004). Eurocode 8: Design of structures for earthquake resistance - part 1: General rules, seismic actions and rules for buildings. *Norsk Standard NS-EN 1998-1:2004+A1:2013+NA:2014.*

Standard Norge (2005). Eurocode 8: Design of structures for earthquake resistance - part 2: Bridges. *Norsk Standard NS-EN 1998-2:2005+A1:2009+A2:2011+NA:2014.*

Todorovska, M. I., Trifunac, M. D., Ding, H., and Orbovic, N. (2015). Coherency of dispersed synthetic earthquake ground motion at small separation distances: Dependence on site conditions. *Soil Dynamics and Earthquake Engineering,* 79:253–264.

Wikipedia (2017). Discrete-time fourier transform. [20.03.17]. Available from: `https://en.wikipedia.org/wiki/Discrete-time_Fourier_transform`.

Yamamura, N. and Tanaka, H. (1990). Response analysis of flexible mdf systems for multiple-support seismic excitations. *Earthquake Engineering and Structural Dynamics,* 19(3):345–357.

Ye, J., Zhang, Z., and Liu, X. (2012). A simplified multisupport response spectrum method. *Earthquake Engineering and Engineering Vibration,* 11(2):243–256.

Zerva, A. (2016). *Spatial Variation of Seismic Ground Motions: Modeling and Engineering Applications.* Advances in Engineering Series. CRC Press.

Øverli, J. A. (2016). Formula sheet, concrete structures 1. From: TKT4175.

Appendix A

Results from the Chacao Bridge

The South Pylon, eastern leg

(a) THA

(b) Simplified

(c) SPRS

(d) MPRS

(e) Comparing results
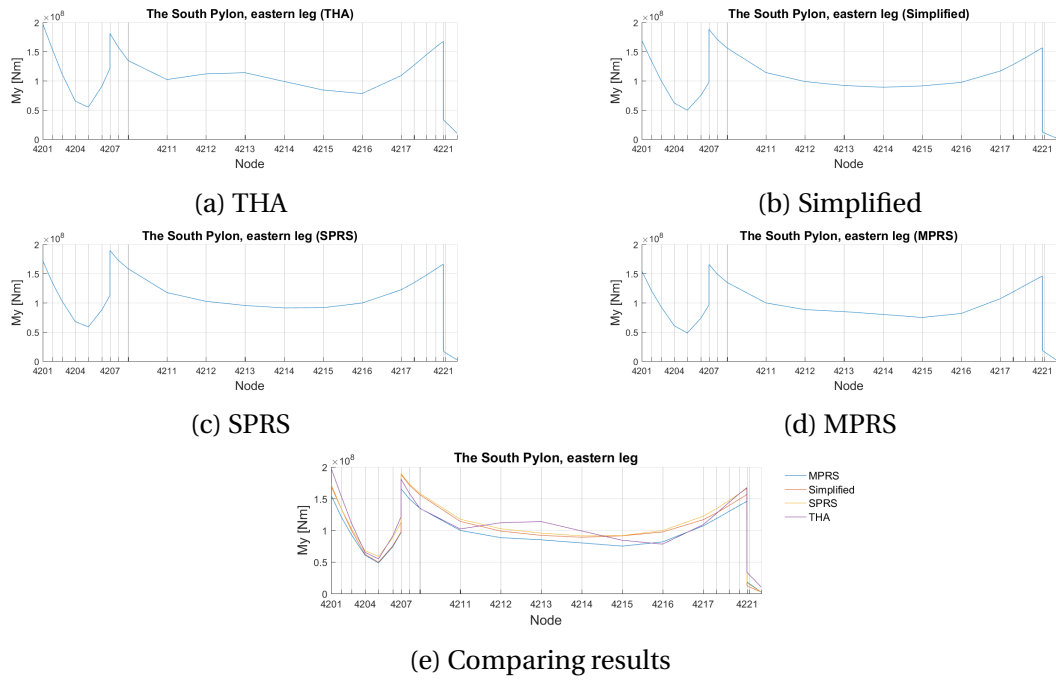
Figure A.1: Moment about global longitudinal axis (My)

(a) THA

(b) Simplified

(c) SPRS

(d) MPRS

(e) Comparing results
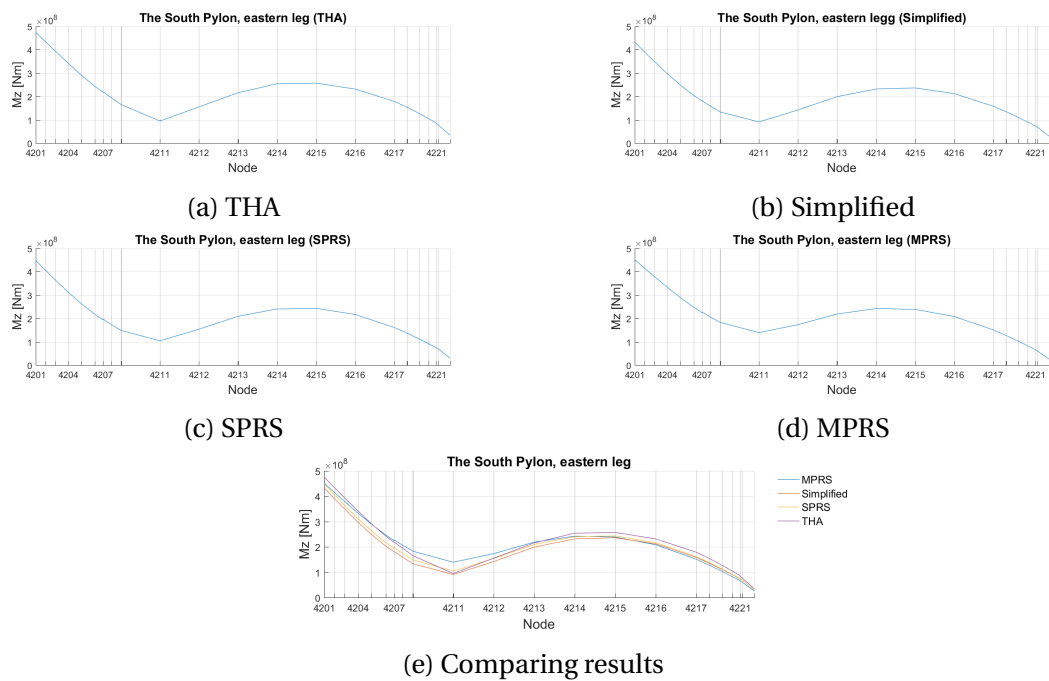
Figure A.2: Moment about global transverse axis (Mz)

The South Pylon, lower crossbeam

(a) THA

(b) Simplified

(c) SPRS

(d) MPRS

(e) Comparing results
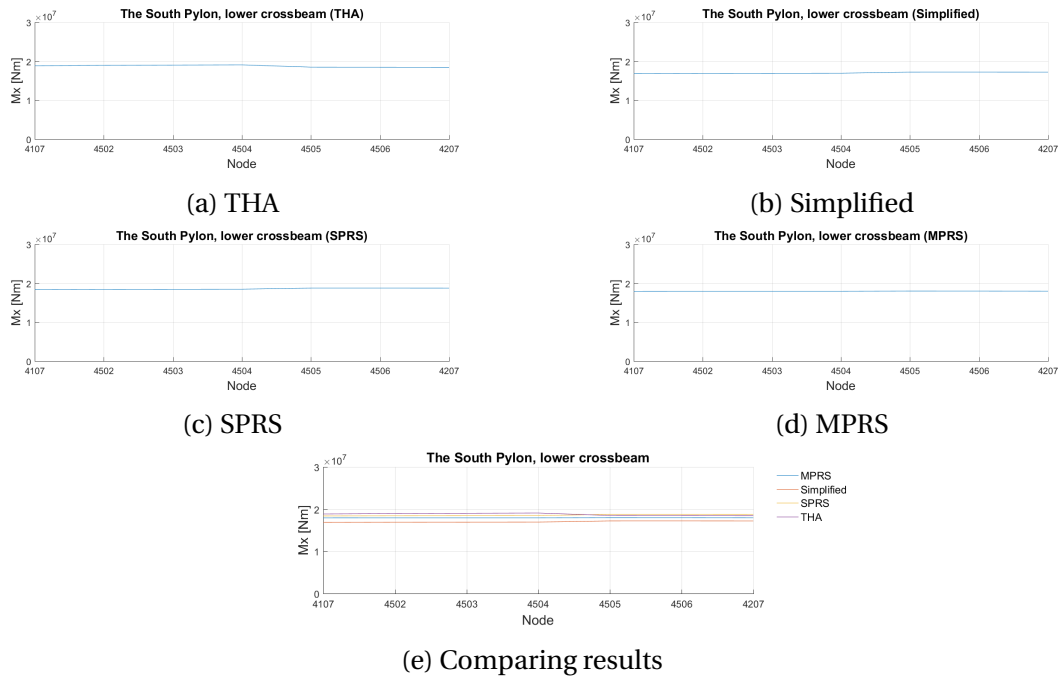
Figure A.3: Moment about global transverse axis (Mx)

(a) THA

(b) Simplified

(c) SPRS

(d) MPRS

(e) Comparing results
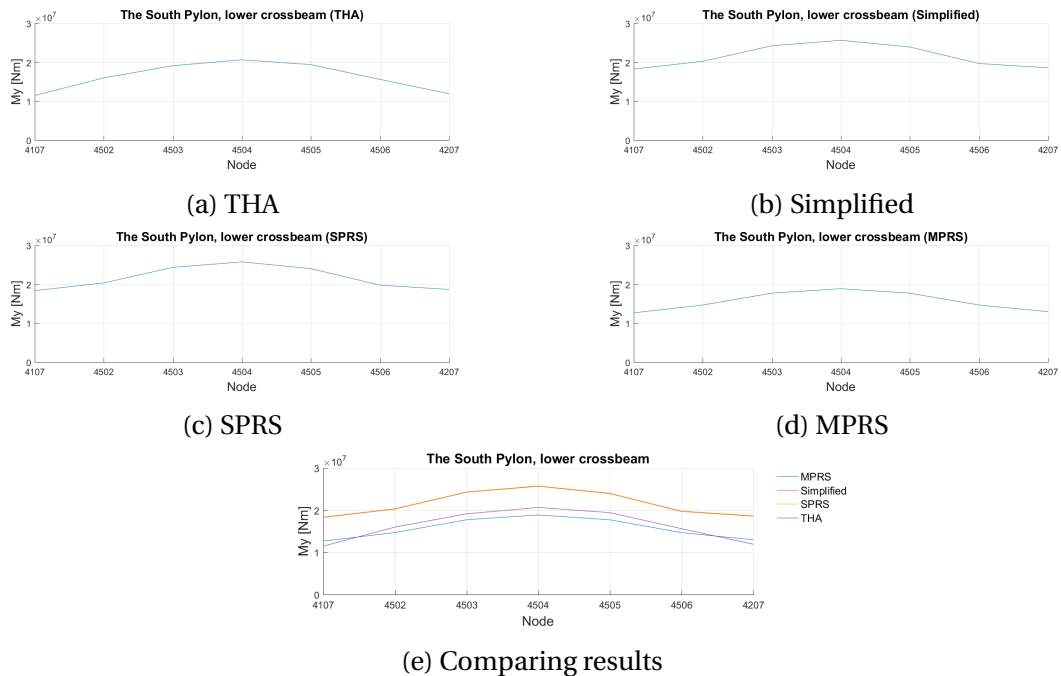
Figure A.4: Moment about global vertical axis (My)

The South Pylon, upper crossbeam

(a) THA

(b) Simplified

(c) SPRS

(d) MPRS

(e) Comparing results
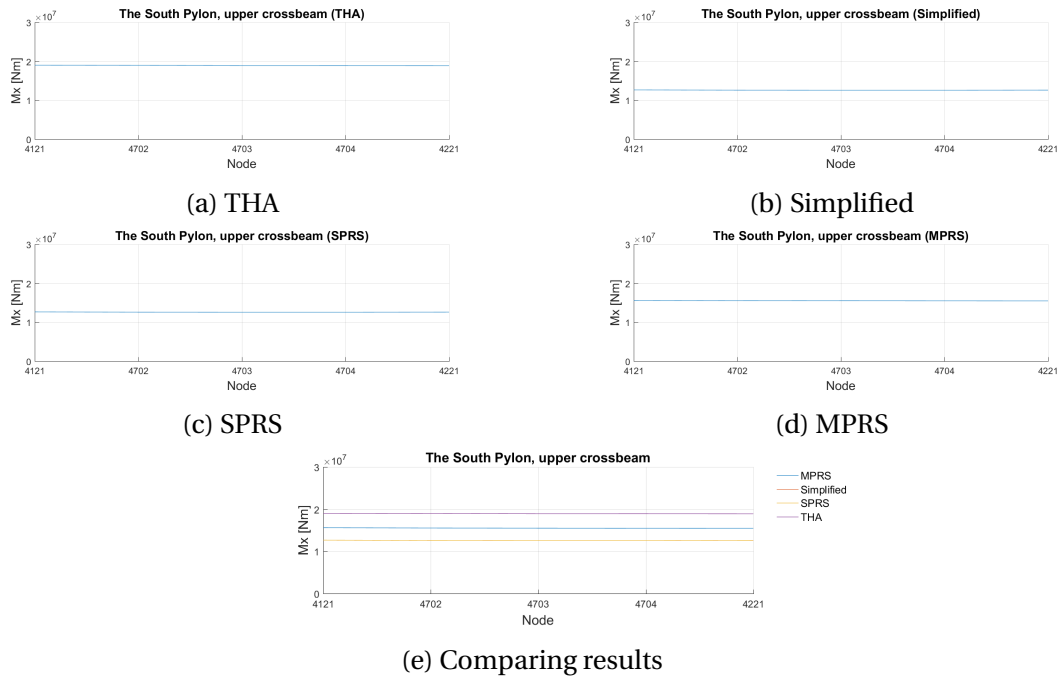
Figure A.5: Moment about global transverse axis (Mx)

(a) THA

(b) Simplified

(c) SPRS

(d) MPRS

(e) Comparing results
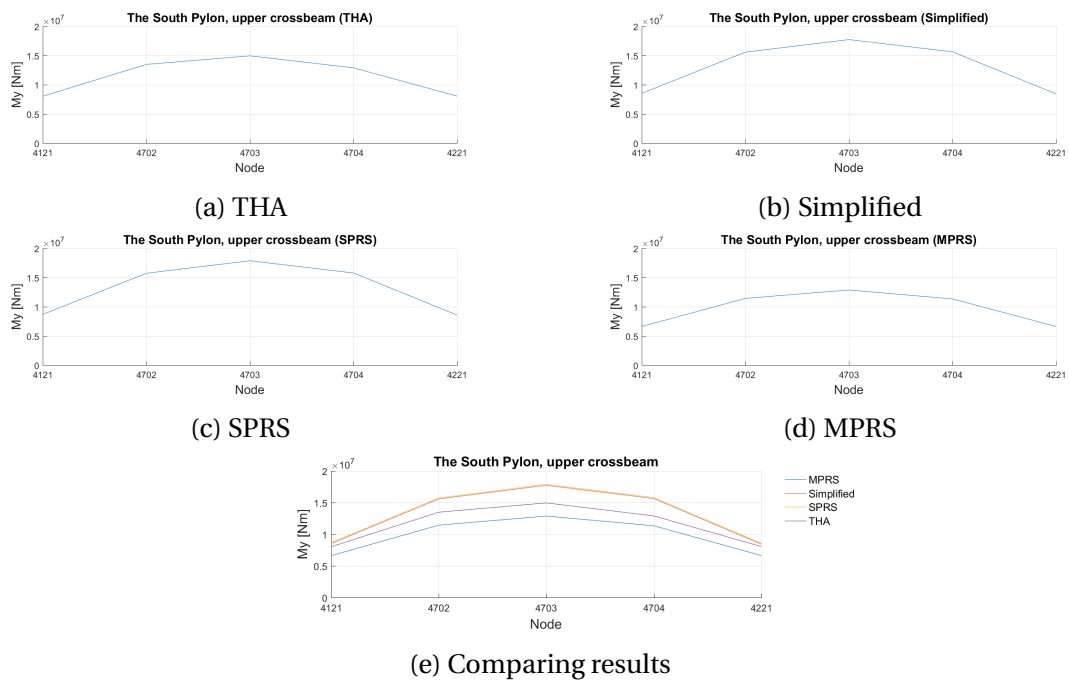
Figure A.6: Moment about global vertical axis (My)

The Central Pylon, lower crossbeam

(a) THA

(b) Simplified

(c) SPRS

(d) MPRS

(e) Comparing results
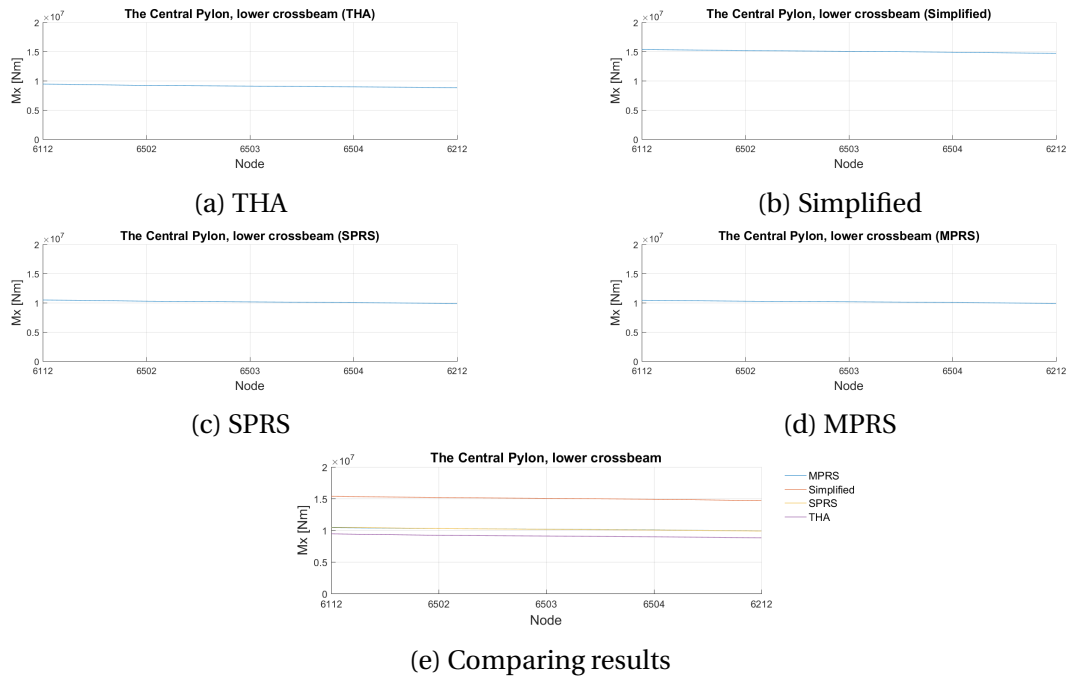
Figure A.7: Moment about global transverse axis (Mx)

(a) THA

(b) Simplified

(c) SPRS

(d) MPRS

(e) Comparing results
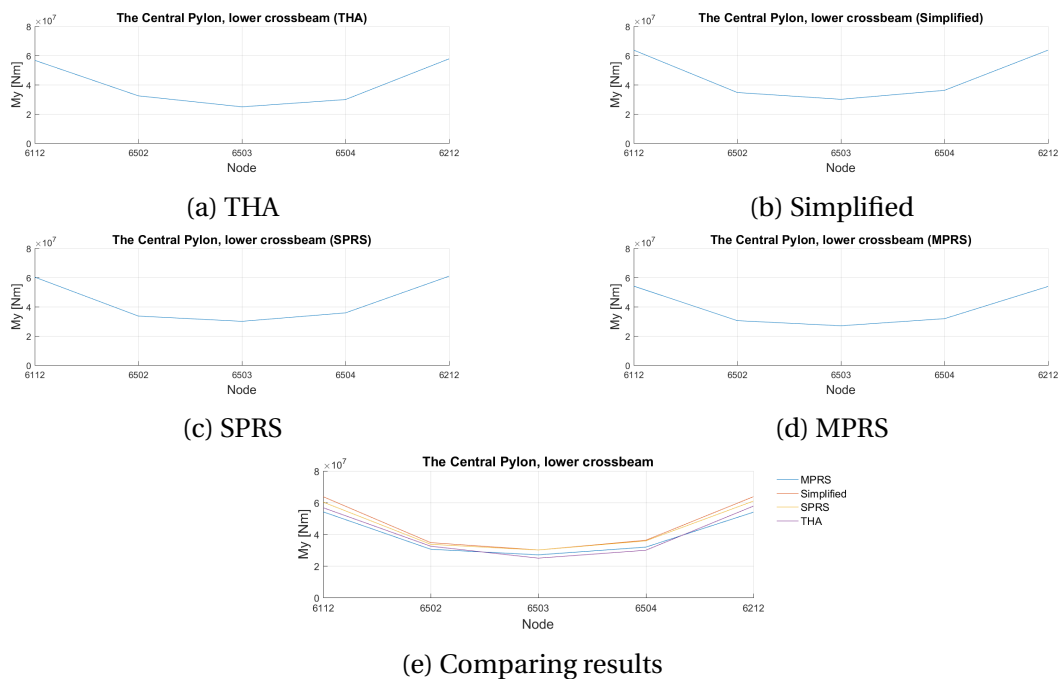
Figure A.8: Moment about global vertical axis (My)

The Central Pylon, upper crossbeam

(a) THA

(b) Simplified

(c) SPRS

(d) MPRS

(e) Comparing results
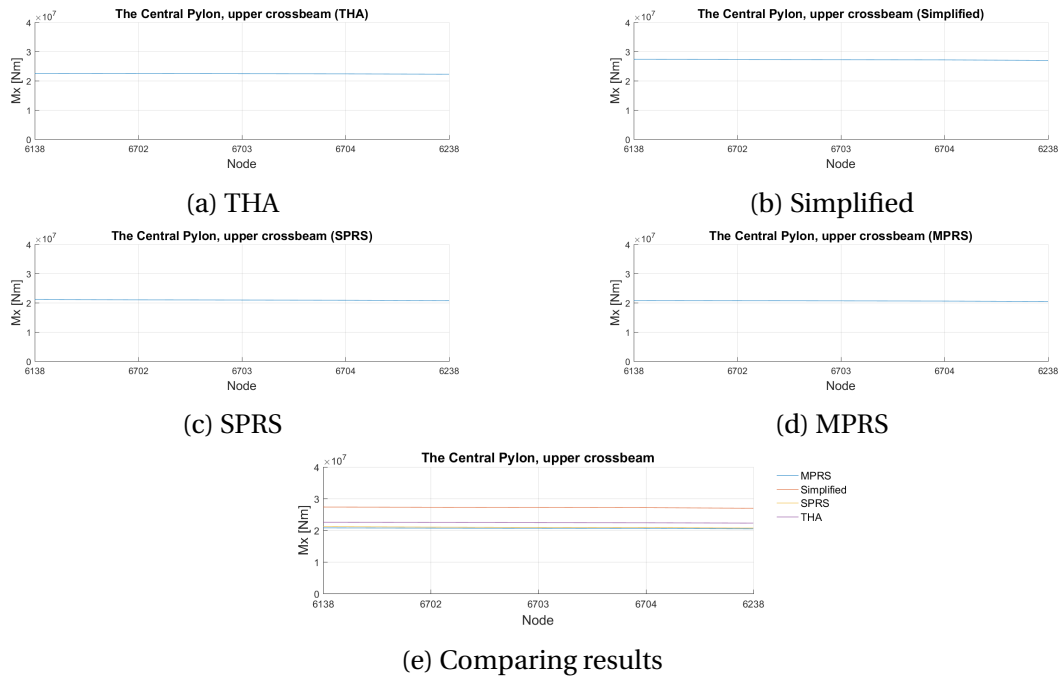
Figure A.9: Moment about global transverse axis (Mx)

(a) THA

(b) Simplified

(c) SPRS

(d) MPRS

(e) Comparing results
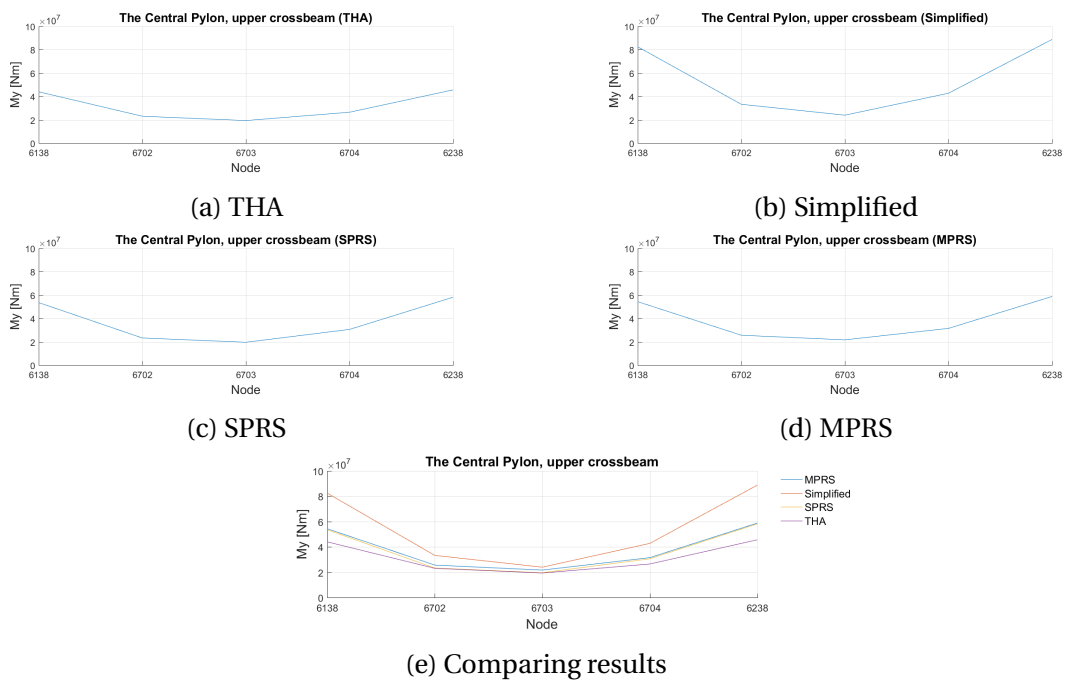
Figure A.10: Moment about global vertical axis (My)

The North Pylon, eastern leg

(a) THA

(b) Simplified

(c) SPRS

(d) MPRS

(e) Comparing results
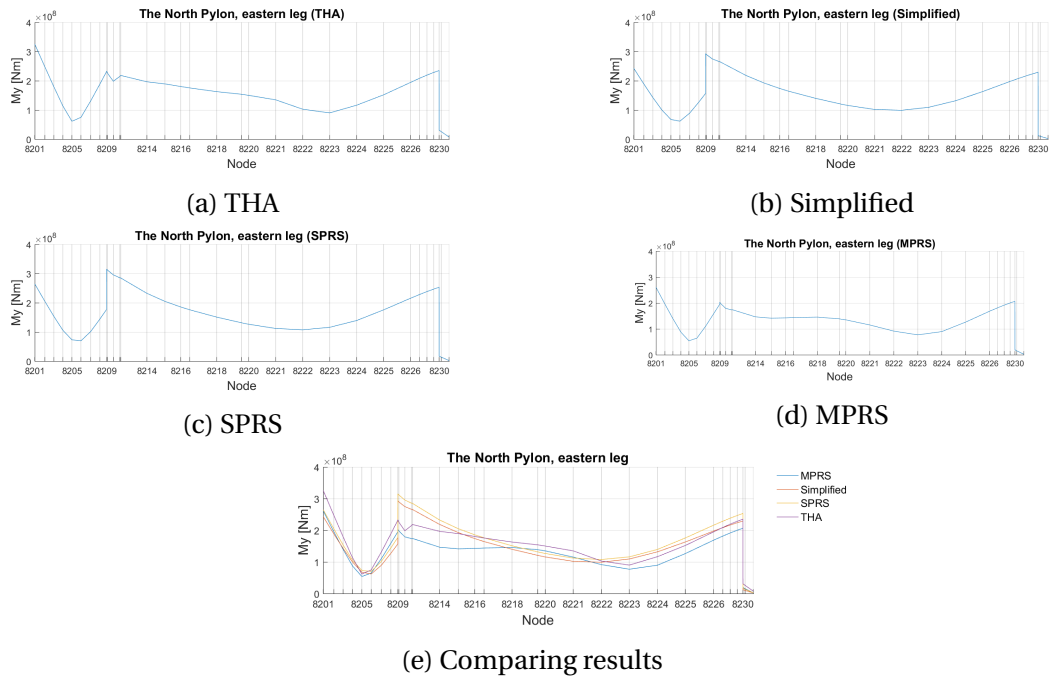
Figure A.11: Moment about global longitudinal axis (My)

(a) THA

(b) Simplified

(c) SPRS

(d) MPRS

(e) Comparing results
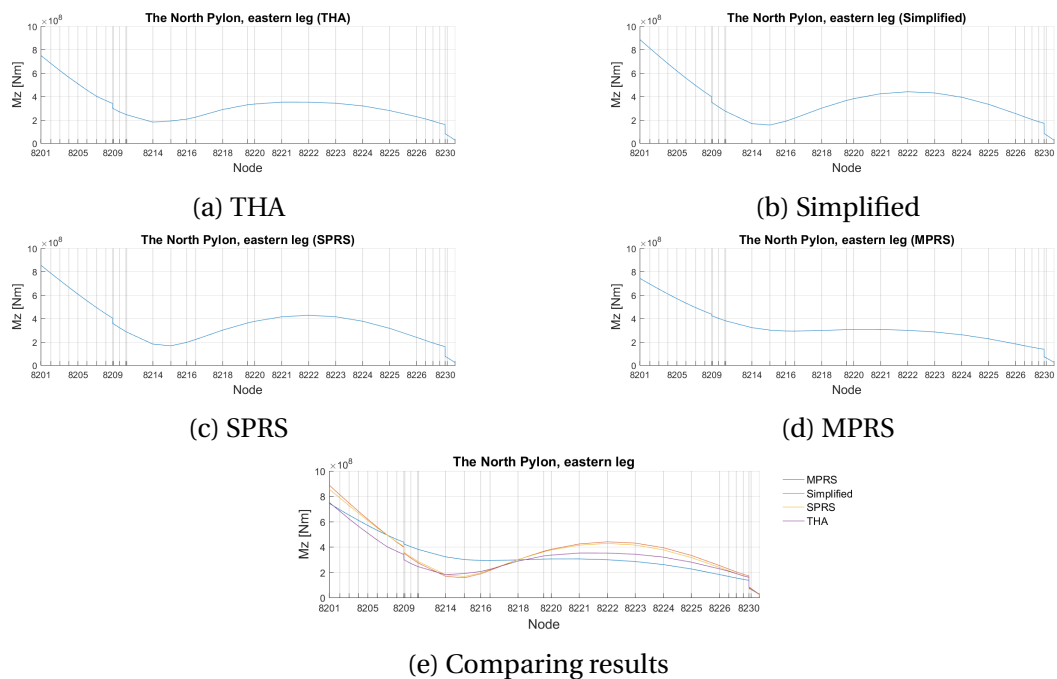
Figure A.12: Moment about global transverse axis (Mz)

The North Pylon, lower crossbeam

(a) THA

(b) Simplified

(c) SPRS

(d) MPRS

(e) Comparing results
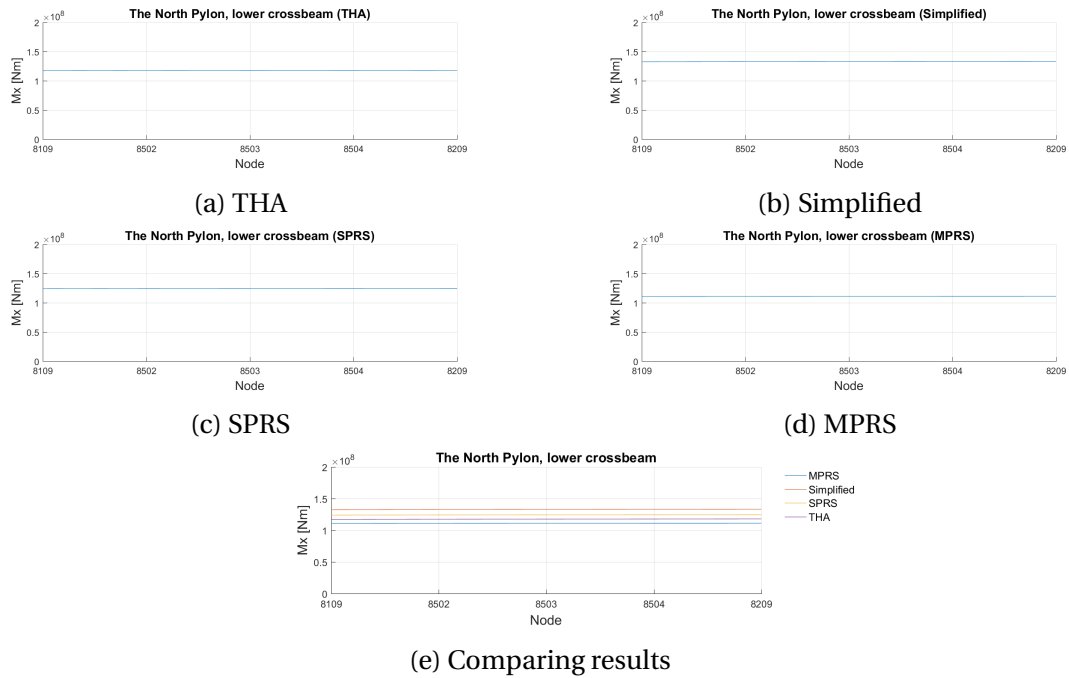
Figure A.13: Moment about global transverse axis (Mx)

(a) THA

(b) Simplified

(c) SPRS

(d) MPRS

(e) Comparing results
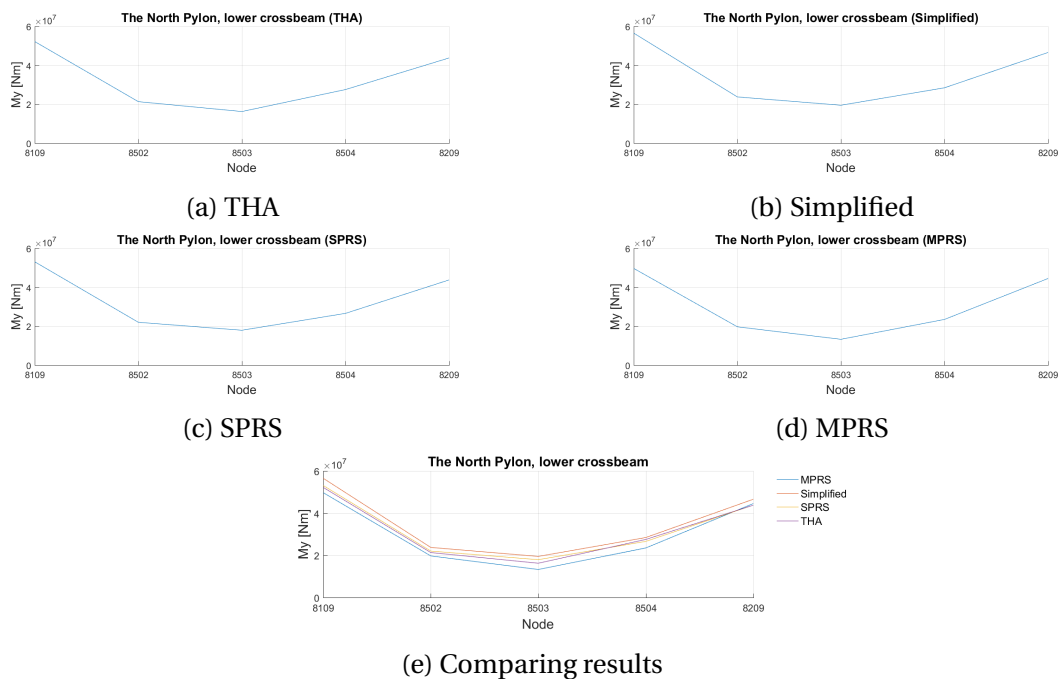
Figure A.14: Moment about global vertical axis (My)

The North Pylon, upper crossbeam

(a) THA

(b) Simplified

(c) SPRS

(d) MPRS

(e) Comparing results
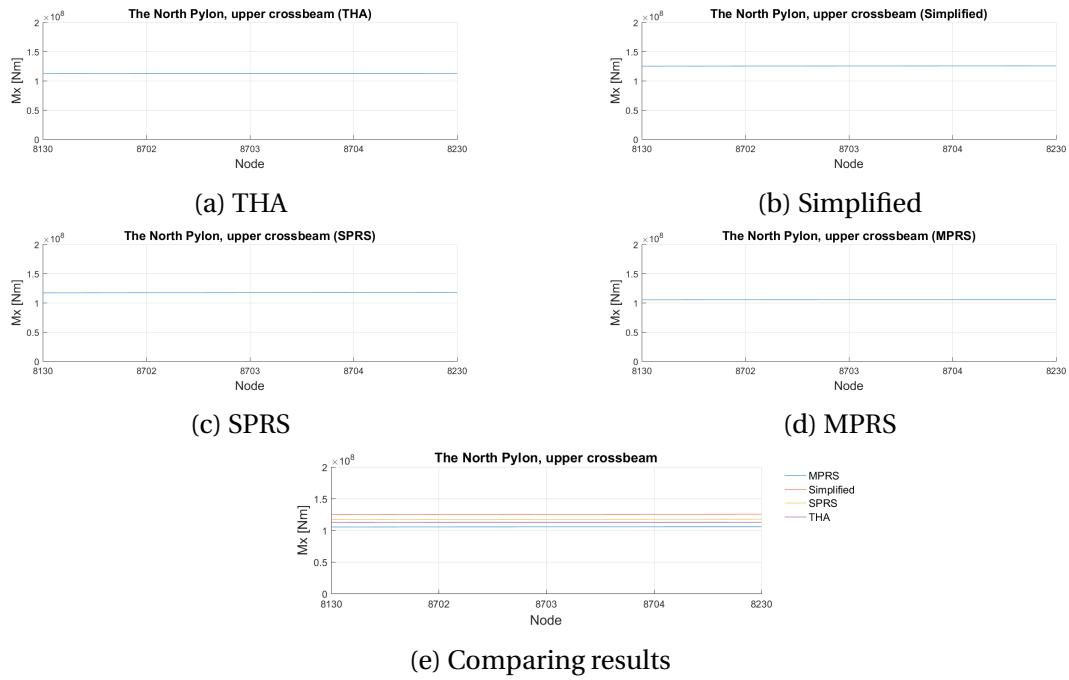
Figure A.15: Moment about global transverse axis (Mx)

(a) THA

(b) Simplified

(c) SPRS

(d) MPRS

(e) Comparing results
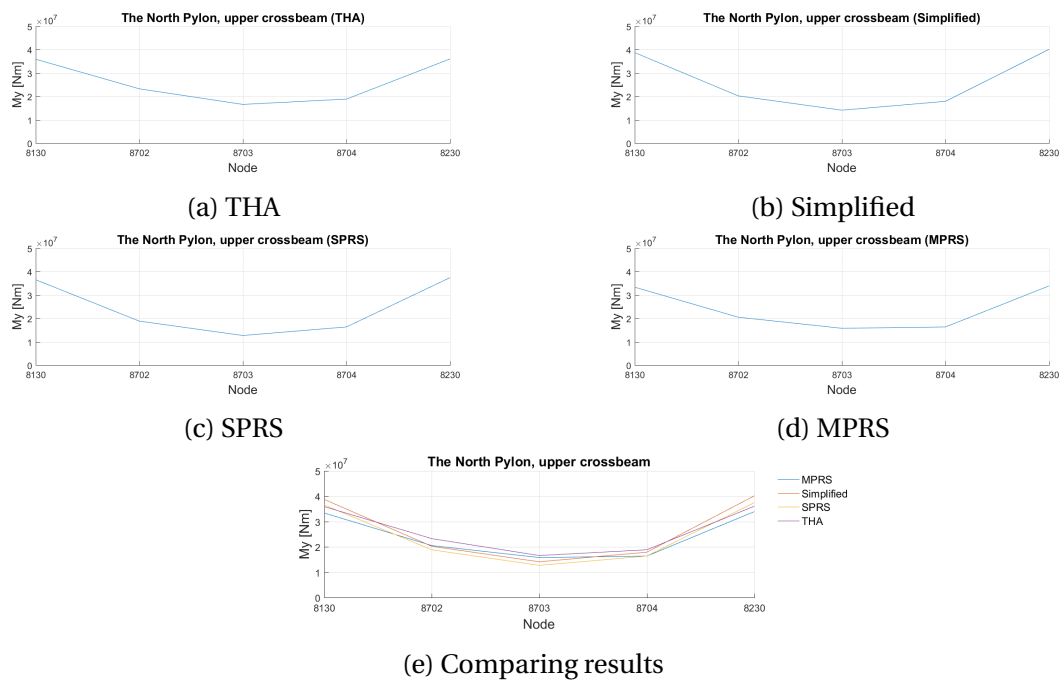
Figure A.16: Moment about global vertical axis (My)

The Central Pylon, pile tops

(a) THA

(b) Simplified

(c) SPRS

(d) MPRS

(e) Comparing results
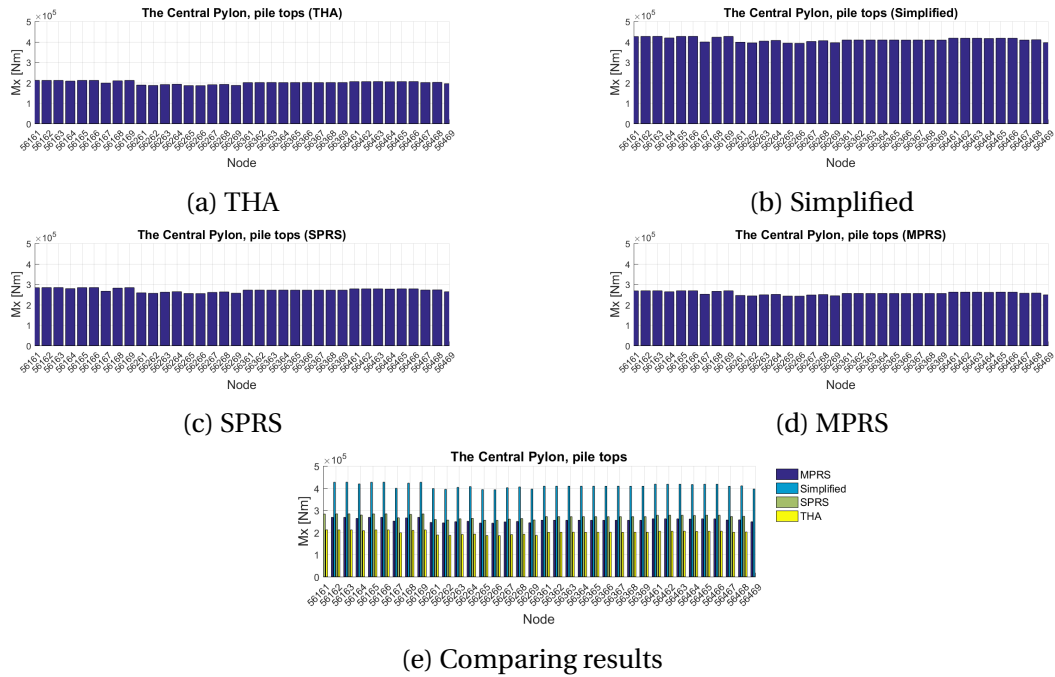
Figure A.17: Moment about global vertical axis (Mx)

(a) THA

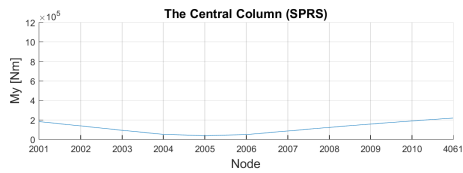(b) Simplified

(c) SPRS

(d) MPRS

(e) Comparing results
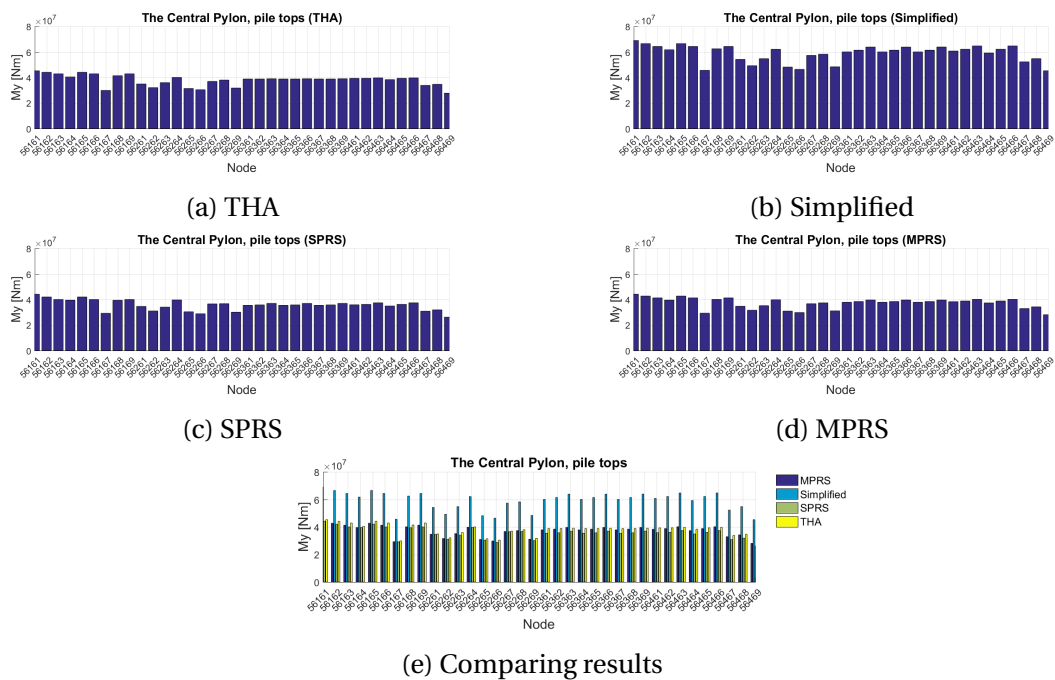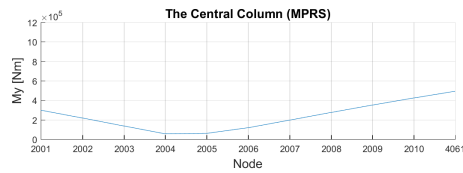
Figure A.18: Moment about global longitudinal axis (My)

(a) THA

(b) Simplified

(c) SPRS

(d) MPRS

(e) Comparing results
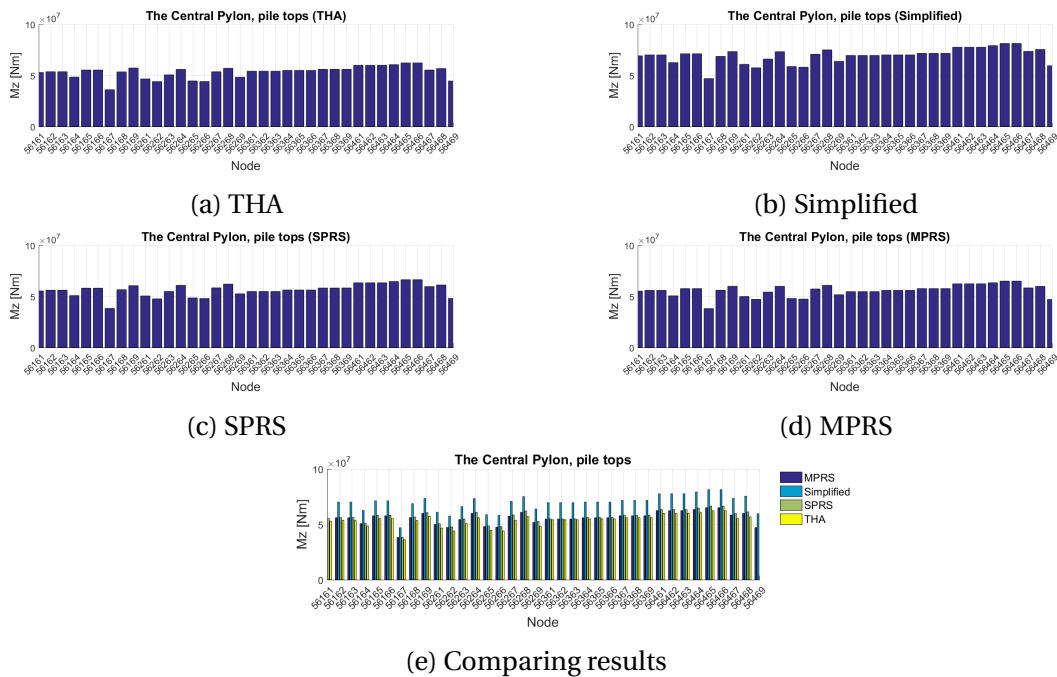
Figure A.19: Moment about global transverse axis (Mz)

The North Pylon, pile tops

(a) THA

(b) Simplified

(c) SPRS

(d) MPRS

(e) Comparing results
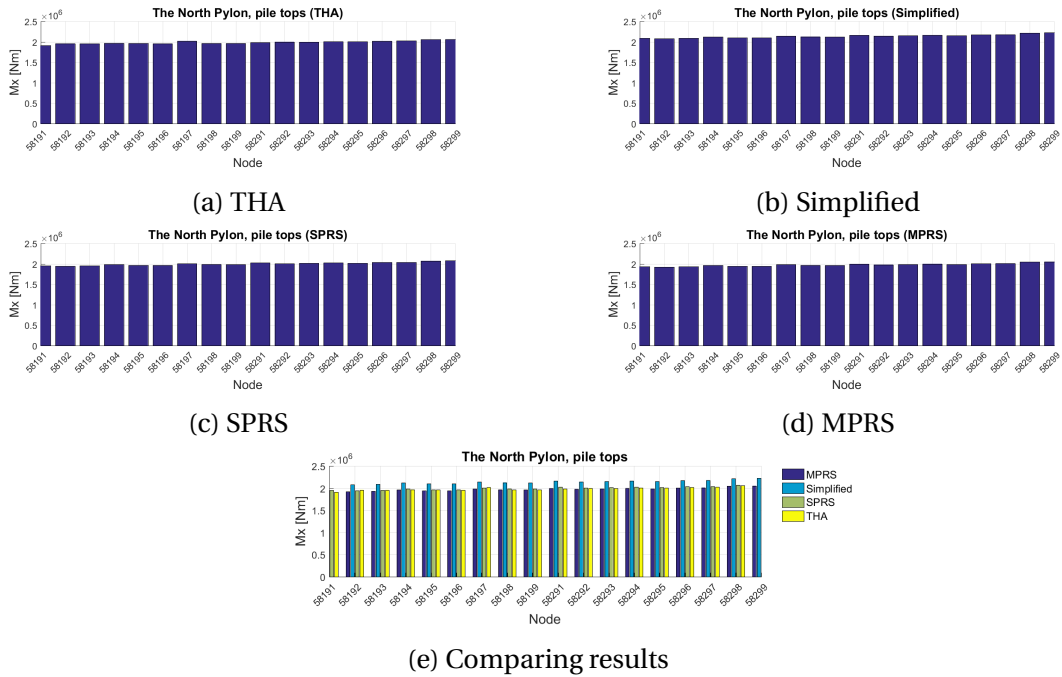
Figure A.20: Moment about global vertical axis (Mx)

(a) THA

(b) Simplified

(c) SPRS

(d) MPRS

(e) Comparing results
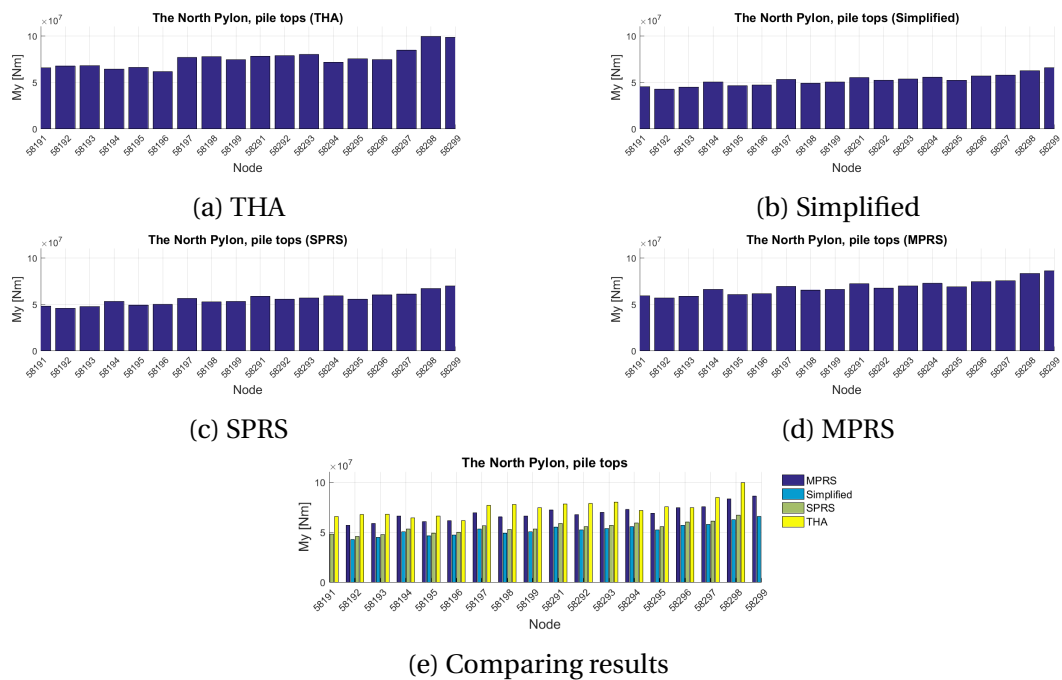
Figure A.21: Moment about global longitudinal axis (My)

(a) THA

(b) Simplified

(c) SPRS

(d) MPRS

(e) Comparing results
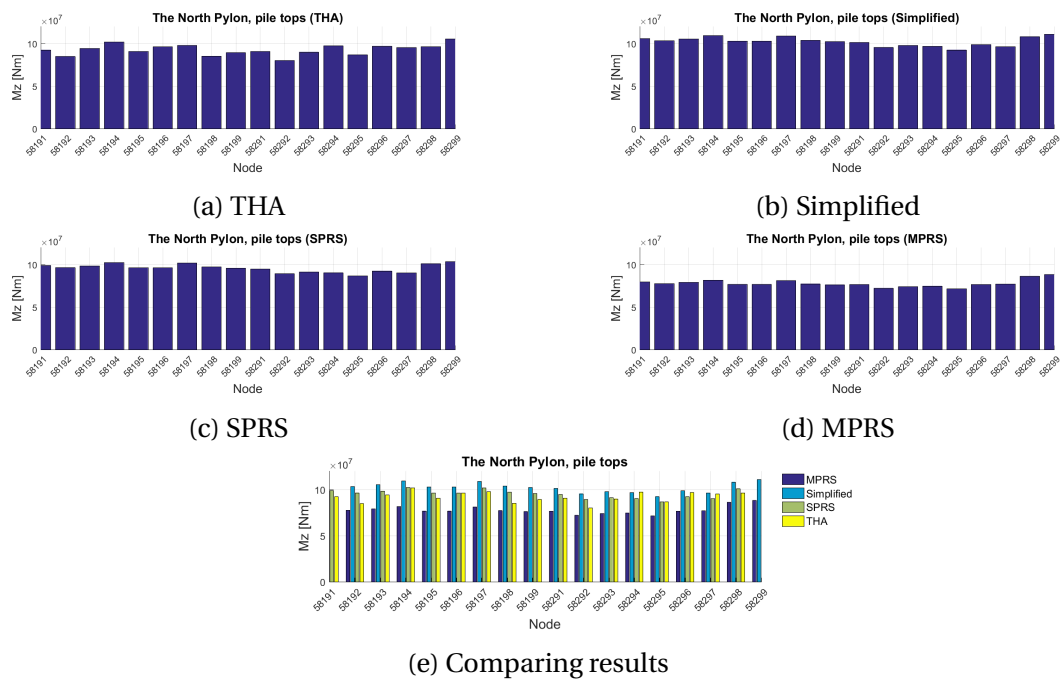
Figure A.22: Moment about global transverse axis (Mz)

Girder

(a) THA

(b) Simplified

(c) SPRS

(d) MPRS

(e) Comparing results
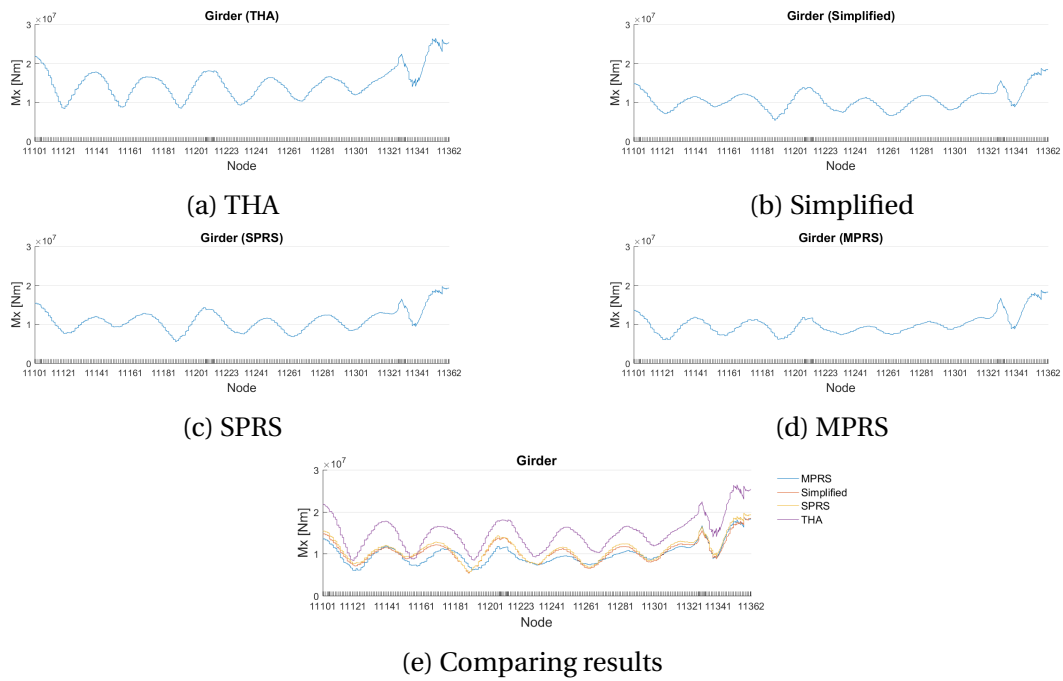
Figure A.23: Moment about global longitudinal axis (Mx)

(a) THA

(b) Simplified

(c) SPRS

(d) MPRS

(e) Comparing results
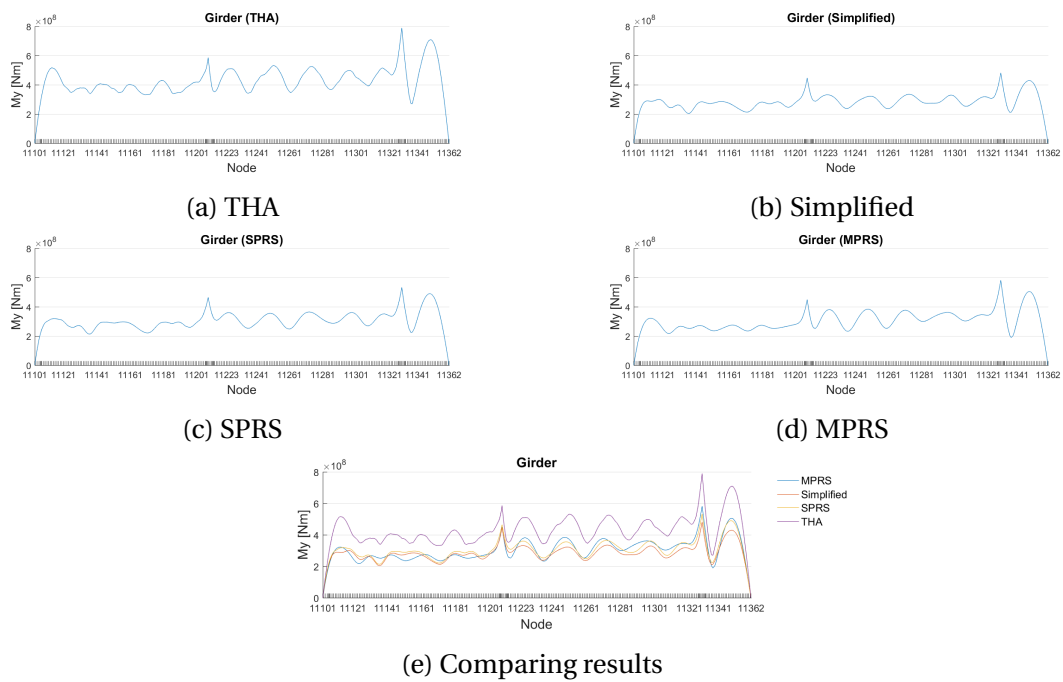
Figure A.24: Moment about global vertical axis (My)

(a) THA

(b) Simplified

(c) SPRS

(d) MPRS

(e) Comparing results
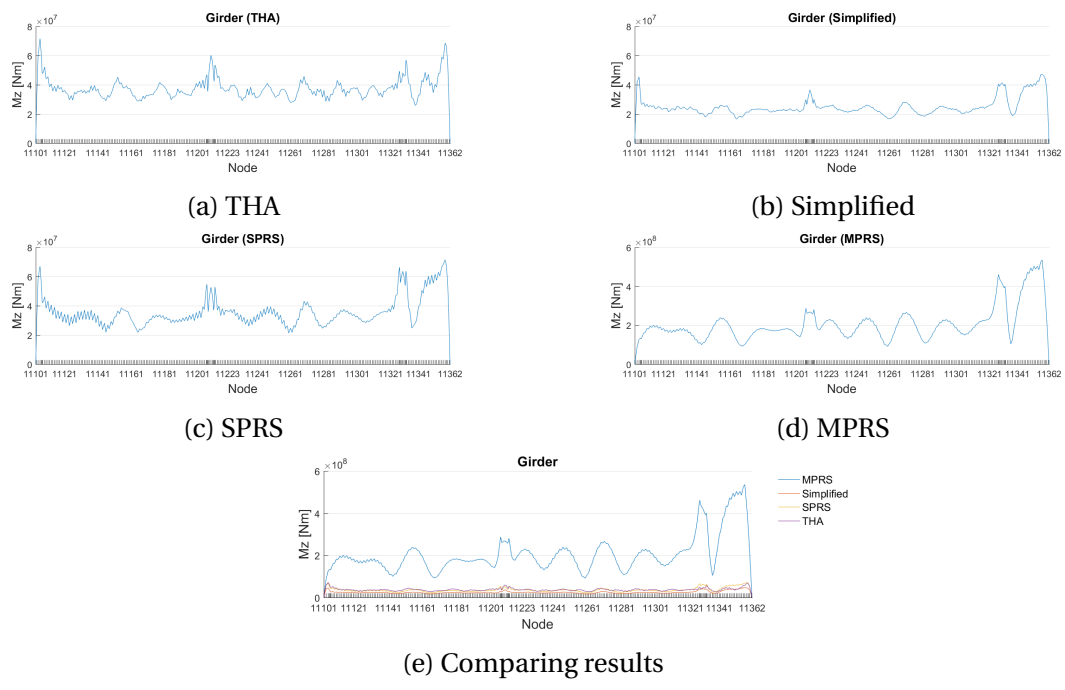
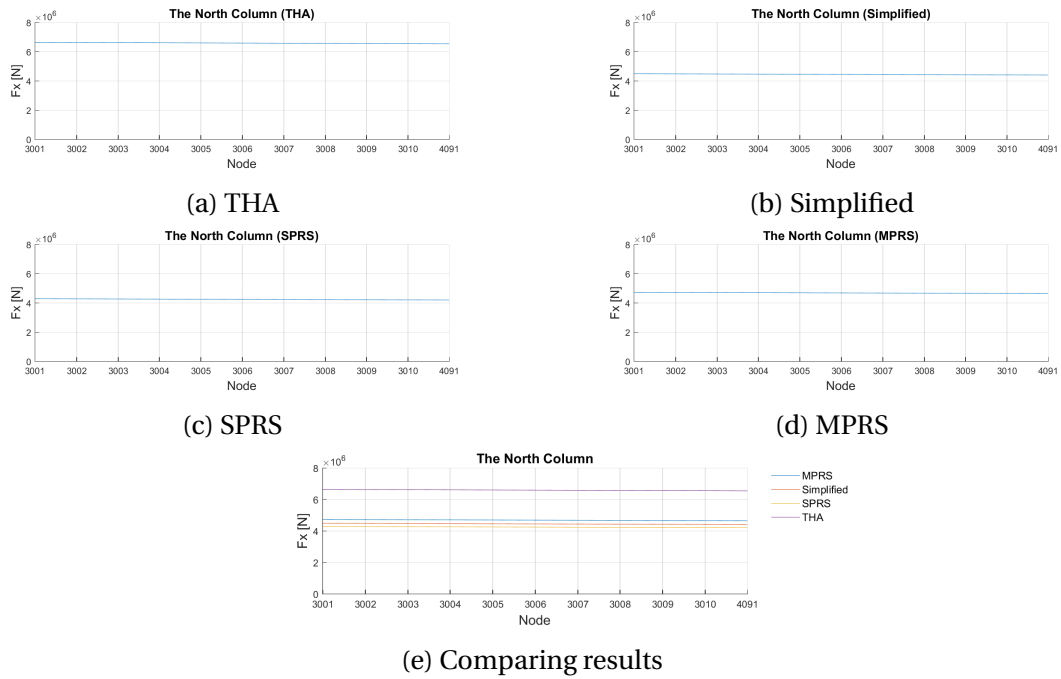Figure A.25: Moment about global transverse axis (Mz)

Appendix B

Results from the Simple Bridge

The South Column

(a) THA

(b) Simplified

(c) SPRS

(d) MPRS

(e) Comparing results
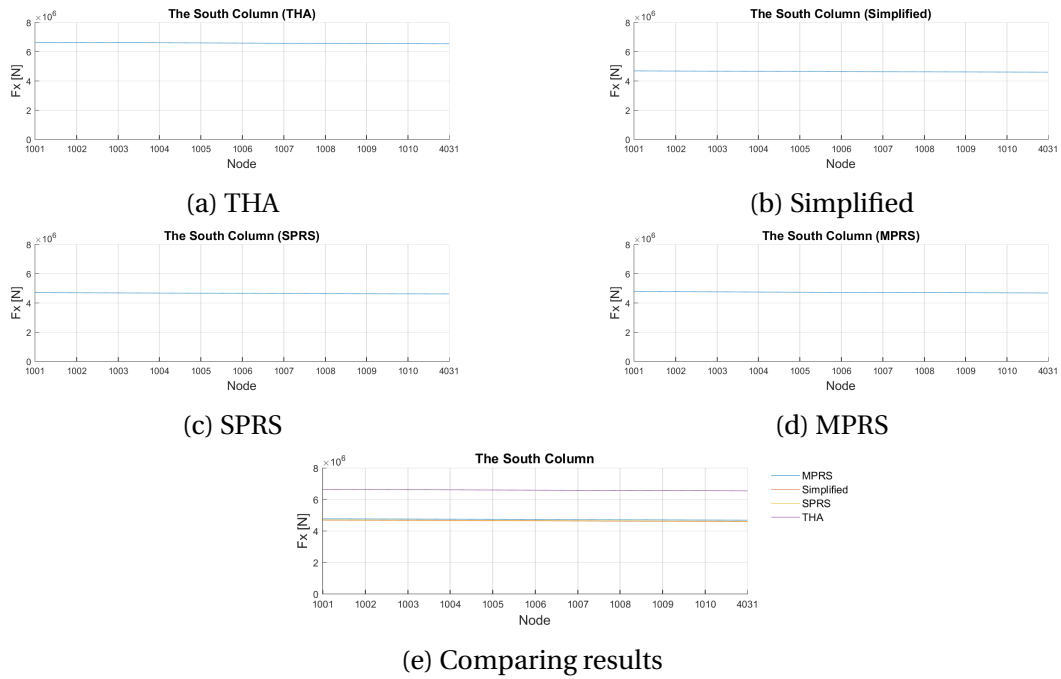
Figure B.1: Force along global vertical axis (Fx)

(a) THA

(b) Simplified

(c) SPRS

(d) MPRS

(e) Comparing results
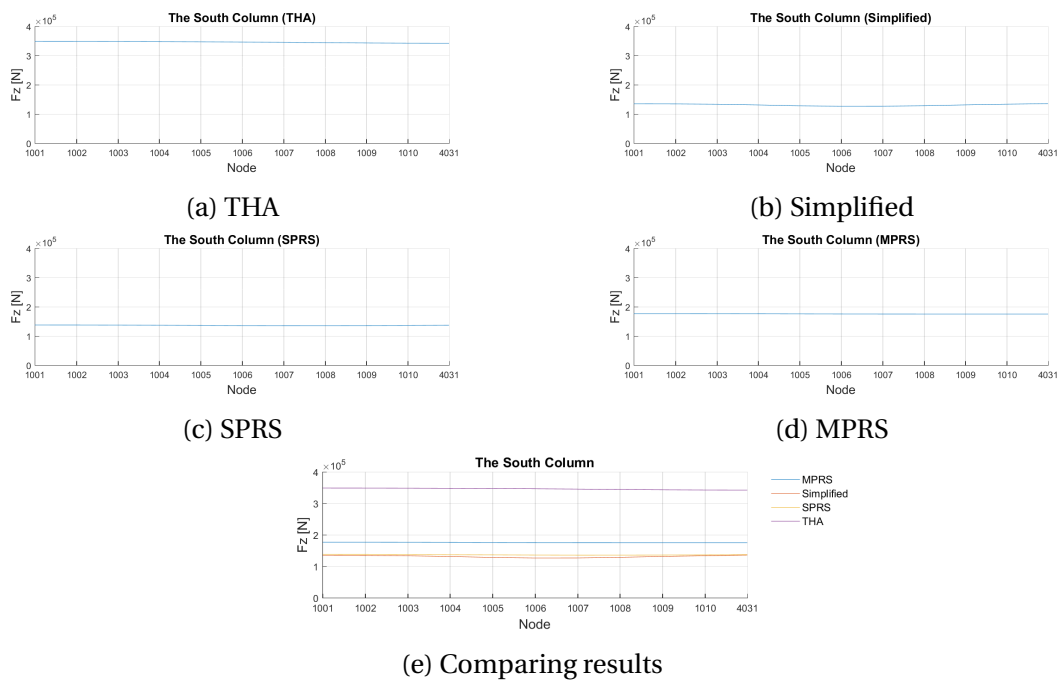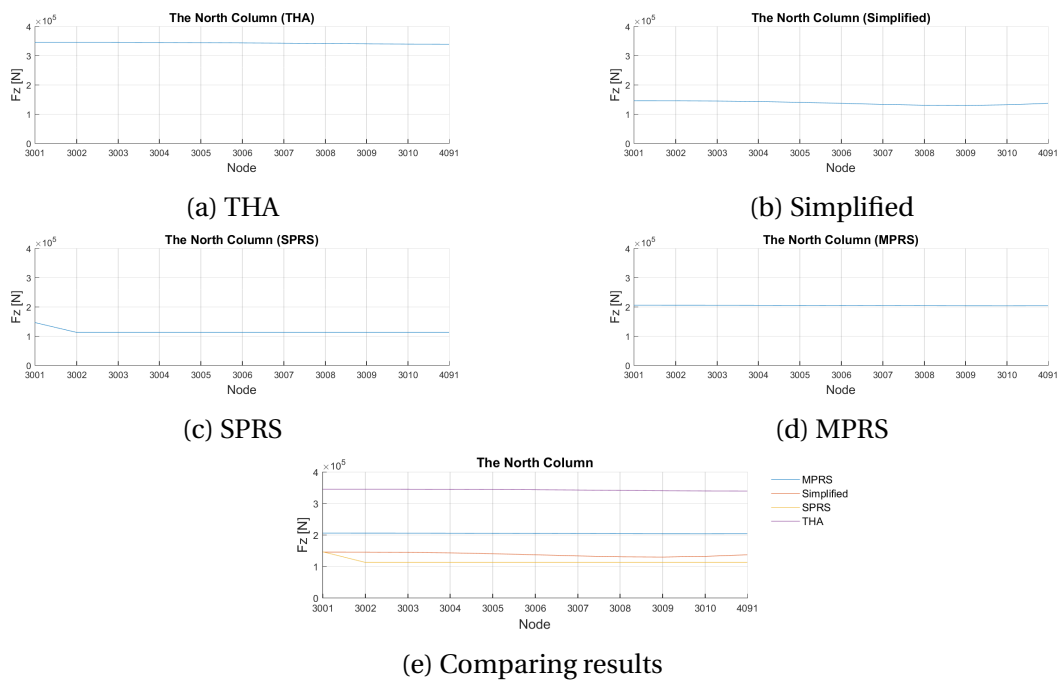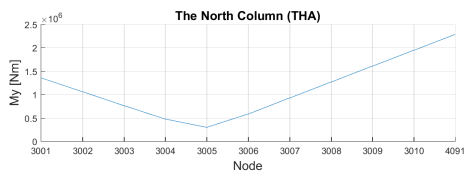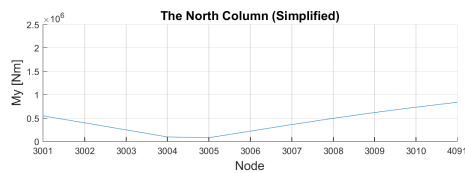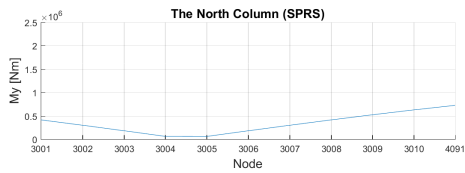
Figure B.2: Force along global longitudinal axis (Fz)

(a) THA

(b) Simplified

(c) SPRS

(d) MPRS

(e) Comparing results
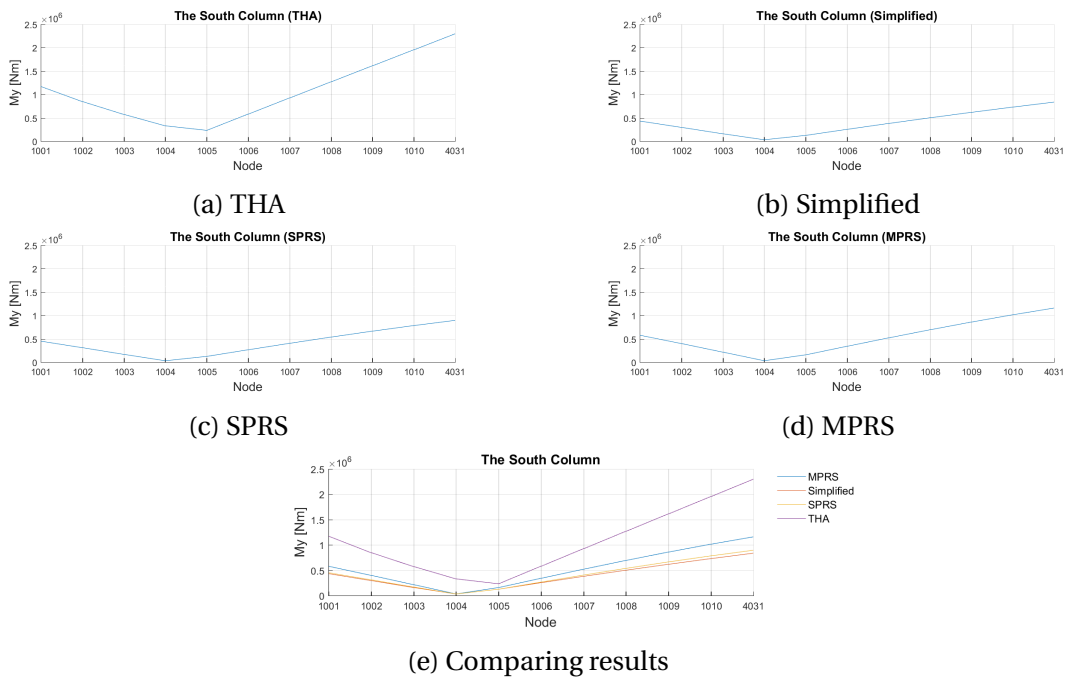
Figure B.3: Moment about global transverse axis (My)

The Center Column

(a) THA

(b) Simplified

(c) SPRS

(d) MPRS

(e) Comparing results
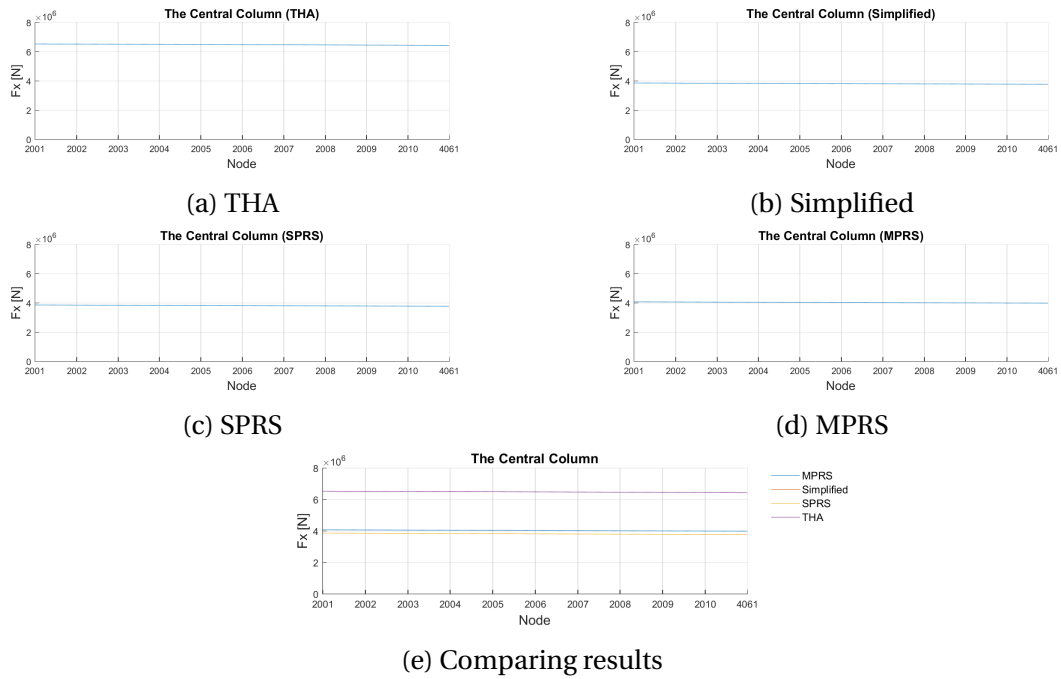
Figure B.4: Force along global vertical axis (Fx)

(a) THA

(b) Simplified

(c) SPRS

(d) MPRS

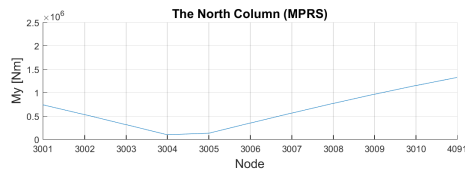(e) Comparing results
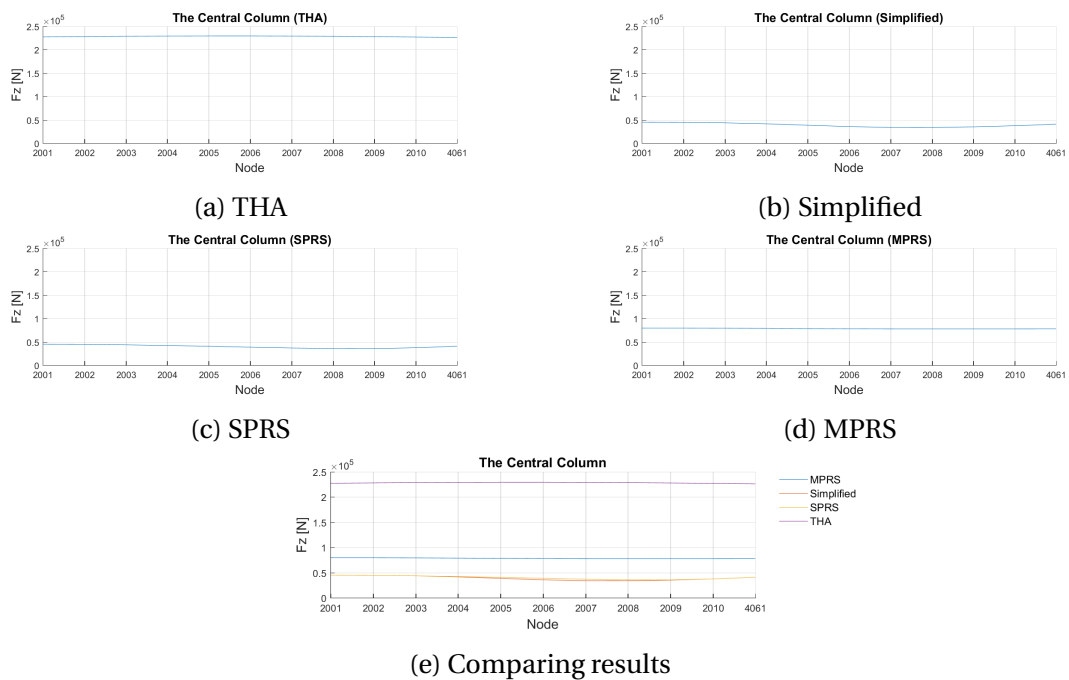
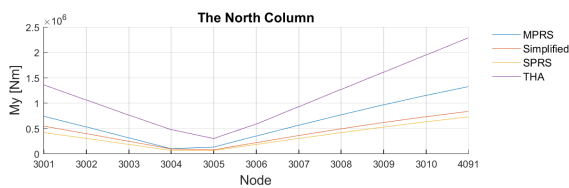Figure B.5: Force along global longitudinal axis (Fz)
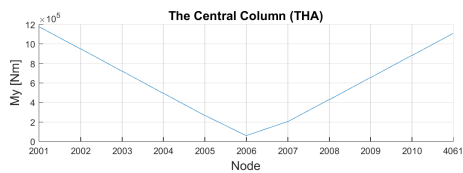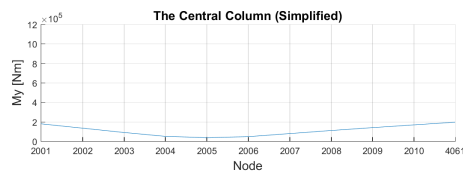
(a) THA

(b) Simplified
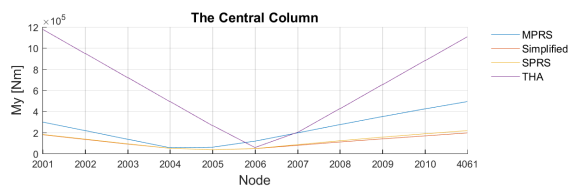
(c) SPRS

(d) MPRS

(e) Comparing results

Figure B.6: Moment about global transverse axis (My)

The North Column

(a) THA

(b) Simplified

(c) SPRS

(d) MPRS

(e) Comparing results

Figure B.7: Force along global vertical axis (Fx)

(a) THA

(b) Simplified

(c) SPRS

(d) MPRS

(e) Comparing results

Figure B.8: Force along global longitudinal axis (Fz)

(a) THA

(b) Simplified

(c) SPRS

(d) MPRS

(e) Comparing results

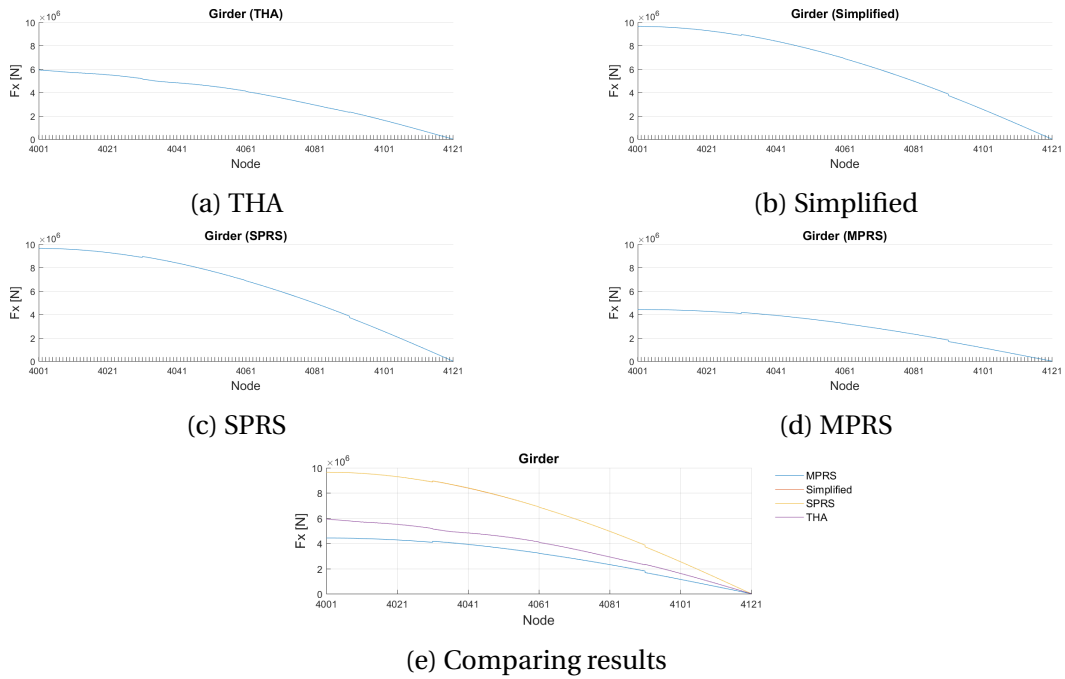Figure B.9: Moment about global transverse axis (My)

Girder

(a) THA

(b) Simplified

(c) SPRS

(d) MPRS

(e) Comparing results

Figure B.10: Force along global longitudinal axis (Fx)

(a) THA

(b) Simplified

(c) SPRS

(d) MPRS

(e) Comparing results
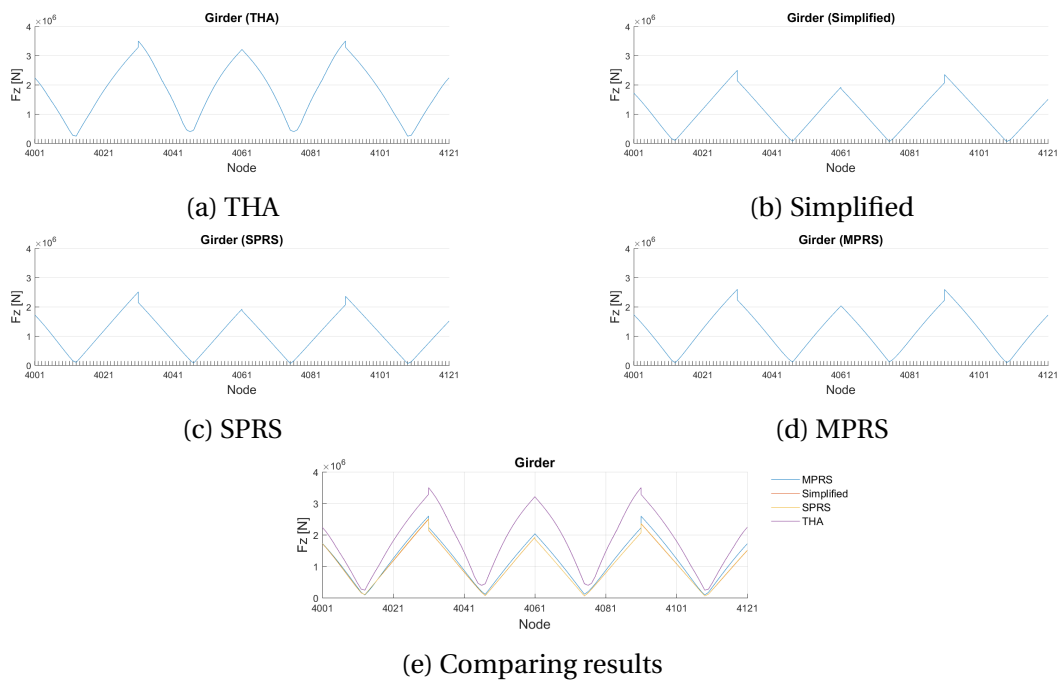
Figure B.11: Force along global vertical axis (Fz)

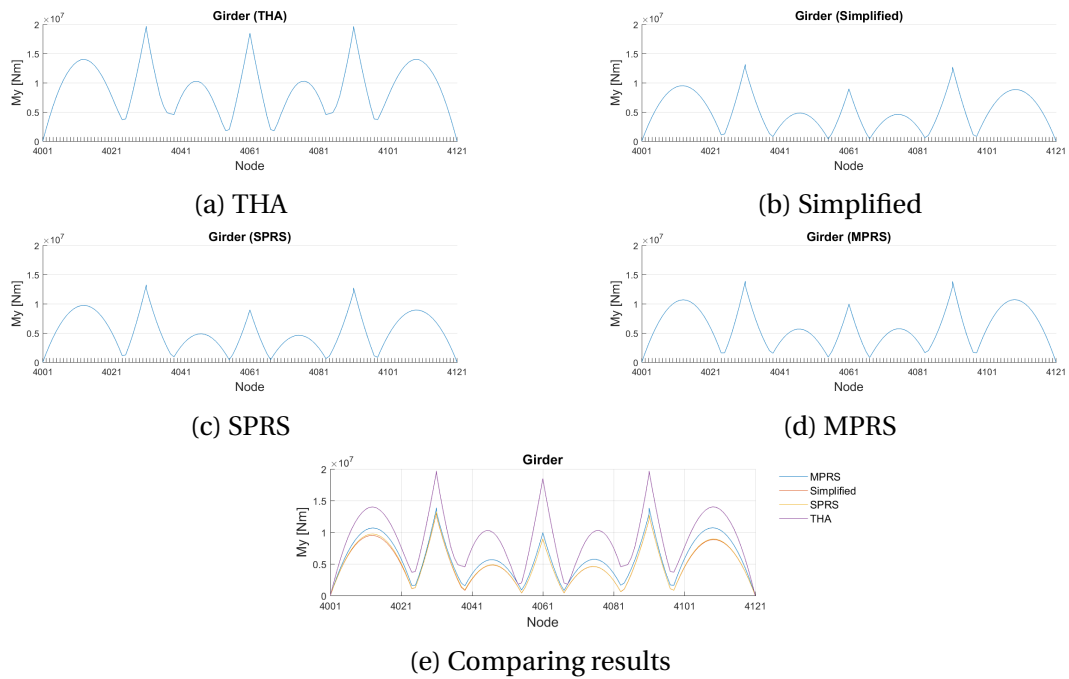(a) THA

(b) Simplified

(c) SPRS

(d) MPRS

(e) Comparing results

Figure B.12: Moment about global transverse axis (My)